Modelling and Verification of the Dynamics of an Ocean Current Energy Converter

by

Simon Graaff

Thesis presented in partial fulfilment of the requirements for the degree of Master of Science in Engineering (Mechanical) in the Faculty of Engineering at Stellenbosch University

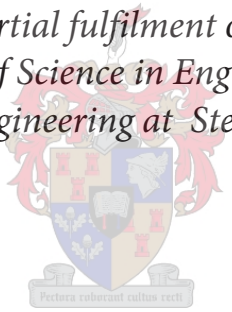

Supervisors: Prof J.L. Van Niekerk

Prof J.W. Von Backström

December 2014

Declaration

By submitting this thesis electronically, I declare that the entirety of the work contained therein is my own, original work, that I am the sole author thereof (save to the extent explicitly otherwise stated), that reproduction and publication thereof by Stellenbosch University will not infringe any third party rights and that I have not previously in its entirety or in part submitted it for obtaining any qualification.

Date: 2014/09/01 .....

Abstract

Modelling and Verification of the Dynamics of an Ocean Current Energy Converter

S. Graaff

Thesis: MScEng (Mech)

December 2014

South Africa has a significant potential resource for electrical power generation in the Agulhas Current on the southeast coast. The Ocean Current Energy Convertor studied in this project was designed to generate power from this current. The feasibility of this device was investigated by analysing the dynamic stability and controllability of the convertor, when acted upon by hydrodynamic forces while harvesting energy from the current. A simulation model was developed to predict the dynamic behaviour using the Simulink software suite. A scale model of the prototype was built and tested in the Towing Tank at Stellenbosch University, and the experimental results were compared against the simulation results. A control algorithm was designed, using the mathematical model, to control the roll angle and deployment depth. The control algorithm was tested in simulation.

The results indicated that the simulation model accurately predicted the behaviour of the prototype in testing, and results showed that the device is both stable and controllable. It was concluded that this OCEC design concept warrants further investigation. The recommendations are that the experimental model be improved to ensure reliable experimental results, that further complexity be added to the simulation model, and that the control algorithm be tested on the improved prototype in the towing tank.

Uittreksel

Modellering en Verifikasie van die Dinamika van 'n Seestroom Energie Omsetter

("Modelling and Verification of the Dynamics of an Ocean Current Energy Converter")

S. Graaff

Tesis: MScIng (Meg)

Desember 2014

Die Agulhas-seestroom aan die suidooskus van Suid-Afrika bied 'n aansienlike potensiële hulpbron vir elektriese kragopwekking. Die seestroomenergie-omsetter (SEO) wat in hierdie projek bestudeer is was ontwikkel om krag uit hierdie seestroom te genereer. Die doenlikheid van hierdie toestel is ondersoek deur die dinamiese stabiliteit en beheerbaarheid van die omsetter onder die invloed van hidrodinamiese kragte te analiseer terwyl dit energie van die stroom inwin. 'n Simulasiemodel is met behulp van Simulink-sagteware ontwikkel om die dinamiese gedrag te voorspel. 'n Skaalmodel van die prototipe was gebou en in die sleeptenk by Universiteit Stellenbosch getoets en die eksperimentele resultate met die simulasie se resultate vergelyk. 'n Beheer-algoritme is daarna ontwerp, deur middel van die wiskundige model, om die rolhoek en diepte van ontplooiing te beheer.Hierdie algoritme is tydens simulasie getoets.

Die resultate het aangedui dat die simulasiemodel akkuraat die gedrag van die prototipe tydens toetse voorspel het, en die resultate het gewys dat die toestel beide stabiel en beheerbaar is. Die gevolgtrekking is gemaak dat die SEO se ontwerpkonsep verdere studie regverdig. Die aanbevelings is dat die eksperimentele model verbeter word om betroubare eksperimentele resultate te verseker, dat verdere kompleksiteit by die simulasiemodel gevoeg word, en dat die beheer-algoritme op die verbeterde model in die sleeptenk getoets word.

Dedication

For my wife Shawn

Thank you for all the support, love, editing and, above all, patience.
I couldn't have done it without you.

Acknowledgements

My supervisors for their support and guidance through this project, and for the great opportunity to do this study:

- Prof Van Niekerk
- Prof Von Backström

The technical team in the Mechanical Workshop for their help and input during the prototype building and testing:

- Juliun Stanfliet
- Cobus Zietsman

Fellow students who gave their time and knowledge:

- Josh Reinecke
- James Joubert
- Neil Fourie
- Graham Newton
- Tim Verschaeva
- Charl Pierre Verster

My parents for mentorship and editorial assistance:

- Dr Anna Strebel
- Dr Johann Graaff

Contents

List of Figures

List of Tables

Nomenclature

α_0, β_0 Added mass constants
α Angle of attack of hydrofoil
α' Modified angle of attack of hydrofoil
γ Kinematic viscosity coefficient
δ Angle of the wing flap deflection
δ_A, δ_C Angles of control flaps
$\eta_1 = x, y, z$ Position in inertial reference
$\eta_2 = \phi, \theta, \psi^T$ Euler angles in inertial reference
η Relative angle between water flow and cable
Θ_T, x_T, z_T States at Trim
$\nu_1 = u, v, w$ Linear velocity of CG
$\nu_2 = p, q, r$ Angular velocity of CG
${\nu_1}^{rel}$ Relative linear water speed
${\nu_2}^{rel}$ Relative rotational water speed
$\rho =$ 1023 kgm^{-3} Density of sea water
$\tau_1 = X, Y, Z$ Total external forces in body-fixed reference
τ_{1B} Bouyancy force in body-fixed reference
τ_{1C}^i Total force in inertial reference of the ith cable section
τ_{1Cd}^i Drag force in inertial reference of the ith cable section
τ_{1Cp}^i Damping force in inertial reference of the ith cable section
τ_{1Cr}^i Restoring force in inertial reference of the ith cable section
τ_{1Cs}^i Stretch force in inertial reference of the ith cable section
τ_{1G} Gravity force in body-fixed reference
τ_{1H} Hydrofoil force in body-fixed reference
τ_{1P} Damping force in body-fixed reference
τ_{1R} Thrust force produced on the turbine in body-fixed reference
$\tau_2 = K, M, N$ External moments about CG
τ_{2B} Moment about CG due to the bouyancy force in body-fixed reference
τ_{2C} Moment induced by the cable about CG in body-fixed reference
τ_{2H} Moment of hydrofoil about CG in body-fixed reference

$\tau_{2_H^p}$ Pitching moment of hydrofoil about CG in body-fixed reference
τ_{2P} Moment about CG due to the damping force in body-fixed reference
τ_{2R} Torque produced on the turbine
ω_R Angular velocity of the rotor blades
A_B^n Projected cross-sectional area of a body element
A_B^t Projected tangential area of a body element
A_R^n Swept area of the turbine
A_H^n Effective area of the hydrofoil
A_R^t Projected tangential area of the turbine
A_C^n Cross-sectional area of the cable
A_C^t Projected tangential area of cable element
A_H^t Projected tangential area of the hydrofoil
A_T, B_T Matrix of coefficients at Trim
A, B, C State space matrices
A_w Effective area of the hydrofoil
a, b, c Ellipsoid semi-axes
C_D Hydrofoil drag coefficient
C_L Hydrofoil lift coefficient
C_M Hydrofoil pitch moment coefficient
C_N Hydrofoil normal force coefficient
C_{Pb}^n Body normal damping coefficient
C_{Pb}^t Body tangential damping coefficient
C_{Pc}^n Cable normal damping coefficient
C_{Pc}^t Cable tangential damping coefficient
C_{Ph}^n Hydrofoil normal damping coefficient
C_{Ph}^t Hydrofoil tangential damping coefficient
C_R^t Turbine tangential drag coefficient
C_T Turbine thrust coefficient
C_W Turbine power coefficient
C_X Hydrofoil chordwise force coefficient
CG Centre of gravity
D Characteristic length
DCM Direct Cosine Matrix
DE Department of Energy
DOF Degrees of Freedom
E Young's Elastic Modulus of the cable
EMEC European Marine Energy Centre

e Ellipsoid eccentricity

f_n, f_r Hydrodynamic loading coefficients

FAU Florida Atlantic University

G Control feedback coefficients

HAT Horizontal Axis Turbine

I_{xx}, I_{yy}, I_{zz} Moments of Inertia

I_{xa}, I_{ya}, I_{za} Moments of Inertia including added mass effect

l Original length of the cable

$J_1(\eta_2)$ Direct Cosine Matrix

l_s Stretched length of the cable

M_A Added mass matrix

m Mass of vessel

m^i Mass of the ith cable element

NERSA National Energy Regulator of South Africa

NREL National Renewable Energy Laboratory

OCEC Ocean Current Energy Converter

OH Oscillating Hydrofoil

q Constant of effect of flap on angle of attack

R_{0B} Vector from the CG to the centre of bouyancy

R_{0P} Vector from the CG to the geometric centre of each body component

R_{0X} Vector from the CG to the point in question

R_{0H} Vector from the CG to the geometric centre of the wing

R_{0C} Vector from the CG to the cable tether point

R_x, R_y, R_z Rotations about x, y, and z axes

R_n Reynolds number

r Radius of the rotor blades

$Sv =$ 10^6 $\mathrm{m^3 s^{-1}}$ Volume flow rate

SA South Africa

SMD Soil Machine Dynamics

SRET Sea Renewable Energy Turbine

u Unit vector in the direction of the cable section

$\mathbf{u}$ States of the input variables

$\frac{\partial \dot{u}}{\partial u}$ Partial derivatives for each state

V Volume

V_w Speed of the current

V^i Volume of the ith cable element

$v =$ 1.56 x $10^{-6}\mathrm{m^2 s^{-1}}$ Kinematic viscosity of sea water

VAT Vertical Axis Turbine

$X_{\dot{u}}, Y_{\dot{v}}, Z_{\dot{v}}, K_{\dot{p}}, M_{\dot{q}}, N_{\dot{r}}$ Added mass coefficients

X_i, Y_i, Z_i^T Directions in inertial reference

X_b, Y_b, Z_b Directions in body-fixed reference

$\mathbf{x}$ States of the vessel

Chapter 1

Introduction

Since 2006, South Africa has experienced major problems with its electricity supply, with the country having to deal with scheduled blackouts or "load-shedding" that affected both private consumers and industry. This is due to greater than expected economic growth in the country, resulting in bigger demand on the power supply, as well as poor planning of power plant construction. Almost no new power plants have been built in the last 20 years. After it was seen what a major impact the load-shedding had on the economy there is now a rush to increase South Africa's power capacity to meet future demands.

Another significant driver of the future of South Africa's power supply is the goal of reducing carbon emissions. The state utility, Eskom, has a power generation mix that is over 85% dependent on coal. This means that South Africa's electricity is among the most carbon intensive in the world. In 2003 the Department of Minerals and Energy set a target of 10,000 GWh of renewable energy contribution to final energy consumption by 2013. It was decided that the best way to achieve this goal was to incentivise the private sector to contribute to power production. To achieve this a Renewable Energy Independent Power Producer Procurement Programme (REIPPP) was implemented by the Department of Energy in 2011 which offers premium rates to private energy producers who set up renewable energy facilities and establish a Power Purchase Agreement with Eskom. After a number of iterations of reviewing the process, three rounds of bids have thus far been allocated under this program with more due to follow.

While the bulk of renewable energy production up until now comes from solar and wind, the country has other natural resources that could be utilised for power production. Having 2,800 km of coastline, the ocean is a resource that is, as yet, untapped. South Africa has two major ocean currents that flow along its coasts: the Benguela on the west coast, and the Agulhas on the east coast. The Agulhas Current in particular has significant potential for energy production as it is one of the strongest currents in the world by speed and volume. It also within 25 km of the coast which would reduce the cost of transmission.

The C-Plane concept for generation of electrical energy from ocean currents has existed since the 1940's, though it has never been implemented full-scale. The concept is that a hydrofoil is placed into the current, tethered by a cable to the ocean bed. This hydrofoil has two turbines on the downstream side which are turned by the current and generate electricity. The hydrofoil uses control surfaces to maintain the optimum depth and orientation in the water. The hydrofoil also brings the device to the surface when maintenance is required or dives deeper if the device needs to avoid extreme conditions at the surface of the ocean, such as a major storm.

A version of this concept has been proposed by the Sea Renewable Energy Turbine company. This device is known as the Ocean Current Energy Convertor (OCEC), which is shown in the concept drawing Figure 1.1. The OCEC

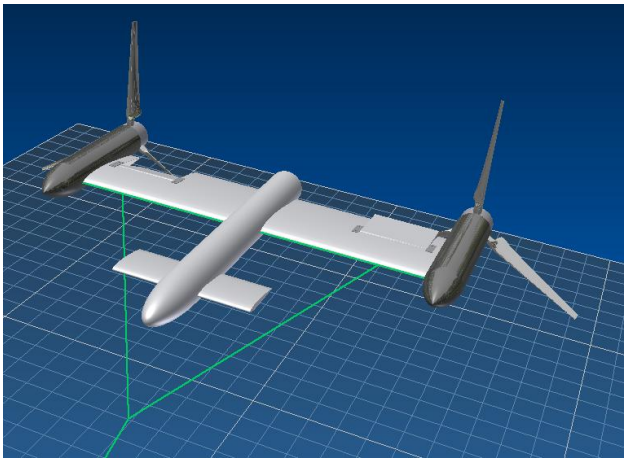

Figure 1.1: Concept drawing of OCEC

has all the characteristics of the C-Plane concept, including two counter-rotating turbines, a hydrofoil surface, and a tether to the seabed. There are also two sets of control surfaces: the canards on the fuselage to control the pitch angle, and the ailerons on the wings to control the roll angle.

The objective of this study is to investigate the feasibility of the OCEC concept by determining whether the design is dynamically stable and controllable when acted upon by hydrodynamic forces. First, a simulation model will be created in Matlab, based on mathematical theory, to predict the behaviour of the device. Then a scale prototype will be built of the design, tests will be run in the towing tank and data will be gathered. This data will be compared against the simulation prediction to verify the model. Finally, a control strategy will be designed for the depth and pitch angle, and this strategy will be simulated using the model to predict its behaviour. Based on these findings, a conclusion will be made on whether the design is stable and controllable, and would therefore warrant further study.

Chapter 2

Literature Review

2.1 Agulhas Current and its Potential for Energy Generation

Ocean currents are directed, continuous flows of sea water in the world's oceans. These currents are the result of a number of factors including prevailing wind, rotation of the Earth, and salinity or temperature differences in the water. The major ocean currents of the world are shown in Figure 2.1. Note that in the Southern Hemisphere currents flow anticlockwise, while in the Northern Hemisphere currents flow clockwise.

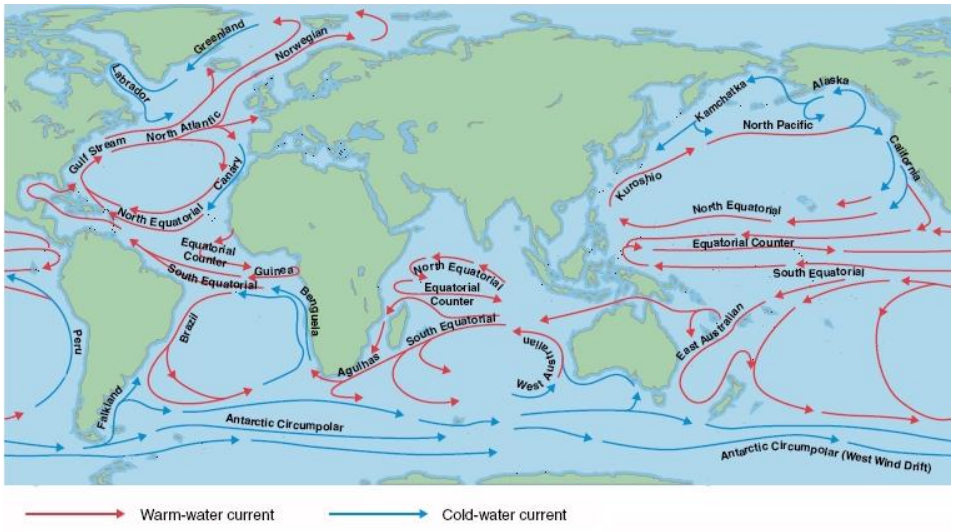

Figure 2.1: Major ocean currents of the world [1]

The Agulhas Current is the Western Boundary Current of the Indian Ocean that runs poleward down the east coast of Africa. It has its origin in the South Equatorial Current of the Indian Ocean that runs westwards along the 15° S latitude line, going around north and south sides of Madagascar and

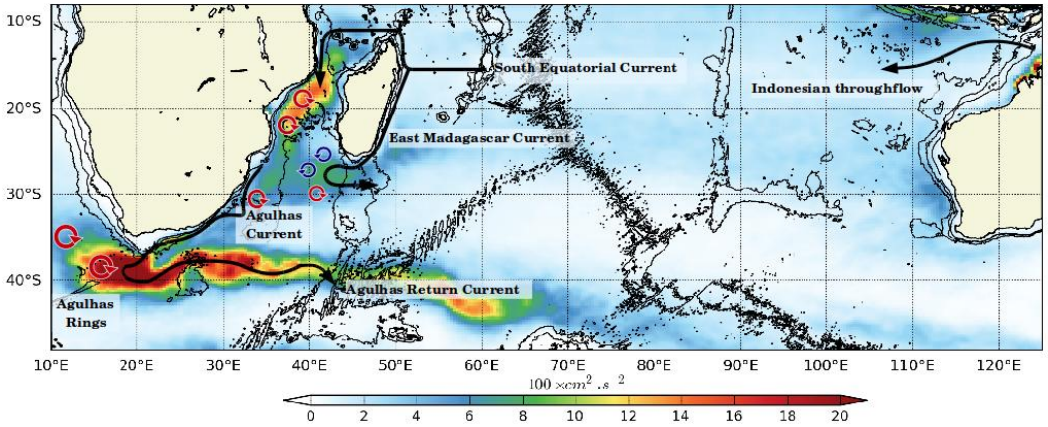

Figure 2.2: Schematic of the circulation in the South Indian Ocean. Colour contours give mean Eddy Kinetic Energy, while the arrows show the main current flows[2]

then down the east coast of South Africa before "retroflecting" or changing direction back eastwards towards the Indian Ocean at 40° S latitude, as shown in Figure 2.2.

Looking in more detail at the Agulhas current along the South African coastline, it can be seen from Figure 2.3 that the current closely hugs the coast particularly from Durban to Port Elizabeth, before following the contour of the Agulhas Bank further away from the coast. It then turns sharply back eastwards.

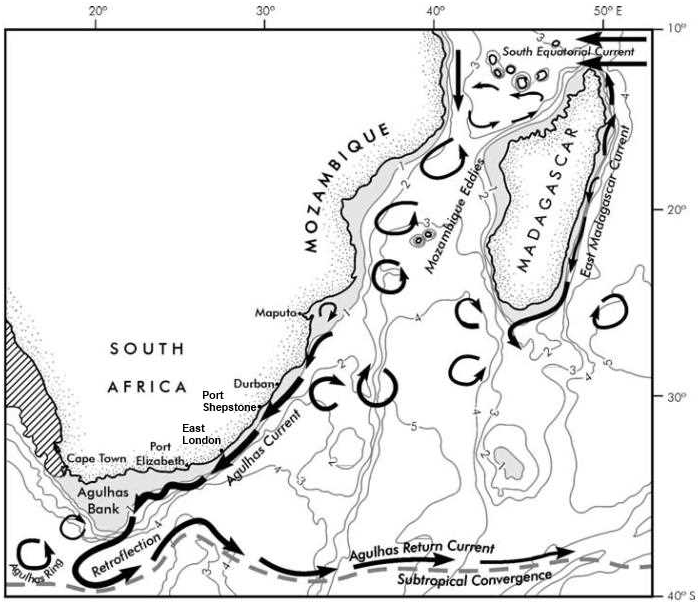

Figure 2.3: Detail of Agulhas Current [3]

The area of strongest flow is the area from Port Shepstone to East London

where the currrent hugs the coast. Figure 2.4 shows the velocity profile of the current at four points along the coast. This shows that the current stays between 20-60 km off the coast in this region, with flows up to 2 ms^{-1}. The average transport has been calculated as 69.7 Sv ($10^6 m^3/s$) which makes the Agulhas Current the largest Western Boundary Current in the world ocean [17]. The core of the current, where the flow is the greatest, is close to the surface, about 100 m below sea level.

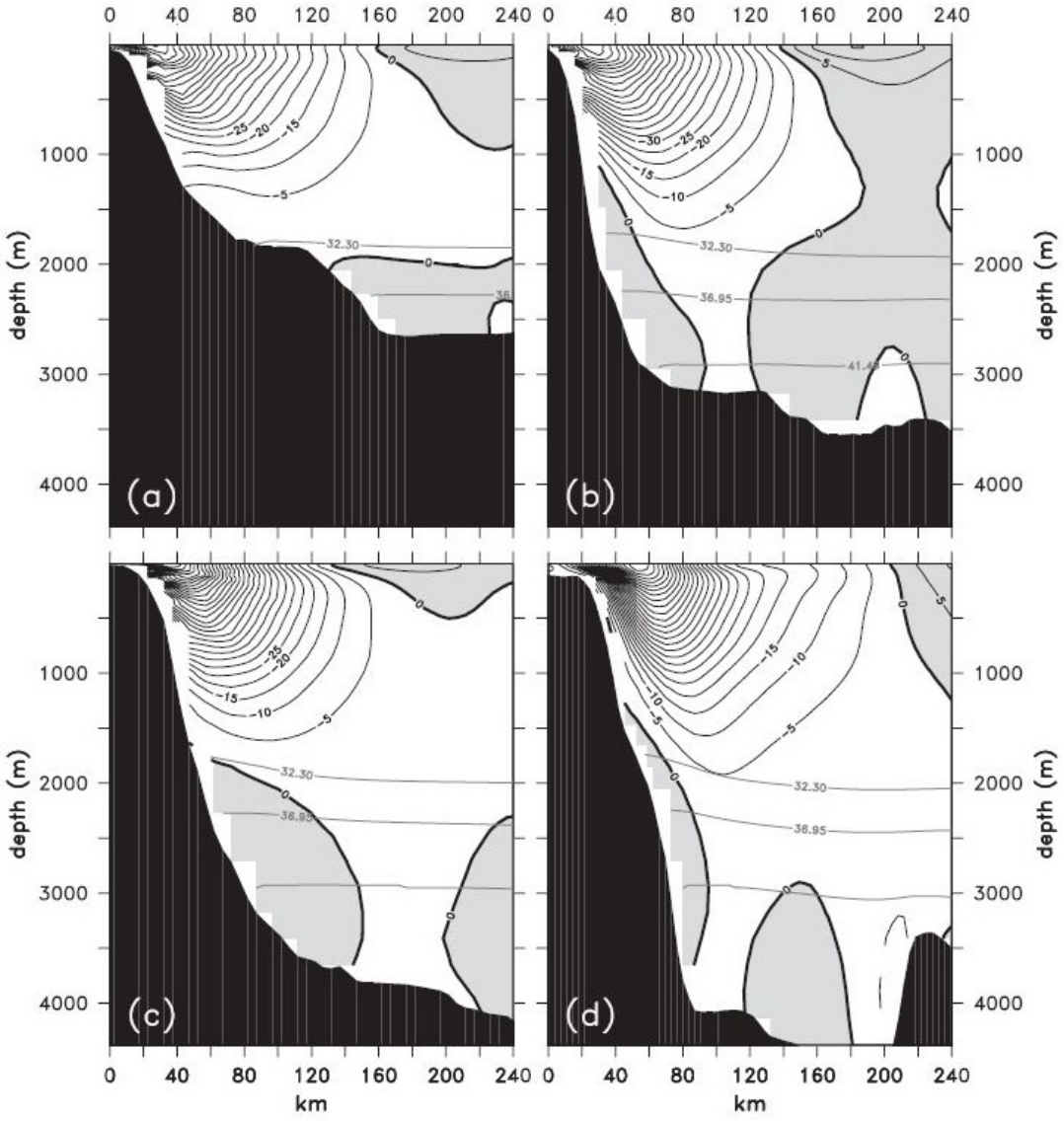

Figure 2.4: Agulhas Current velocity cross section at (a) Richards Bay, (b) Port Shepstone, (c) East London, and (d) Port Elizabeth. Contours show speed in cms^{-1}. Negative indicates flow in southerly direction [4]

The current does have a degreee of variability in its speed over a 12-month period, with velocitites up to 3 ms^{-1} recorded. A typical exceedance

of probability plot of velocity is shown in Figure 2.5.

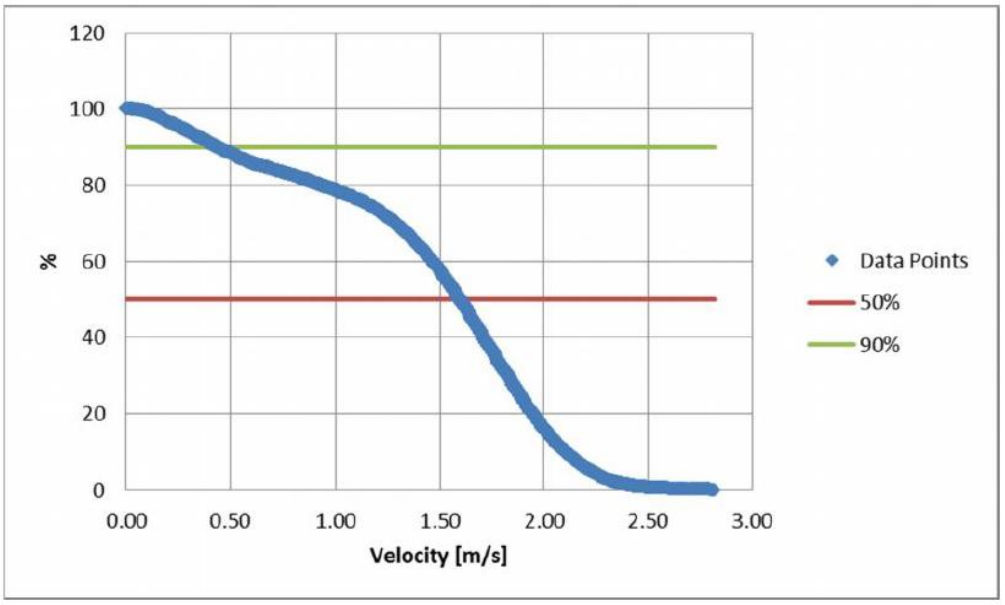

Figure 2.5: Exceedance of probability plot for Cape Morgan [5]

This current has a number of interesting features, one of which can also be also be seen in Figure 2.4. There is an undercurrent below the Agulhas Current at a depth of about 2,000 m that flows in the opposite direction to the main flow, back towards the Equator.

Another significant feature is a seasonal variation, that happens about six times a year, called the Natal Pulse. Figure 2.6 shows the velocity vector representation of a pulse moving down the South African coast. It is, in essence, a big vortex that is generated from eddies in the Madagascar Channel, and moves at a rate of 20 km/day [18]. As can be seen in the velocity cross-section in Figure 2.6 this results in the core of the current being disrupted and moving up to 160 km further offshore for the few days that the pulse is passing.

A number of recent studies have examined the feasibility of producing energy from the Agulhas Current, with the potential untapped energy estimated to be anything from 21.4 - 27.1 GW [5], which makes the prospect very attractive for interested parties. Feasible locations have also been identified with good resources and close proximity to appropriate electrical grid infrastructure. The reports have concluded that, while there are significant challenges that stand in the way of effectively utilising the Agulhas Current as a resource, with the right technology these challenges could be overcome.

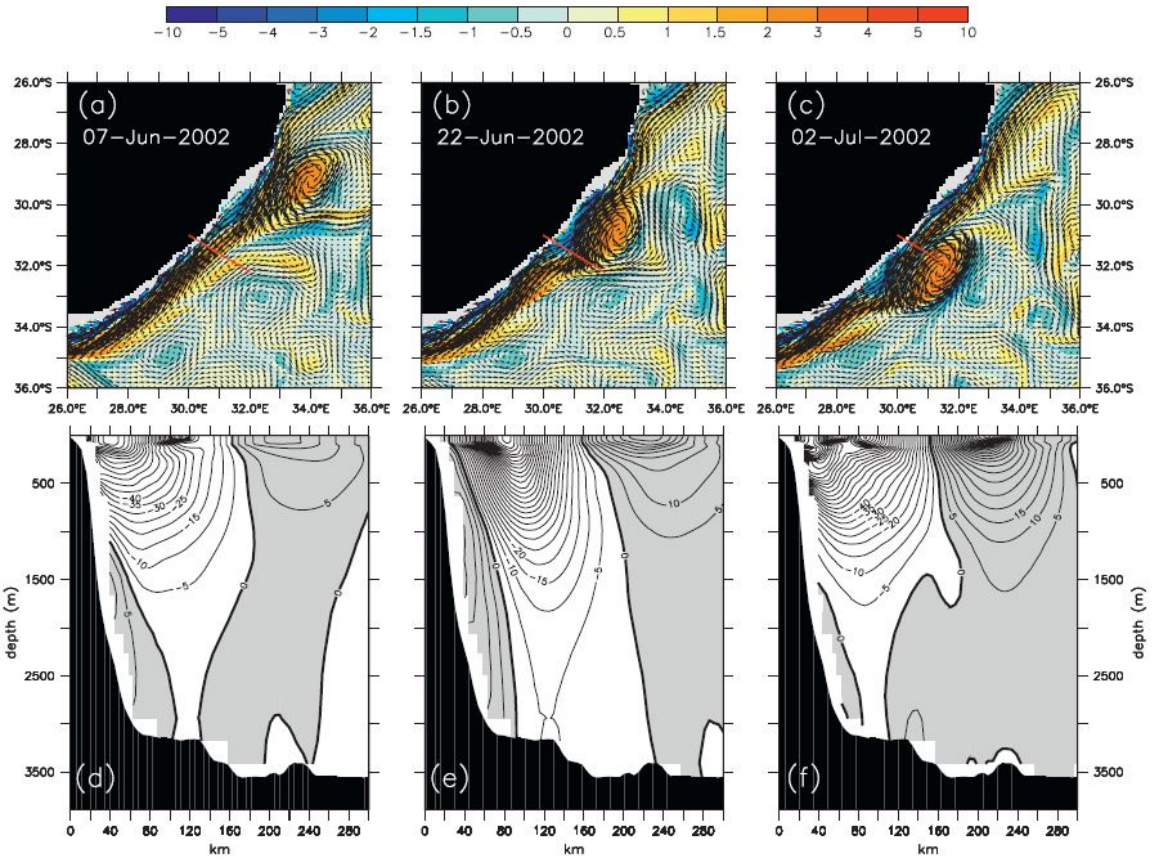

Figure 2.6: Natal Pulse vorticity and velocity cross section [4]

2.2 Electricity and Renewable Energy in South Africa

In 2006, damage to the Koeberg nuclear power station resulted in rolling blackouts in the Western Cape, and by 2007 the entire country was experiencing "load-shedding", as demand outstripped supply by nearly 2 GW [19]. This was the result of a combination of factors including poor capacity build planning, coal shortages, and maintenance problems. As a result there is currently an urgent drive to increase the country's generating capacity.

As previously mentioned, South Africa's electricity mix is predominantly derived from coal power. Only 5% of power can be considered to be in any way "renewable", mostly in the form of hydropower. Table 2.1 shows the large disparity in power sources for Eskom power.

South Africa hosted the World Summit on Sustainable Development in 2002, and renewable energy was brought back into the national consciousness. In 2003 the Department of Minerals and Energy set a target of 10,000 GWh of renewable energy consumption by 2013 [21]. In 2011, the Department of Energy published a Request for Proposal (RFP) for the procurement of renewable energy from Independent Power Producers (IPP's) in three rounds. By

Table 2.1: Eskom generating capacity by type 2012 [20]

Type	Number of stations	Number of units	Net maximum capacity
Coal-fired	13	79	34 772 MW
Coal-fired (return to service)		*8*	*949 MW*
Hydroelectric	2	6	600 MW
Pumped storage	2	6	1 400 MW
Nuclear	1	2	1 800 MW
Wind	1	3	3.2 MW
Open Cycle Gas Turbine (OCGT) (Liquid fuel)	4	20	2 409 MW
Total	23	124	41 933.2 MW

November 2013 the department had allocated renewables projects as follows:

- 2011 Round 1 - 1,416 MW
- 2012 Round 2 - 1,044 MW
- 2013 Round 3 - 1,465 MW [22]

Indications are that further allocations will be made in the future, though the quantities are yet to be determined. There is currently both the economic demand and the political will to drive the building of renewable energy facilities. This makes it a favourable environment for the development of new renewable energy sources, such as the Ocean Current Energy Converter device.

2.3 Ocean Current Converters

Mankind has been using flowing water to do work for thousands of years, with watermills being the oldest example. The flow of water, usually in a river or aqueduct, is used to turn a mill that grinds wheat into flour. Watermills were used by the ancient Romans and the Chinese from around the middle of the 3^{rd} century BC. Waterwheels have been described as "the earliest human application of a natural force to do work" [23]. Through the ages more and more uses were found for power from water such as sawing wood, bellows for metalwork, and culminating in the advent of massive hydropower plants where water is used to turn turbines to generate electricity.

Using the ocean for power is far less common than using rivers. The only historical example of using the ocean to do work is the tidal mill, which works on much the same principle as a watermill. The Persians used tidal mills as far back as 1050 AD [24]. However, use of ocean power has not been

able to progress much beyond this point, particularly due to the harsh conditions at sea which would destroy any device that was built using traditional technology.

The drive for renewable energy in the 1970's has lead to a resurgence of interest in ocean energy, with particular focus on wave power. Using ocean currents for power is less popular, but there is evidence of concepts being formulated from the late 1800's [25]. A review conducted by the author of the activity in the ocean current energy field produced over 70 separate devices being developed in 15 countries around the world. Current Converters can be broadly broken up into four categories:

- Horizontal Axis Turbines
- Vertical Axis Turbines
- Oscillating Hydrofoils
- Others

They are simplistically depicted in Figure 2.7. They will be described in more detail in the sections that follow. These devices can further be described by their mooring method:

- Seabed Mounted - has a base that is directly attached to the bed, secured by either its own weight or additional fixings.
- Pile Mounted - attached to a concrete or steel pile driven deep into the bed.
- Flexible Tether - attached by a cable that is free to move. Rigid Tether, where the device is attached by a rigid structure that may have a few degrees of motion.
- Floating Platform - attached to a structure that floats on the top of the water.

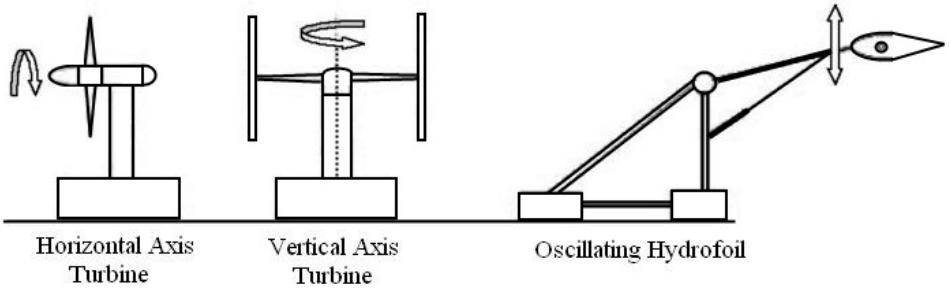

Figure 2.7: Current device categories [6]

2.3.1 Horizontal Axis Turbines (HAT's)

These are the most common ocean current devices, due to their similarity to wind turbines, and use of similar components. HAT's can be basically described as turbines that have their main axis of rotation parallel to the flow of water. HAT's can be further categorised as Open or Closed, depending on whether they have ducting around the blades and also by the number of blades. Two, Three, and Multiple blade configurations are the most common. By far the most well-known project is the 1.2 MW SeaGen device built by

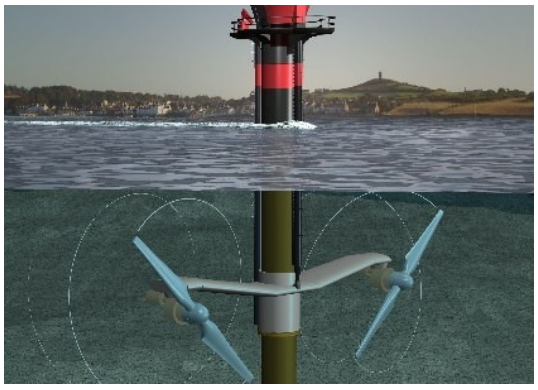

Figure 2.8: SeaGen [7]

Marine Current Turbines in Northern Ireland [7].

2.3.2 Vertical Axis Turbines (VAT's)

These devices have their axis of rotation perpendicular to the flow of water. There are three main types: H-Darrieus, Savonius, and Helical as shown in Figure 2.9.

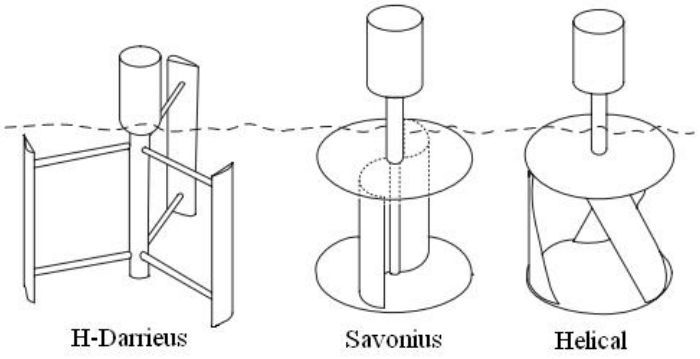

Figure 2.9: Types of Vertical Axis Turbine [8]

An example is the 250 kW EnCurrent device, developed by New Energy Corporation and scheduled to be installed in Canada [26].

Figure 2.10: EnCurrent

2.3.3 Oscillating Hydrofoils (OH's)

These devices use the lift force created by water flowing over a hydrofoil to create a vertical oscillating motion that produces power. An example is the 250 kW Stingray by Dutch company The Engineering Business of which a full-scale prototype has been built [27].

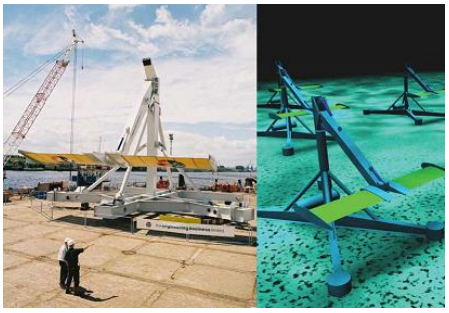

Figure 2.11: Stingray

2.3.4 Others

There are many other unique designs that don't fit into any of the above categories, but show the range of ingenuity being applied to the concept of ocean current devices. Examples are waterwheels, screws, and sails.

There is currently significant interest in the ocean current generator concept around the world, and many groups are investigating different ways of extracting energy from those currents. Research into the Ocean Current Generator Converter is, therefore, in line with global research trends.

2.4 C-Plane

The "C-Plane" design that is the subject of this study is by no means an original concept. Documents show that it has existed since the 1940's. The C-Plane is an electrical power generating device that uses the flow of water to turn turbines that produce electricity. The device consists of two counter-rotating turbines attached to each other by a thin body. Either the body or a surface on the body is shaped like a hydrofoil which produces dynamic buoyancy that allows the device to float in the water stream. Control surfaces, like those on an aeroplane wing, allow the device to adjust its depth automatically. The device is moored to the seabed by a cable (or number of cables) that allows the device to change its orientation depending on the flow of the current.

The first documented evidence of this concept is a 1946 patent by Ernst Souzcek in Austria that describes a "Stream Turbine" as shown in Figure 2.12.

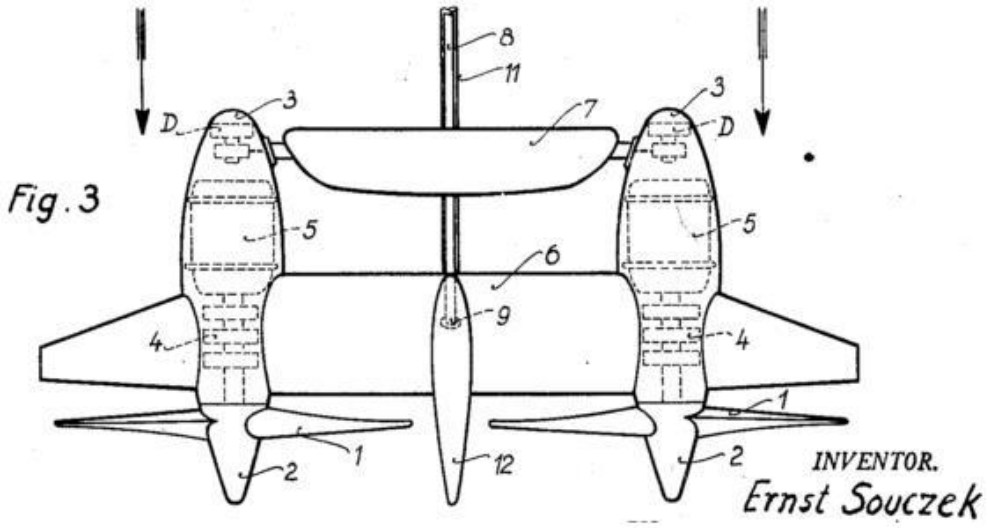

Figure 2.12: Stream Turbine [9]

He describes his device as an "underwater carrier connected with the turbine and creating dynamic buoyancy" with "control devices in a manner similar to airplane wings" and a pair of turbines "running in opposite direction" which "hangs on a rope anchored at the bottom of the water course" [9]. These are all the basic elements of the C-Plane as defined above. No evidence can be found from the literature of whether this device was ever built.

In 1979 Wallace Bowley patented an "Underwater Power Generator", which was conceptualised to take advantage of the well-known Gulf Stream Current off the east coast of the United States of America. It was designed as a more reliable alternative to wind or tidal power generators (Figure 2.13). It also contains all the chief C-Plane elements: two counter-rotating turbines, hy-

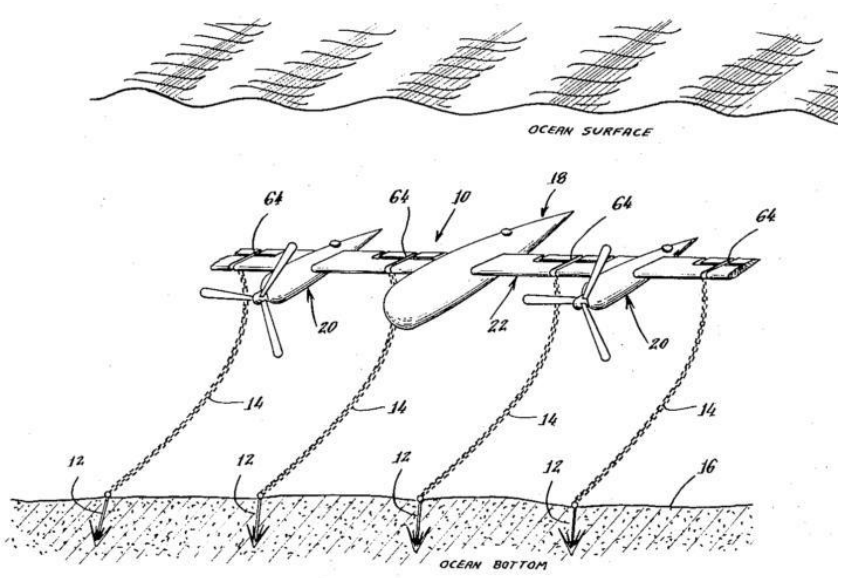

Figure 2.13: Underwater Power Generator [10]

drofoil surface to create bouyancy, moored by cable to the ocean bottom [10]. This device also appears to never have been constructed.

More recently, interest in this concept has been renewed, with a number of independent projects in progress. In 1998, James Dehlsen patented a control method for a "Tethered Water Current-Driven Turbine" shown in Figure 2.14 (c) [28]. He has subsequently developed his design further, setting up a company EcoMerit Technologies to commercialise the device under the name Aquantis, while receiving research assistance from Florida Atlantic University. Currently, studies are still being completed and funding sought [29].

In 2001, John Robson patented a "Submersible Electrical Power Generating Plant" as shown in Figure 2.15 that contains all the elements of the C-Plane. In 2006, he submitted a further patent with refinements to the design [30] [31]. He established the company Gulf Stream Turbines LLC that is trying to source funding to further develop the device, while currently continuing to refine the design [32].

In 2004, Ralph Manchester patented his "Submerged Power Generating Apparatus" [33] which has been subsequently developed for commercial use by the Soil Machine Dynamics (SMD) company under the name of TidEL (Figure 2.16). Currently a $\frac{1}{10}$ th scale model is undergoing testing at EMEC [34].

In 2010, Steven Oldfield formed a company called Sea Renewable Energy (Pty) Ltd with the aim of employing a C-Plane device, as shown in Figure 2.17, into the Agulhas Current off the coast of South Africa to produce power. This device is based upon the Aquantis device described above. He has employed Stellenbosch University to assist with the design and feasibility studies. This device is currently awaiting approval for funding from the South African government. The C-Plane concept is an established idea that is

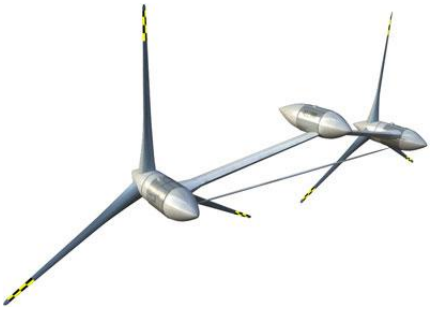

(a) Latest concept

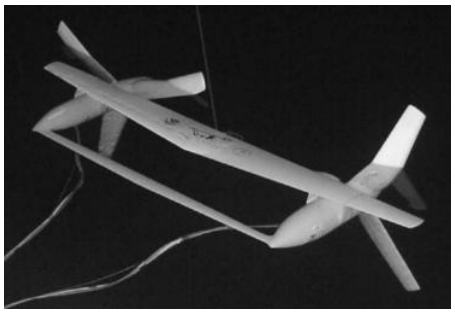

(b) FAU test unit

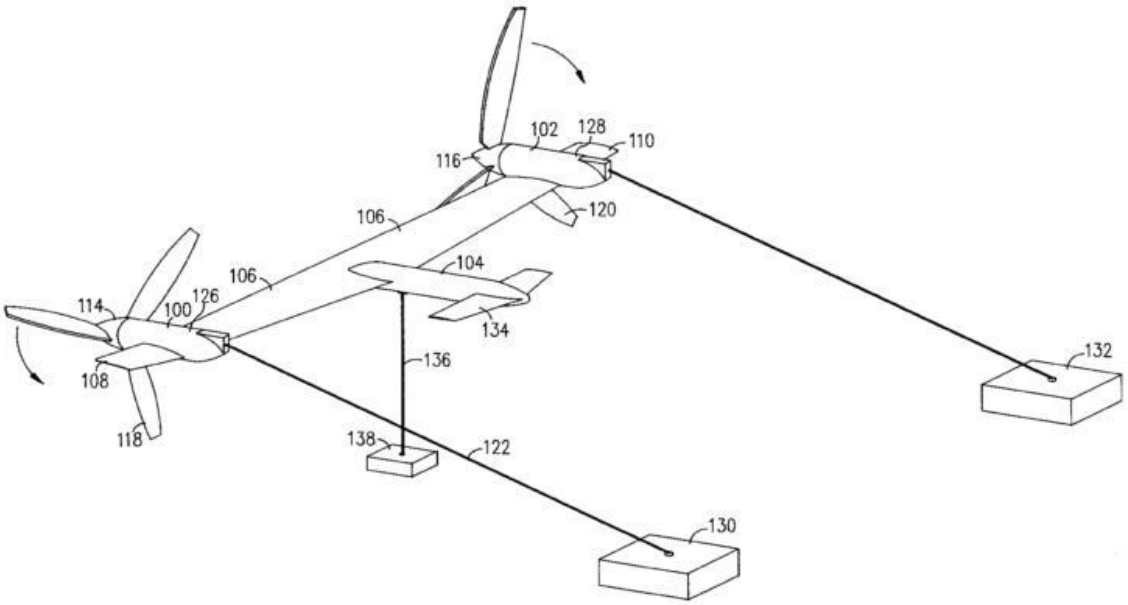

(c) Original patent

Figure 2.14: Incarnations of the Aquantis device

receiving renewed interest given the ongoing concerns regarding global warming. In the search for the most practical method of generating power from ocean currents the C-Plane is clearly a favoured concept that deserves further study.

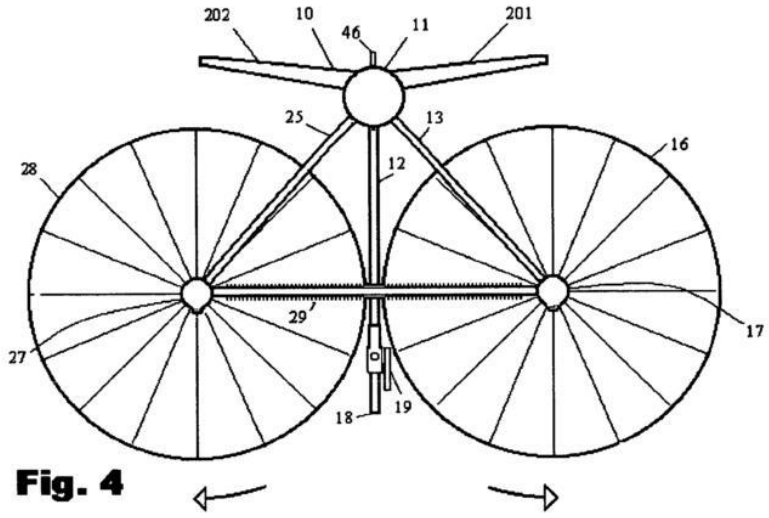

Figure 2.15: Submersible Electrical Power Generating Plant [30]

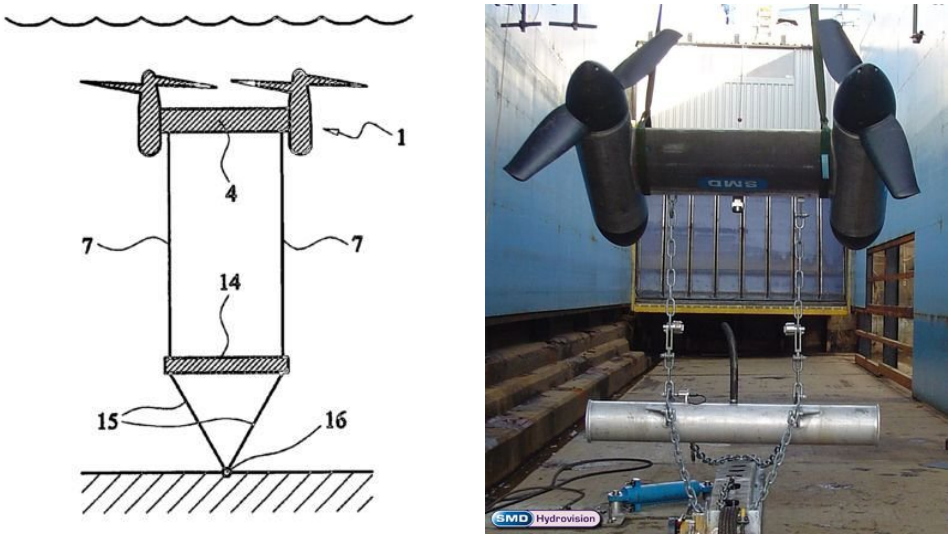

(a) Original patent (b) Towing tank test unit

Figure 2.16: TidEL device from SMD Hydrovision [34]

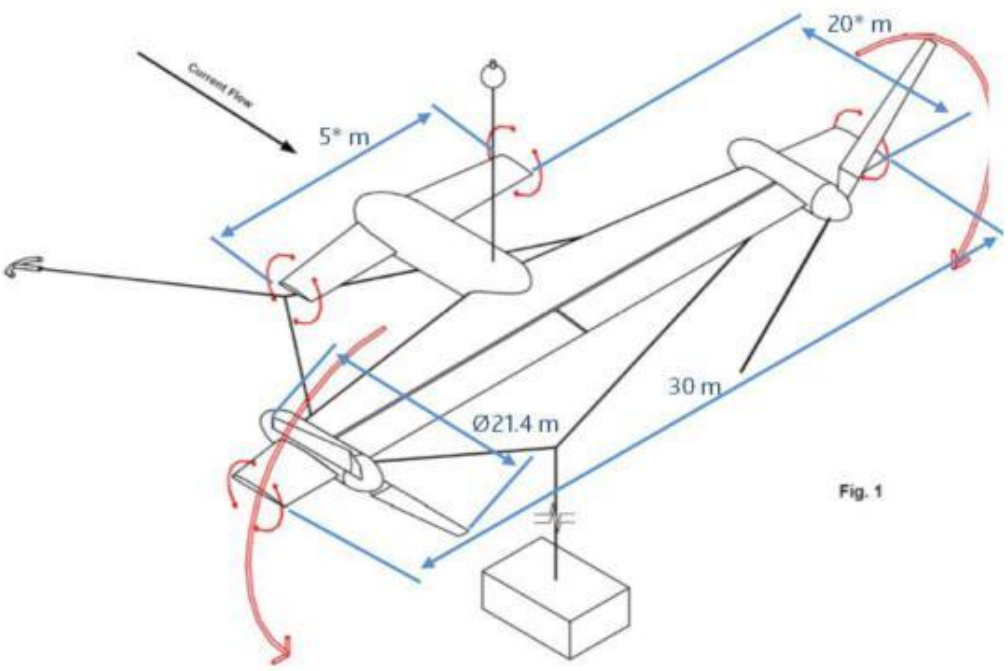

Figure 2.17: Sea Renewable Energy Technologies device [16]

Chapter 3

Mathematical Modelling

3.1 Notation and Coordinates

3.1.1 State Description

For the purposes of precision, terminology will now be defined for describing the positions relative to the OCEC and the state of the OCEC itself. For convenience of notation, the standard naval terminology will be used for the identification of locations relative to the vessel. Figure 3.1 shows a graphical representation.

"Fore" denotes the front of the vessel. "Aft" denotes the rear of the vessel. "Starboard" denotes the right side of the vessel, while "Port" denotes the left

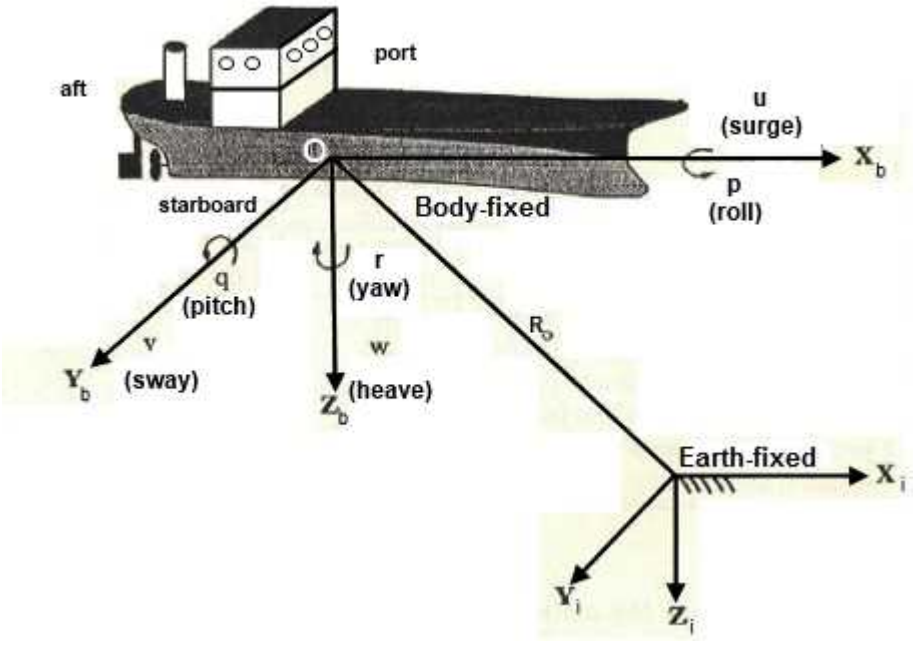

Figure 3.1: Body-fixed and earth-fixed reference frames [11]

side. All directions are taken as if viewing the vessel from the downstream direction, looking upstream.

To model this vessel, both its static and dynamic state must be described. Its static state can be described by six separate parameters or Degrees of Freedom (DOF). These are the three linear displacements in 3D space to describe the location of the vessel and three angles that describe its state of angular displacement about each axis in 3D space. The dynamic states are the rates of change of the linear displacements and angular displacements. This fully describes the state of the vessel for the purposes of modelling.

For underwater vessels the standard terms for the six DOF are as follows: surge is movement in the fore-aft direction, sway is movement in the port-starboard direction, and heave is movement in the up-down direction. Roll is rotation about the surge axis, pitch is rotation about the sway axis, and yaw is rotation about the heave axis.

3.1.2 Coordinate Frames

When describing the motion of underwater vessels, it is mathematically convenient to define two coordinate frames: the earth-fixed and body-fixed coordinates. In the earth-fixed frame the origin is chosen as a convenient point external to the vessel, and independent of the vessel's motion. Often this is a fixed point on the ocean bed or on the surface. In this case it will be chosen as the point at which the OCEC is tethered to the ocean floor.

The x-axis is defined as the northwards direction, the y-axis is defined as the eastwards direction and the z-axis is defined as the downwards direction. For the purpose of this study, the Earth will be approximated as flat and non-rotating, which is sufficiently accurate for the purposes of this study considering an object that is slow-moving. Since this is the case, the earth-fixed coordinates can be considered to be an inertial reference. These directions will be denoted as X_i, Y_i, Z_i.

The position and orientation of the OCEC should be described relative to the inertial reference, while the linear and angular velocities should be described relative to the body-fixed axes. All rotations are defined as positive in the clockwise direction when facing along the positive direction of the axis. Rotation about the x-axis is denoted ϕ. Rotation about the y-axis is denoted θ. Rotation about the z-axis is denoted ψ.

For the body-fixed reference the origin is usually taken at the centre of gravity (CG) or some other point convenient for calculations. In this case the CG is used as the origin. The x-axis is defined as along the centre of the fuselage, positive in the fore direction. The y-axis is defined as along the quarter chord line of the wing, positive in the starboard direction. The z-axis is defined as positive in the downward direction. These are denoted as X_b, Y_b, Z_b. As stated above the absolute position will only be defined relative to the inertial reference. For the body-fixed frame, only the velocities and forces will be defined. The forces along the X_b, Y_b, Z_b axes will be denoted X, Y,

Z. The moments about these axes will be denoted K, M, N. The linear velocities in X_b, Y_b, Z_b axes will be denoted u, v, w. The angular velocities about these axes will be denoted p, q, r. The vector from the origin of the inertial coordinates to the origin of the body-fixed coordinates is denoted R_0.

In summary, the full state and motion of an underwater vessel can be described by the following vectors according to the SNAME (1950) notation [11]:

$$\eta = \begin{bmatrix} \eta_1^T \\ \eta_2^T \end{bmatrix} = \begin{bmatrix} x & y & z \\ \phi & \theta & \psi \end{bmatrix} \text{(Position and Orientation)} \tag{3.1.1}$$

$$\nu = \begin{bmatrix} \nu_1^T \\ \nu_2^T \end{bmatrix} = \begin{bmatrix} u & v & w \\ p & q & r \end{bmatrix} \text{(Linear and Angular Velocity)} \tag{3.1.2}$$

$$\tau = \begin{bmatrix} \tau_1^T \\ \tau_2^T \end{bmatrix} = \begin{bmatrix} X & Y & Z \\ K & M & N \end{bmatrix} \text{(Forces and Moments)} \tag{3.1.3}$$

3.1.3 Euler Angles and Axis Transformations

It will often be required to perform calculations in either the body reference or inertial reference frames and then to transform from the one reference frame to the other. For the purposes of this study, the convention of the Euler 3-2-1 angles will be used. This means that to transform from the inertial axes to the body axes one must first perform the yaw rotation, then the pitch rotation, and then the roll rotation. It can be shown that to rotate a vector in 3D space about a certain angle is a 3x3 matrix with a 1 in the row and column of the axis about which the rotation is done. It is trivial to show that the angular velocity relationship can be described by:

$$\dot{\eta_2} = \begin{bmatrix} 1 & \sin\phi\tan\theta & \cos\phi\tan\theta \\ 0 & \cos\phi & -\sin\phi \\ 0 & \sin\phi/\cos\theta & \cos\phi/\cos\theta \end{bmatrix} \begin{bmatrix} p \\ q \\ r \end{bmatrix} \tag{3.1.4}$$

To transform the linear velocities, rotation transformations about the three axes must be performed, in the order described above. These are described by the following 3x3 matrices:

$$R_x = \begin{bmatrix} 1 & 0 & 0 \\ 0 & \cos\phi & \sin\phi \\ 0 & -\sin\phi & \cos\phi \end{bmatrix} R_y = \begin{bmatrix} \cos\theta & 0 & -\sin\theta \\ 0 & 1 & 0 \\ \sin\theta & 0 & \cos\theta \end{bmatrix} R_z = \begin{bmatrix} \cos\psi & \sin\psi & 0 \\ -\sin\psi & \cos\psi & 0 \\ 0 & 0 & 1 \end{bmatrix} \tag{3.1.5}$$

These produce a combined transformation as shown by the following:

$$J_1(\eta_2) = \begin{bmatrix} \cos\psi\cos\theta & -\sin\psi\cos\phi + \cos\psi\sin\theta\sin\phi & \sin\psi\sin\phi + \cos\psi\cos\phi\sin\theta \\ \sin\psi\cos\theta & \cos\psi c\phi + \sin\phi\sin\theta\sin\psi & -\cos\psi\sin\phi + \sin\theta\sin\psi\cos\phi \\ -\sin\theta & \cos\theta\sin\phi & \cos\theta\cos\phi \end{bmatrix} \tag{3.1.6}$$

This is otherwise known as the Direct Cosine Matrix (DCM). The practical application of this is that this transformation can be used to transform between the inertial reference and the body-fixed reference in the following way:

$$\dot{\eta_1} = J_1(\eta_2)v_0 \tag{3.1.7}$$

$$\nu_1 = J_1^T(\eta_2)\dot{\eta_1} \tag{3.1.8}$$

As J_1 is a square matrix, its inverse is equal to its transpose.

3.2 Equations of Motion

Since the body-fixed coordinate system is fixed at the centre of gravity, the Coriolis and Centripetal terms can be neglected and the equations of motion can be simplified in the following manner [11]:

Linear accelerations:

$$\dot{\nu_1} = \tau_1/m + \nu_1 \times \nu_2 \tag{3.2.1}$$

Angular accelerations:

$$\dot{\nu_2} = \left(\tau_2 - \begin{bmatrix} (I_{zz} - I_{yy})q.r \\ (I_{xx} - I_{zz})r.p \\ (I_{yy} - I_{xx})p.q \end{bmatrix} \right) \begin{pmatrix} I_{xx}^{-1} \\ I_{yy}^{-1} \\ I_{zz}^{-1} \end{pmatrix} \tag{3.2.2}$$

Where:

m is the mass of the vessel

I_{xx} , I_{yy}, I_{zz} are the moments of inertia about the roll, pitch, and yaw axes.

3.3 Added Mass

When an object is moving through a liquid, that liquid resists the acceleration of the moving object. This is due to the force required to move the liquid out of the way and around the object. This effect is known as "added mass" can be accounted for by increasing the mass or moment of inertia of the object for motion in a particular direction or about a particular axis. While added mass is a complex concept, the simplest way to approximate the added mass is to take the projected area of the shape in the direction of acceleration and draw

a semi-circle with this area as the diameter. The mass of the quantity of water contained within this semi-circle should then be added to the mass of object to give the new mass for the purpose of dynamics calculations. It's important to note that this effect is only observed when the object accelerates. Examples of this explanation are shown in Figure 3.2 for a few simple shapes. If the

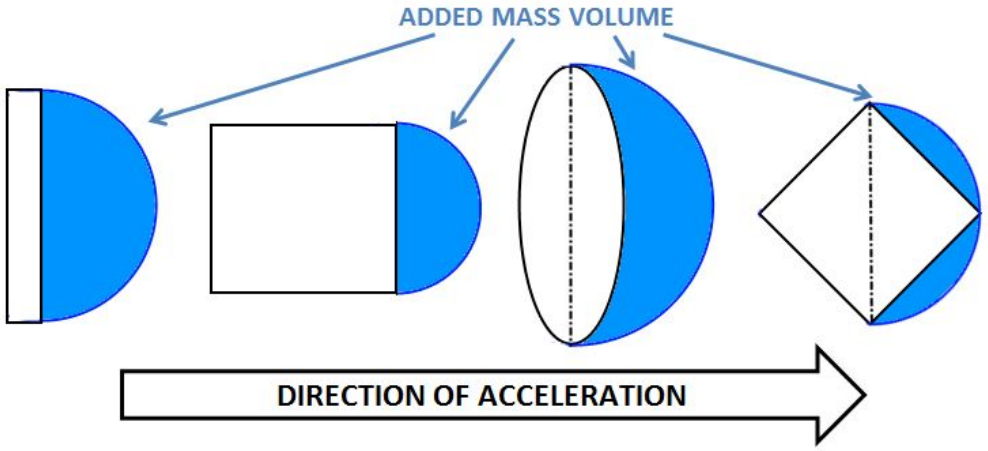

Figure 3.2: Added mass volumes for various simple shapes

object has three planes of symmetry the contribution can be approximated by [11]:

$$M_A = -diag\left[X_{\dot{u}}, Y_{\dot{v}}, Z_{\dot{v}}, K_{\dot{p}}, M_{\dot{q}}, N_{\dot{r}}\right] \tag{3.3.1}$$

Where:

M_A is the added mass matrix

$X_{\dot{u}}$ is added mass for the relationship between force X and acceleration $\dot{u}$

The exact value of each term depends on the shape of the object. It can be shown for a totally submerged ellipsoid described by the function:

$$x^2/a^2 + y^2/b^2 + z^2/c^2 = 1 \tag{3.3.2}$$

that the added mass derivative terms are the following:

$$X_{\dot{u}} = -\frac{\alpha_0}{2-\alpha_0}m \tag{3.3.3}$$

$$Y_{\dot{v}} = Z_{\dot{w}} = -\frac{\beta_0}{2-\beta_0}m \tag{3.3.4}$$

$$K_{\dot{p}} = 0 \tag{3.3.5}$$

$$N_{\dot{r}} = M_{\dot{p}} = -\frac{1}{5}\frac{(b^2-a^2)^2(\alpha_0-\beta_0)}{2(b^2-a^2)+(b^2+a^2)(\beta_0-\alpha_0)}m \tag{3.3.6}$$

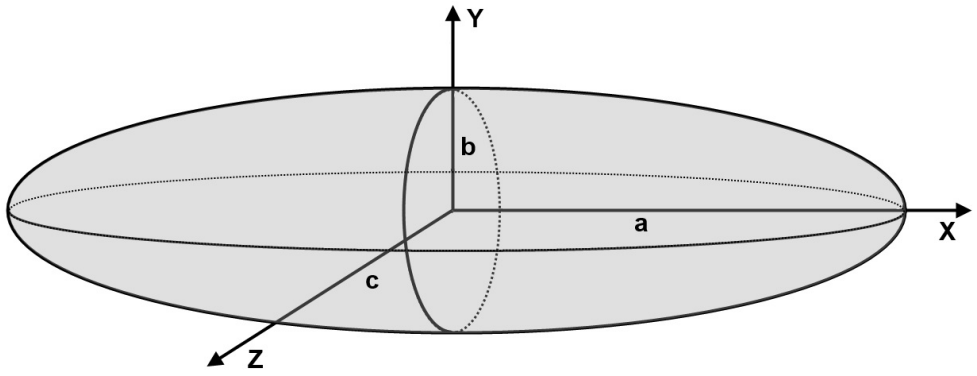

Figure 3.3: Ellispoid with semi-axes a, b, and c

Where the mass of water displaced is:

$$m_w = \tfrac{4}{3}\pi\rho ab^2 \tag{3.3.7}$$

the eccentricity e is defined as:

$$e = 1 - (b/a)^2 \tag{3.3.8}$$

and the constants α_0 and β_0 are defined as [35]:

$$\alpha_0 = \tfrac{2(1-e^2)}{e^3}\left(\tfrac{1}{2}\ln\tfrac{1+e}{1-e} - e\right) \tag{3.3.9}$$

$$\beta_0 = \tfrac{1}{e^2} - \tfrac{1-e^2}{2e^3}\ln\tfrac{1+e}{1-e} \tag{3.3.10}$$

For this study, the shape of the vehicle will be approximated by a set of ellipsoids to simplify the added mass calculation.

3.4 Hydrodynamic Forces

For any object underwater there are forces exerted on the object by the surrounding liquid. These forces can be broadly separated into restoring forces and hydrodynamic damping forces.

3.4.1 Restoring Forces

The forces due to gravity and bouyancy are known as the restoring forces. The gravity force is calculated as follows:

$$\tau_{1G} = J_1^T(\eta_2)\begin{bmatrix} 0 \\ 0 \\ m.g \end{bmatrix} \tag{3.4.1}$$

Where:

τ_{1G} is the gravity force in body-fixed reference

$J_1^T(\eta_2)$ is the transformation matrix from inertial to body-fixed reference

m is the mass of the vessel

g is the gravitational constant

Since this force is acting at the CG there will be no moment as a result. The force due to bouyancy can be calculated as follows:

$$\tau_{1B} = J_1^T(\eta_2) \begin{bmatrix} 0 \\ 0 \\ -V\rho g \end{bmatrix} \tag{3.4.2}$$

Where:

τ_{1B} is the bouyancy force in body-fixed reference

V is the volume of the vehicle

The moment produced by the bouyancy force can be found by:

$$\tau_{2B} = R_{0B} \times \tau_{1B} \tag{3.4.3}$$

Where:

τ_{2B} is the moment about the CG due to the bouyancy force in body-fixed reference

R_{0B} is the vector from the CG to the centre of bouyancy

3.4.2 Hydrodynamic Damping Force

The water provides a resistance force to the motion of the OCEC which can be seen as a damping action. This force can be separated into two components: the tangential force due to skin friction along the surface of the OCEC, and the normal force caused by vortex shedding from the front face of the OCEC. Both of these forces are dependent on the surface area presented to the flow of water, the surface roughness, and the velocity of the water flow. There is also a moment that resists the rotational speed as well. The damping force can be obtained as follows:

$$\tau_{1P} = -J_1^T(\eta_2)\frac{1}{2}\rho \begin{bmatrix} A_B^n C_{Pb}^n u^{rel}|u^{rel}| \\ A_B^t C_{Pb}^t v^{rel}|v^{rel}| \\ A_B^t C_{Pb}^t w^{rel}|w^{rel}| \end{bmatrix} \tag{3.4.4}$$

Where:

τ_{1P} is the damping force in body axes

C_{Pb}^{n} is the normal drag coefficient

C_{Pb}^{t} is the tangential drag coefficient

A_{B}^{n} is the projected cross-sectional area

A_{B}^{t} is the projected tangential area

${\nu_1}^{rel}$ is the relative water speed

$$\tau_{2P}^{b} = -\frac{1}{2}\rho \begin{bmatrix} A_B^t C_{Pb}^t p^{rel}|p^{rel}| \\ A_B^n C_{Pb}^n q^{rel}|q^{rel}| \\ A_B^n C_{Pb}^n r^{rel}|r^{rel}| \end{bmatrix} \tag{3.4.5}$$

Where:

τ_{2P} is the damping moment in body axes

${\nu_2}^{rel}$ is the relative rotational water speed

To simplify calculations, the damping forces of the separate body elements will be calculated individually, and then summed to give the total damping force.

The moments will be calculated by:

$$\tau_{2P} = R_{0P} \times \tau_{1P} + \tau_{2P}^{d} \tag{3.4.6}$$

Where:

τ_{2P} is the moment about the CG due to the damping force in body axes

R_{0P} is the vector from the CG to the geometric centre of each body component

Radiation-induced potential damping and wave drift damping, which have an impact on surface vehicles, can be shown to be negligible for underwater vehicles [11].

3.4.3 Relative Water Velocity

Due to the size of the vehicle, small angular velocities can result in large linear velocities at the extremities of the vehicle. To calculate the hydrodynamic forces at every point on the vehicle the relative water velocity at every point must be determined. This can be calculated as follows:

$$\nu_1{}^{rel} = \nu_1 + \nu_2 \times R_{0X} - V_w \tag{3.4.7}$$

Where:

$\nu_1{}^{rel}$ is the relative water velocity

ν_1 is the vehicle velocity at the centre of gravity

R_{0X} is the vector from the centre of gravity to the point in question

V_w is the speed of the current [36]

3.4.4 Reynolds Number

All the hydrodynamic coefficients are functions of the Reynolds number, which is calculated as follows:

$$R_n = \nu_1{}^{rel} D/\gamma \tag{3.4.8}$$

Where:

R_n is the Reynolds number

D is the characteristic length

γ is the kinematic viscosity coefficient

3.5 Modelling of the Turbine

Three blades rotating in a liquid would clearly be a highly complex system to model the hydrodynamics of precisely. For the purposes of modelling the behaviour of the OCEC a simplified dynamic model is required to reduce the complexity of the analysis. The OCEC's turbines can be thought of as very similar to a wind turbine, only in a denser medium. Common practise for wind turbines [12] is to consider the rotor swept area as a permeable disk that provides a resistance to the flow of air through the area, increasing the pressure at the disk surface and reducing the speed of the air, as energy is taken from it. The assumptions made in order for this simplification to be valid is that the flow is stationary, incompressible, frictionless, and with no external forces acting on the flow either upstream or downstream of the disk. There is also assumed to be no rotational velocity component to the fluid. Various studies have used this method as a reasonable approximation for the dynamics of marine current turbines [13].

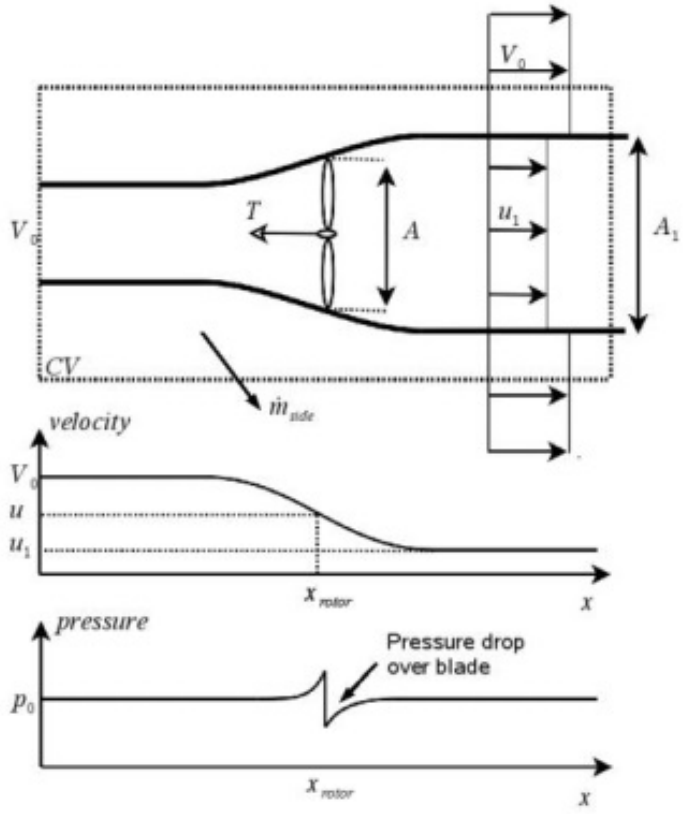

Figure 3.4: Volume control around a wind turbine [12]

This can be used to calculate both the thrust and torque produced on the turbine as shown below:

$$\tau_{1R} = \tfrac{1}{2} C_T \rho {\nu_1^{rel}}^2 A_R^n \tag{3.5.1}$$

$$\tau_{2R} = \tfrac{1}{2} C_W \rho \nu_1^{rel\,3} A_R^n / \omega_R r \tag{3.5.2}$$

Where:

τ_{1R} is the thrust force produced on the turbine

τ_{2R} is the torque produced on the turbine

C_T is the coefficient of thrust

C_W is the coefficient of power

ν_1^{rel} is the relative water velocity

A_R^n is the swept area of the disk

r is the radius of the rotor blades

ω_R is the angular velocity of the rotor blades

Bahaj et al [13] have already conducted experiments measuring the power and thrust coefficients of a similar turbine, and the values obtained in that study will be used for the OCEC model. Their results are shown in Figures 3.5 and 3.6. What can be seen from this study is that the thrust force decreases at

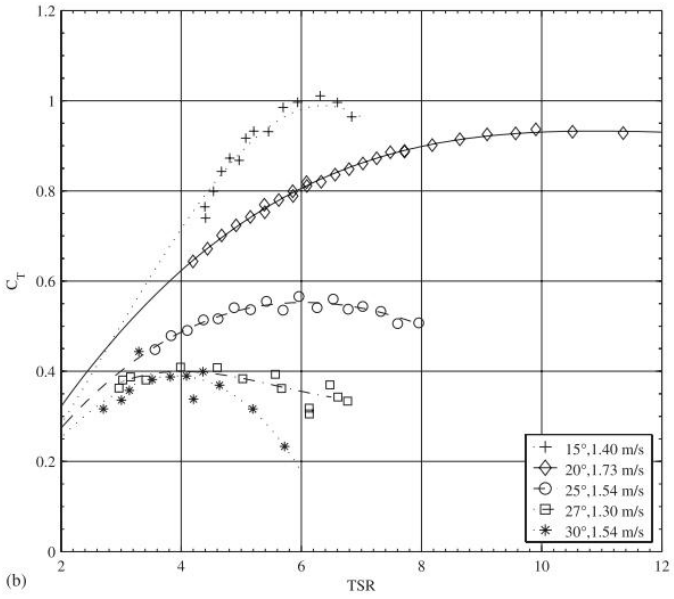

Figure 3.5: Comparison of thrust coefficient C_T for different hub pitch angles, at various tip speed ratios [13]

a rate of close to *cosine* of the yaw angle, which means that it is reasonable to approximate that a permeable disk, when angled against the current flow, has similar behaviour to a rotating turbine. Then in three dimensions, the thrust force generated by the turbine can be calculated in a similar manner to the hydrodynamic damping by:

$$\tau_{1R} = -J_1^T(\eta_2)\frac{1}{2}\rho \begin{bmatrix} A_H^n C_T u^{rel}|u^{rel}| \\ A_H^t C_R^t v^{rel}|v^{rel}| \\ A_H^t C_R^t w^{rel}|w^{rel}| \end{bmatrix} \tag{3.5.3}$$

Where:

C_T is the thrust coefficient

C_R^t is the tangential drag coefficient

A_H^n is the swept area of the rotor

A_H^t is the projected tangential area

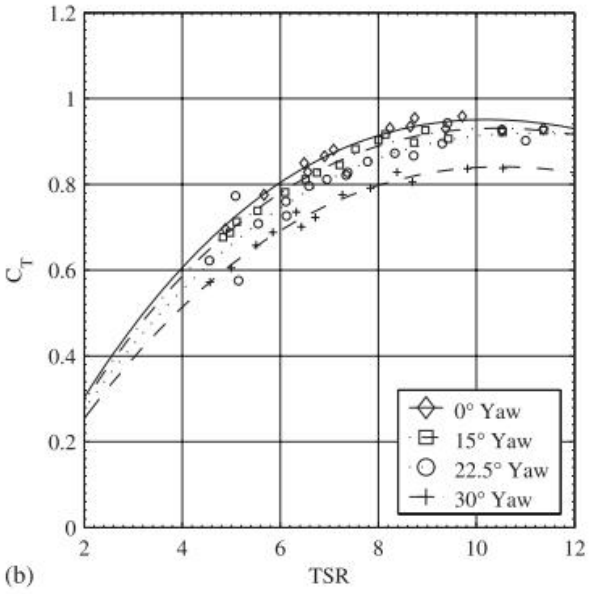

Figure 3.6: Comparison of thrust coefficient C_T for different yaw angles, at various tip speed ratios, for hub angle 20° [13]

3.6 Modelling of Hydrofoil

3.6.1 Introduction

A hydrofoil adds a lift force to the device, that counteracts gravity and the downward tension created by the cable. The significant aspects and forces are shown in Figure 3.7 which shows a typical aerofoil.

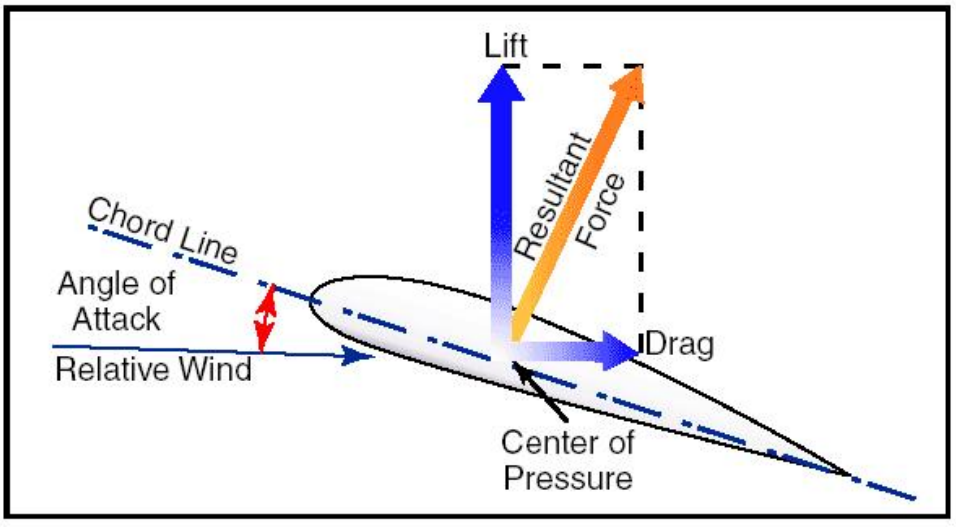

Figure 3.7: Forces on an aerofoil

An aerofoil section works by creating a pressure difference in the fluid on the upper surface and the lower surface, which results in a lift force normal to the water flow. The key factors for the wing are the chord line and the angle of attack (α), which is the angle between the chord line and the relative flow direction.

While this diagram shows an aerofoil in air, the principle for an underwater application is exactly the same, with the main difference being the density of the medium. A characteristic feature of an aerofoil is the phenomenon of "stall". This results in a sharp drop off of the lift force outside of a certain range of angles of attack, an example of which is shown in Figure 3.7. Due to this feature the "unstalled" and "stalled" behaviour will be modelled separately.

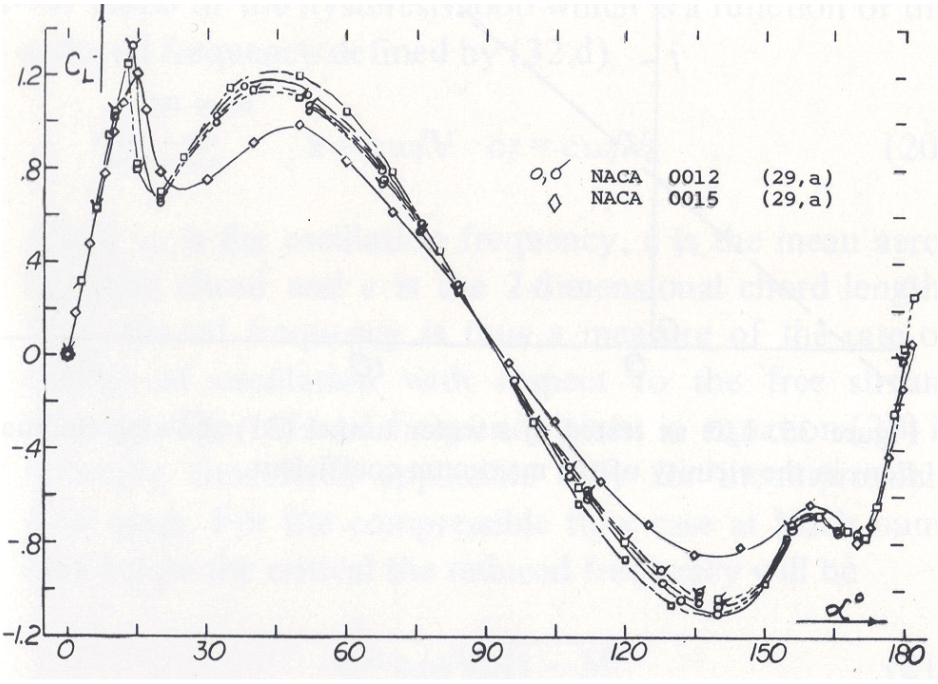

Figure 3.8: Lift coefficient C_L vs. angle of attack α for NACA 0012 profile [14]

3.6.2 Unstalled Behaviour

The lift and drag coefficients are functions of the angle of attack, which will be obtained from a table of values for the NACA 5012 wing profile. See Appendix B.3.

The forces generated by the hydrofoil can be modelled in a similar manner to the hydrodynamic damping forces:

$$\tau_{1H} = -\frac{1}{2}\rho A_w \begin{bmatrix} C_X u^{rel}|u^{rel}| \\ C^t_{Ph} v^{rel}|v^{rel}| \\ C_N w^{rel}|w^{rel}| \end{bmatrix} \tag{3.6.1}$$

Where:

τ_{1W} is the wing force in body axes

C_X is the chordwise force coefficient

C_{Ph}^t is the wing tangential drag coefficient

C_N is the normal force coefficient

A_w is the effective area of the wing

The coefficients are defined as:

$$C_N = C_L cos(\alpha) + C_D sin(\alpha) \tag{3.6.2}$$

$$C_X = C_D cos(\alpha) - C_L sin(\alpha) \tag{3.6.3}$$

Where:

C_L is the lift coefficient

C_D is the drag coefficent

C_L and C_D vary with the angle of attack

The hydrofoil produces a pitching moment about the quarter-chord point of the hydrofoil, which is the point a quarter of the chord length from the leading edge of the wing.

$$\tau_{2H}^p = \tfrac{1}{2}\rho {\nu_1^{rel}}^2 A_W C_M(\alpha) \tag{3.6.4}$$

Where:

τ_{2H}^p is the pitching moment

A_W is the effective area of the hydrofoil

C_M is the moment coefficient

The rest of the moments can be determined as per the regular moment calculations, so the total moment calculation is:

$$\tau_{2H} = \begin{bmatrix} \tau_{1H}^x \times R_{0H} \\ \tau_{2H}^p \\ \tau_{1H}^z \times R_{0H} \end{bmatrix} \tag{3.6.5}$$

Where:

τ_{2H} is the moment induced by the wing about the centre of gravity

τ_{1H}^x is the wing force in the X_b direction

τ_{1H}^z is the wing force in the Z_b direction

R_{0H} is the vector from the centre of gravity to the geometric centre of the wing

3.6.3 Stalled Behaviour

Once the wing goes outside the range of normal operation and becomes "stalled" the behaviour changes. After stalling, the wings will be treated as flat plates and the forces and moments calculated as per the hydrodynamic damping.

$$\tau_{1H} = -\frac{1}{2}\rho A_w \begin{bmatrix} C_H^t u^{rel}|u^{rel}| \\ C_H^t v^{rel}|v^{rel}| \\ C_H^n w^{rel}|w^{rel}| \end{bmatrix} \tag{3.6.6}$$

Moments:

$$\tau_{2H} = R_{0H} \times \tau_{1H} \tag{3.6.7}$$

3.6.4 Wing Flaps

To control the angular rate in the roll direction, wing flaps have been installed. It has been shown [14] that the action of deflecting the wing flap a certain angle shows the same behaviour as changing the angle of attack a proportional amount for deflections of the wing flap $\pm$ <15°.

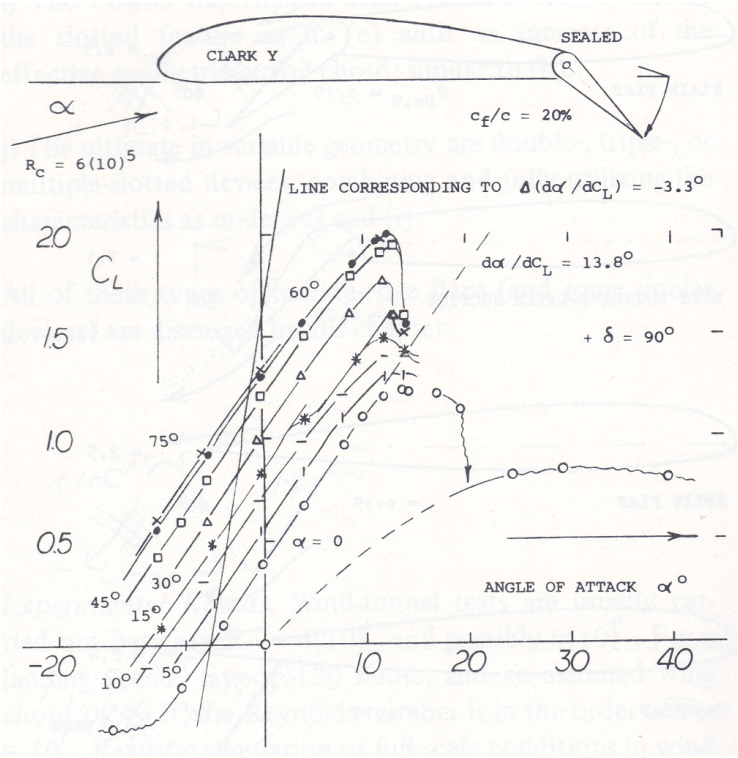

Figure 3.9: Change in C_L due to change in deflection of wing flap [14]

The amount of change in angle of attack due to deflection of wing flap depends on the ratio of the flap chord length to the overall wing chord length.

This relationship can be described by:

$$\alpha' = \alpha + q\delta \tag{3.6.8}$$

Where:

α is the angle of attack

α' is the modified angle of attack

δ is the angle of the flap

q is the constant of effect of flap on angle of attack

3.7 Modelling of Cable

The cable will exert a force on the device, that opposes the lift, buoyancy and drag forces and acts in the direction of the cable. The cable will be modelled using a discretised, lumped mass approach. In this approach, the cable is divided into discrete sections as shown in Figure 3.10. Each section of the

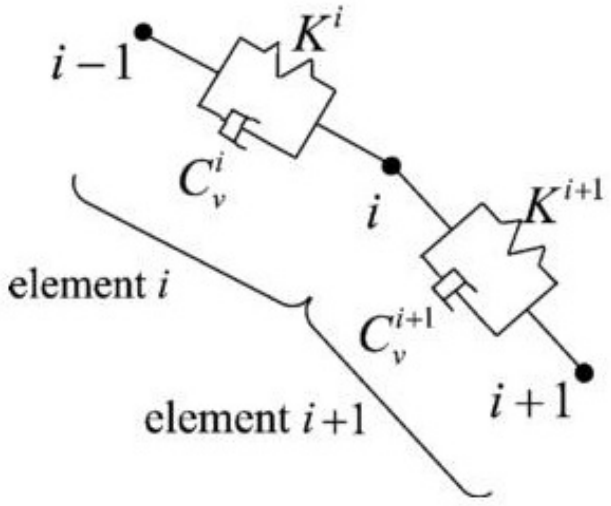

Figure 3.10: The ith element of the discretizes cable is bound by the i-1st and ith nodes [15]

cable is regarded as a straight elastic element with the masses lumped at the nodes. For each cable section the total force can be expressed as follows [15]:

$$\tau_{1C}^{i} = \tau_{1Cs}^{i} + \tau_{1Cd}^{i} + \tau_{1Cr}^{i} + \tau_{1Cg} \tag{3.7.1}$$

Where:

τ_{1C}^{i} is the total force in inertial axes of the ith section

$\tau_{1_{Cs}}^{i}$ is the stretch force in inertial axes of the ith section

$\tau_{1_{Cd}}^{i}$ is the damping force in inertial axes of the ith section

$\tau_{1_{Cr}}^{i}$ is the restoring force in inertial axes of the ith section

$\tau_{1_{Cg}}^{i}$ is the drag force in inertial axes of the ith section

The dynamic behaviour of each node is then modelled as a three DOF object acting under the force of the two sections on either side of it.

In this model there are five discrete sections, with three nodes, and the mooring point fully describing their positions. See Figure 3.11. The force

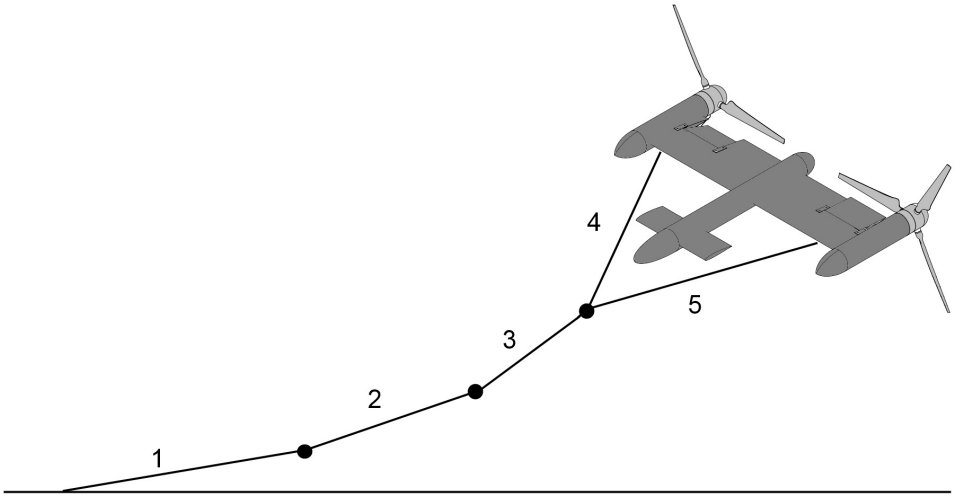

Figure 3.11: Cable elements

exerted onto the vehicle is the sum of the forces from the 4^{th} and 5^{th} section. The moments imposed onto the vehicle by each of the 4^{th} and 5^{th} sections are found as follows:

$$\tau_{2_C}^{i} = \tau_{1_C}^{i} \times R_{0C} \tag{3.7.2}$$

Where:

$\tau_{2_C}^{i}$ is the moment induced by the ith section

R_{0C} is the vector from the CG to the cable tether point

3.7.1 Elastic Force

The spring force is calculated by:

$$\tau_{1_s}^{i} = EA_C(l_s - l)/l \tag{3.7.3}$$

Where:

E is the Young's Elastic Modulus of the cable

A_C is the cross-sectional area of the cable

l is the original length of the cable

l_s is the stretched length of the cable

3.7.2 Damping Force

The damping force is calculated by:

$$\tau_{1_d}^{\ i} = C_d(v_t^i - v_t^{i-1}) \tag{3.7.4}$$

Where:

$\tau_{1_d}^{\ i}$ is the damping force of the ith section

C_d is the damping coefficients

v_t^i is the velocity of the ith element in the tangential direction

Since the tether is a simple system where angle is of no importance, and since there are a number of different cable sections (see later section on tether), it would be inefficient to create a separate axis system for each tether section. Instead the absolute velocity of the cable in the direction of the tether will be obtained using a projection of the inertial velocity of the tether onto the direction of the cable as follows:

$$v^{abs} = norm(u\left(\tfrac{u.v}{u.u}\right)) \tag{3.7.5}$$

Where:

v^{abs} is the absolute velocity in the direction of the tether

u is the unit vector in the direction of the tether

v is the velocity of the tether in inertial axes

The force is then tranformed back into inertial axes by multiplying the absolute force value by the unit vector in the direction of the cable section.

3.7.3 Restoring Force

$$\tau_{1_r}^{i} = \tfrac{1}{2}g(m^i + m^{i+1} - \rho_w vol^i - \rho_w vol^{i+1}) \tag{3.7.6}$$

Where:

$\tau_{1_r}^{i}$ is the restoring force in inertial axes of the ith section

m^i is the mass of the ith element

V^i is the volume of the ith element

For dynamic modelling the added mass must be taken into account, though it is assumed that there is no added mass in the tangential direction. For each element, the added mass in the normal directions is:

$$m_a = \rho_w vol \tag{3.7.7}$$

3.7.4 Drag Force

$$\tau_{1_d}^{i} = -\tfrac{1}{4}\rho d_c l_c \begin{bmatrix} C_n^c f_n (v_r)^2 \frac{v_n}{\sqrt{(v_n)^2+(v_b)^2}} \\ C_n^c f_n (v_r)^2 \frac{v_b}{\sqrt{(v_n)^2+(v_b)^2}} \\ C_n^c f_t v_r |v_r| \end{bmatrix} \tag{3.7.8}$$

Where:

$\tau_{1_d}^{i}$ is the force due to drag

d_c is the cable diameter

l_c is the cable length

C_n is the normal drag coefficient

f_n and f_r are the hydrodynamic loading coefficients

v_r v_n v_b are the relative water velocities at the geometric centre of the cable section

The loading functions account for the non-linear drag transition between normal and tangential directions [15]. They are functions of the relative angle between the cable and the water flow.

$$f_n = 0.5 - 0.1\cos(\eta) + 0.1\sin(\eta) - 0.4\cos(2\eta) - 0.11\sin(2\eta) \tag{3.7.9}$$

$$f_t = 0.01(2.008 - 0.3858\eta + 1.9159\eta^2 - 4.1615\eta^3 + 3.5064\eta^4 - 1.1873\eta^5) \tag{3.7.10}$$

Where η is expressed in radians, and is found by:

$$\eta = \arccos(\frac{u.v}{|u||v|}) \tag{3.7.11}$$

Where:

η is the relative angle between water flow and cable

u is the unit vector in the direction of the cable section

v is the relative water velocity

3.8 Simulation Software

The equations described in these these sections were implemented using Matlab Simulink 6.1 (R14SP1). Embedded M-files were written for the calculations, and then joined with Simulink block diagrams. The simulations were run in an environment using a Fixed-Step 4^{th} order Runge-Kutta solver with a sample time of 0.01 seconds. Figure 3.12 shows the overall block diagram, with controllers implemented. The details of the rest of the nested simulink

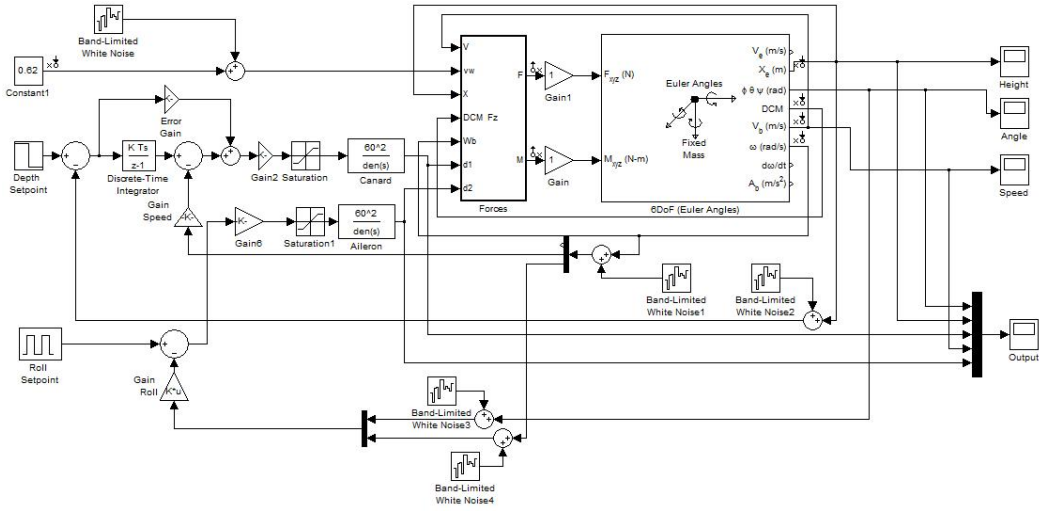

Figure 3.12: Simulink master block diagram

block diagrams contained within the "Force" block are shown in Appendix B.4 and details of the coefficient values used are shown in Appendix B.1.

Chapter 4

Model Verification

4.1 Prototype Design

4.1.1 Detailed Original Concept Description

The Sea Renewable Energy Turbine (SRET), as described in Steven Oldfield's patent [16] and the Stellenbosch University report [37] is a clearly recognisable version of the previously discussed C-Plane concept, and features all of its key elements. As shown in Figures 4.1 and 4.2 there are two counter-rotating

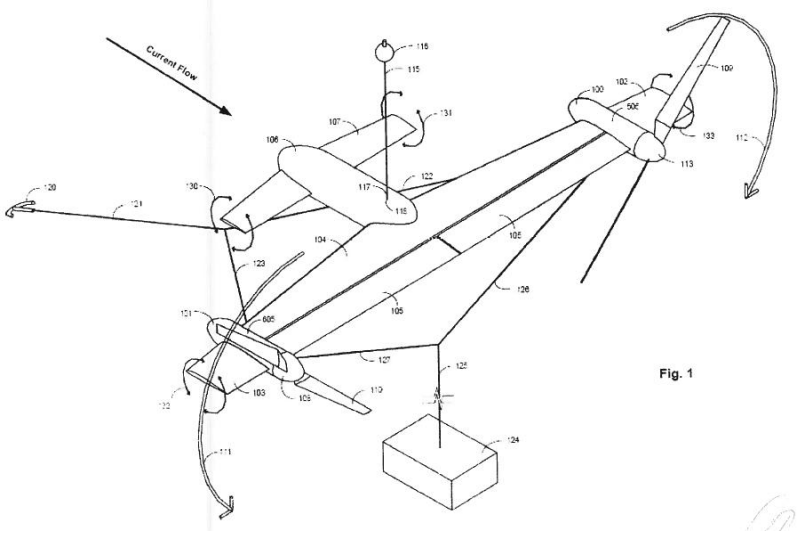

Figure 4.1: SRET top view [16]

turbines, with each turbine driven by two blades, and the generators housed in nacelles. The blades have the ability to change their pitch. The nacelles are joined together by a wing with an aerofoil profile to provide lift. The wings contain movable control surfaces, or ailerons, that span the full length of the wing, and are used to control the roll angle. There is a central fuselage, also attached to the wing, with adjustable nose flaps or canards for pitch

angle control. The SRET is attached to the seabed by a pair of "Y" shaped

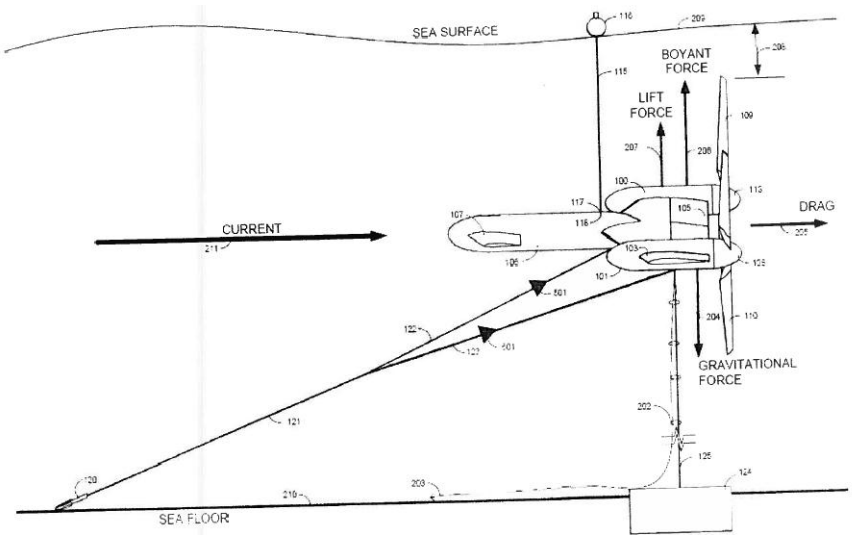

Figure 4.2: SRET side view [16]

tethers, one going directly downwards, and the other angled forwards, with both attached to the underside of the wings. There are adjustable wing tips on the outer sides of the nacelles which are also used for fine roll angle control. A recovery buoy is tethered to the top of the nacelle, and floats on the surface to allow for quick location and recovery of the SRET.

4.1.2 Limitations and Design Considerations

When considering the practical implementation of this design, certain limitations were taken into account. The size and performance of the testing facility was the main consideration to be accounted for. The Stellenbosch Towing Tank, which is described in Section 4.2, was the facility used, and the prototype design had to account for its limitations. Minimising cost is always a factor for a student project, and utilising existing proven designs and hardware was a strong consideration to ensure reliability of the prototype. There was also some leeway given to modify the design where it was felt the concept may not be practical. Safety of the testing personnel was also given top priority in the prototype and test procedure design.

4.1.3 Final Design

The final design that was used for the prototype is shown below in Figure 4.3. It contains the key features of the SRET, while taking into account the limitations mentioned in Section 4.1.2.

There are two counter-rotating turbines with nacelles to house electrics and three blades each. A three blade concept was chosen over a two blade

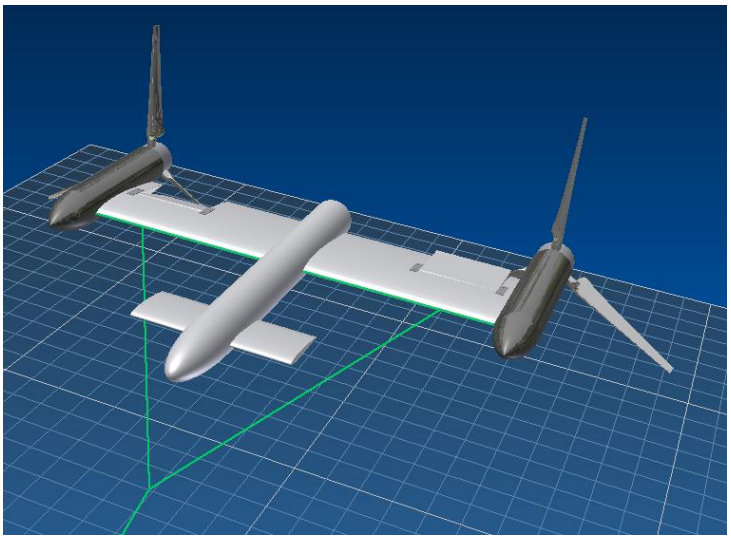

Figure 4.3: Ocean Current Energy Convertor design

model to improve stability. In this prototype the wing is split into two, separated by the central fuselage, and attaches the nacelles to the fuselage. This was done to improve the robustness and rigidity of the body. The fuselage was also increased in size to allow for the housing of all sensor and drive electronics. The wings contain adjustable ailerons, which were located near the nacelles to allow for the maximum moment and to minimise flow disruption due to turbulence. The two ailerons' movement is linked such that they move together, in opposite directions. This was done to simplify the roll control action. There are two adjustable canards attached to the fuselage towards the nose. These canards are linked and move in unison. There is a single "Y" tether attached to the front of the wings, and directed at a forward angle to the seabed tether point. A single tether was selected to allow for more freedom of movement for the prototype. The adjustable wing tips were removed for purposes of simplicity and practical considerations of their effectiveness, given the turbulence created by the blades. The blade pitch is fixed to reduce complexity and the recovery buoy was not used as this would have no major impact on the dynamics of the prototype. The blades are passively driven, rather than motor driven for safety purposes as well as to reduce weight and complexity.

4.2 Testing Facility

The Stellenbosch University Towing Tank was built in 1979 with the primary purpose of testing novel boat hull designs. It consists of a 90 m long, 2.4 m deep, 4.6 m wide concrete tank with rails running along the tops of the walls of the tank and viewer windows built into the walls. On the rails runs an aluminium frame trolley consisting of four individually driven 10 kW motor-

Figure 4.4: Stellenbosch University Towing Tank

driven wheels, run from a 55 kW variable speed drive, housed in a panel on the trolley. The speed of the trolley can be varied by 0.1 ms^{-1} increments up to 9.0 ms^{-1} with 0.05 ms^{-1} tolerance on the speed. The speed is regulated by an encoder on the wheels which feeds back to the controller. The trolley is driven from a control panel on the driver's platform, which is surrounded by safety rails. There are also built-in on-board sensors, including a load cell and two

Figure 4.5: Stellenbosch University Towing Tank Trolley

linear transducers, which are connected to a bridge rectifier unit that can be connected to a computer. There is a shelf with power outlets on-board where a computer can be housed. The water is freshwater, maintained by chlorine. The facility is at 121 m above sea level [38], with a typical barometric pressure

of 1,014 kPa [39]. Though this was not used for this project, the facility also has the capacity to generate surface waves of controlled frequency.

4.3 Testing Procedure

For each test run, the prototype was lowered into the water at the back of the trolley. It was attached to the tether cable, and supported by fishing line at strategic points to hold it above the tank floor and control the starting angle. The setup is shown in Figure 4.6. Before each day of testing the load cell

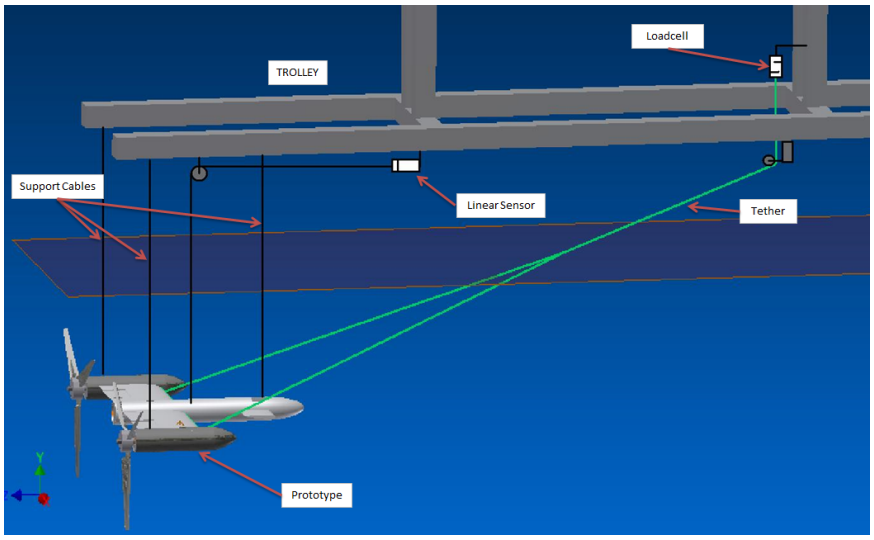

Figure 4.6: Test Setup

and linear sensors would be calibrated to external reference points. Since the load cell was particularly susceptible to drift, it would be checked again at the end of a day of test runs. The prototype would be lowered into position in the water, all sensor systems would then be activated and checked that they were giving correct outputs, the tank would be checked for obstructions, the siren would be sounded, the trolley set to the setpoint speed, and then the trolley would start. To avoid any issues with turbulence or drag from a long pole, the tests were run with the prototype inverted, i.e. upside down, so that the tethered point on the trolley was equivalent to a fixed point on the seabed. The weight also needed to be adjusted so that the expected bouyancy of the final device was simulated by the weight of the prototype (creating a downward force equivalent to the real life upward force).

Some practical considerations had to be taken into account during the prototype testing. The first was that the speed of the trolley drive varied during the runs. Due to the drive behaviour the speed would be auto-corrected every second leading to a constant adjusting of the speed. A typical speed profile is shown in Figure 4.7.

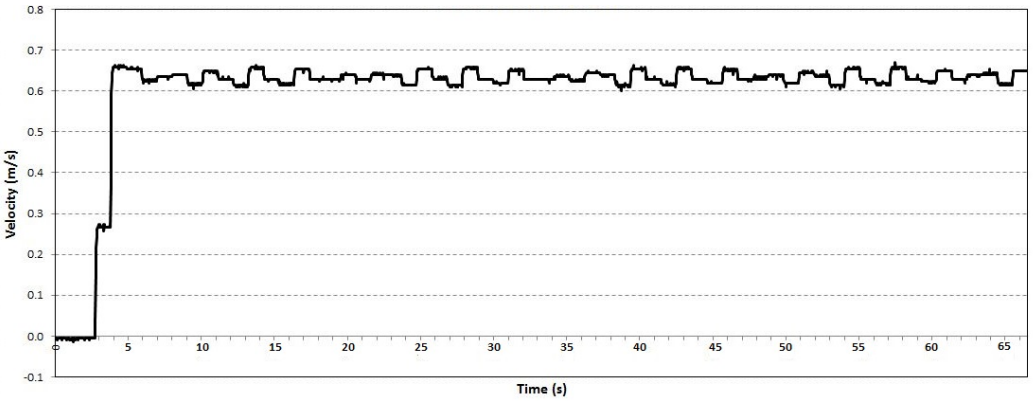

Figure 4.7: Trolley velocity vs. time

The speed varied up to 0.05 ms^{-1} during a run, which would have an influence on the behaviour of the prototype. It was also quickly discovered that the driven turbine blades were difficult to control in terms of keeping their rotations identical, so for the majority of the tests the blades were replaced with Perspex disks of an equivalent drag. There were also difficulties experienced with water ingress into the prototype, interfering with the electronics and affecting the weight balance of the prototype. This resulted in some difficulties obtaining data from the on-board sensors, and occasionally affected the behaviour of the control surfaces. Allowances also had to be made for weight balance. To ensure the accuracy of the data produced each run was repeated several times to verify the results. Obvious outliers were disregarded and all valid runs were averaged to obtain the most reliable result. Details of prototype construction can be seen in Appendix A.1.

4.4 Test Results

A number of tests were run to acquire actual case data to be used to verify the simulation results. The results of those tests are summarised below with a brief analysis of the key points noted from each set of results.

4.4.1 Vertical Motion

When the water flow is started the vessel rises smoothly and settles to a largely stable setpoint, as can be seen in Figure 4.8. Even without control feedback the dynamic response is stable and has many ideal characteristics. A stable setpoint is reached, though the vessel is not strongly held in this position, and drifts in depth within 12% of the settling point. On average the vessel settles to a position 610 mm below the surface, within 20 s. Features of the dynamic response are a marked overshoot of the settling point by around 15% with the peak at 10 s. Another feature is a “pause” in the vertical motion

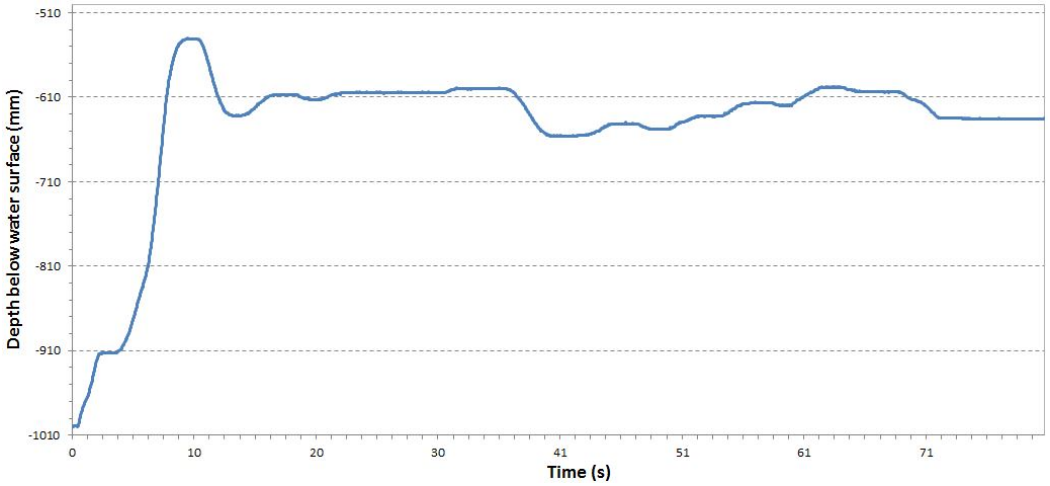

Figure 4.8: Vertical motion at 0.62ms^{-1}

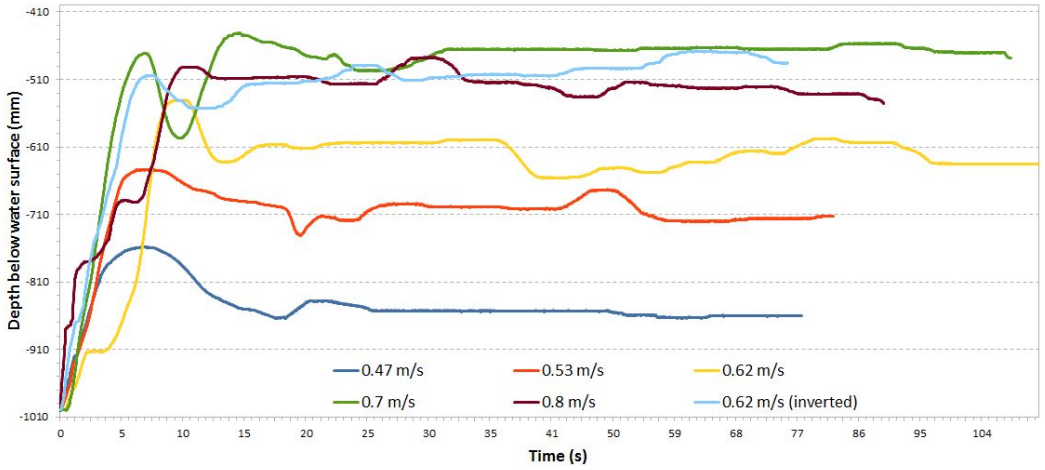

Figure 4.9: Vertical motion at different flow velocities

at around 3 s. Once in motion the vessel is in a stable equilibrium and returns to within the settling point range again within 20 s.

The vessel was tested at different flow velocities to assess how the response varied. As can be seen in Figure 4.9 the depth of the settling point varies with flow velocity, with faster flow velocities having the vessel closer to the surface, while at slower velocities the vessel settles at a lower depth. The dynamic characteristics are very similar at each flow velocity with the characteristics mentioned above: damped response, marked overshoot, "pause" in vertical motion, and settling to a stable point. An interesting feature is that while the settling time varies according to the flow velocity, the overshoot peak time is consistent across the different flow velocities. Below is a table showing the average results for each flow velocity. Test runs were also done at 0.62 ms^{-1} with the vessel inverted. The purpose of these tests was to evaluate the difference due to the wing lift force. As can be seen it was found that there

Table 4.1: Depth and settling time vs. flow velocity

Flow Velocity (ms^{-1})	Settling Depth (m)	Settling Time (s)
0.47	-863	24
0.53	-699	20
0.62	-605	18
0.63(inverted)	-465	24
0.70	-516	15
0.80	-507	14

is a marked difference in the depth when the vessel is inverted, which is consistent with the hydrofoil lift theory.

4.4.2 Tether Force

Figure 4.10 shows a typical plot of the output of the trolley load cell, attached to the vessel tether at 0.62 ms^{-1}. A key feature of the tether force response

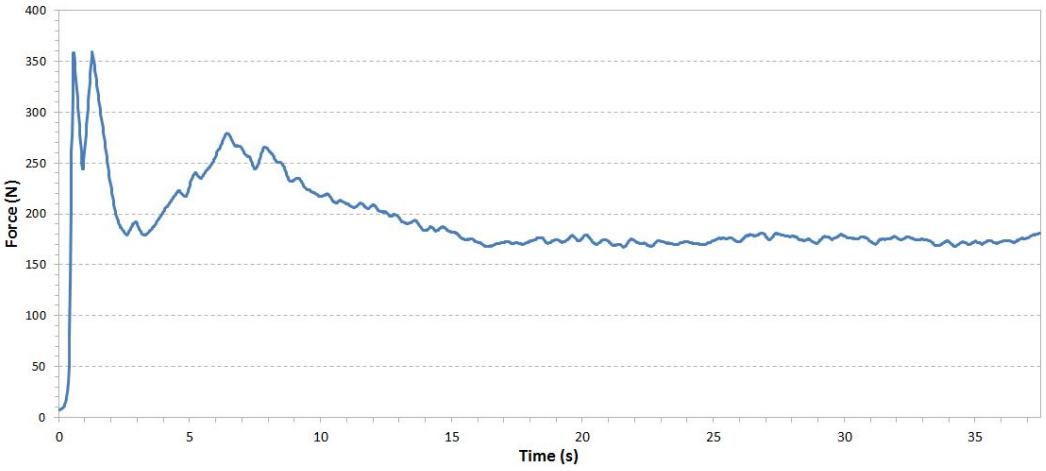

Figure 4.10: Tether force at 0.62ms^{-1}

is the initial spike when the inertia of the vessel is being overcome, which then drops off sharply. There is immediately afterwards a secondary, more sustained peak during the time that the vessel is rising to its settling position. At the settling position the force is generally constant, varying not more than 5% during normal motion. The average tether force was measured for different flow velocities and different actions of the control surfaces. The results are shown in Table 4.2.

The force is roughly proportional to the square of the flow velocity, which is consistent with the predictions of drag force theory. The inverted state shows an increase in force, which is due to the change in pitch angle which results in an increase in the surface area perpendicular to the flow. The force

Table 4.2: Average force vs. flow velocity

Flow Velocity (ms^{-1})	Canard	Aileron	Average Force (N)
0.35	0°	0°	67.6
0.47	0°	0°	111.3
0.53	0°	0°	137.7
0.62	0°	0°	174.4
0.62	+30°	0°	176.1
0.62	-30°	0°	182.4
0.62	0°	25°	176.0
0.62	inverted	inverted	184.9
0.70	0°	0°	219.3
0.80	0°	0°	280.0

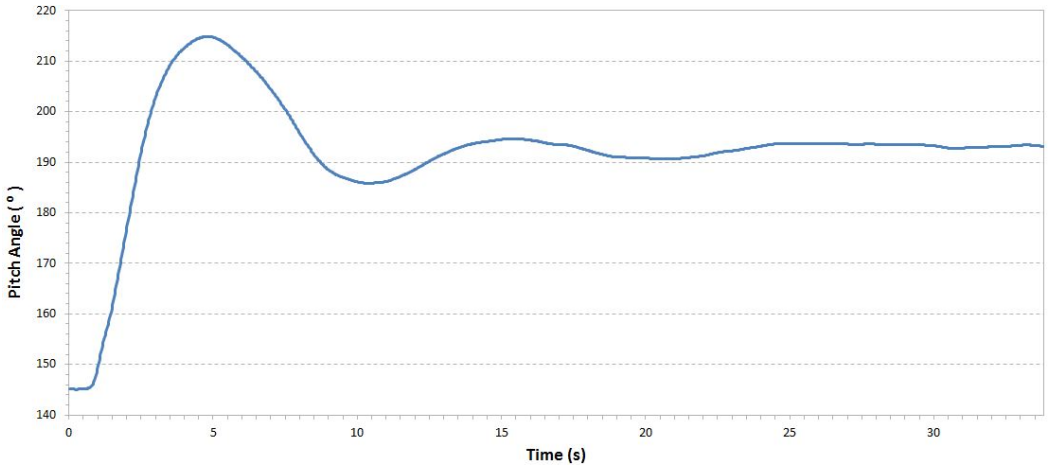

Figure 4.11: Pitch angle motion at $0.62ms^{-1}$

at activated state of the control surfaces shows minor changes. For canards at -30° the pitch angle is reduced, but this is offset by the increased resistance of the canards in their activated state. With canards at +30° the force is larger, due to the increase in pitch angle. With ailerons activated there is little difference in the force, as the pitch angle is not affected.

4.4.3 Pitch Angle Motion

The typical pitch angle response is shown in Figure 4.11. The angle settles to the average settling point of 14° within 30 s. The response is consistent with a second-order under-damped response. There is an overshoot of under 44% and oscillations at a frequency of 0.182 Hz. The pitch angle is stable, and returns to the settling point if disturbed. The key to this study is the fact that the vessel is stable in pitch, and rejects disturbances returning to the settling point. This is encouraging as it suggests that the depth of the

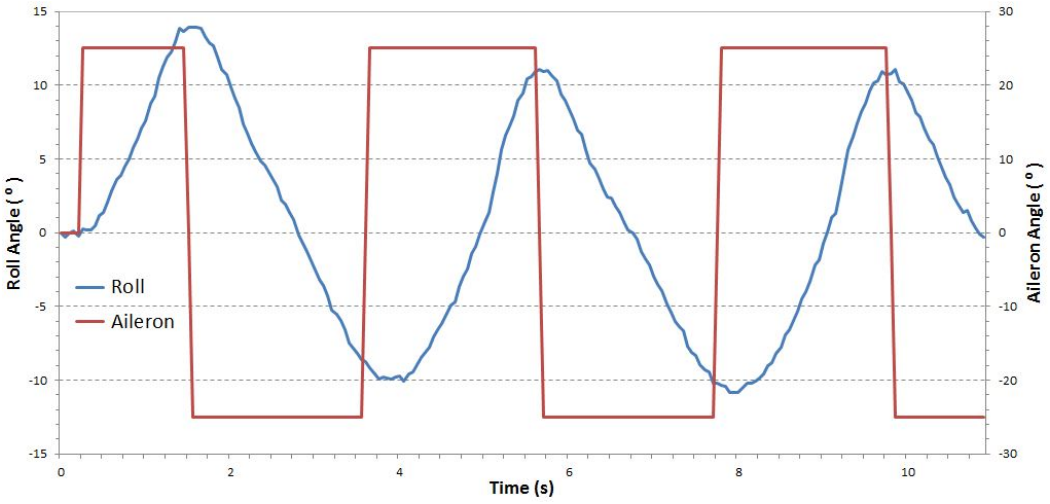

Figure 4.12: Roll angle motion with alternating ailerons

vessel will be controllable since the pitch angle is stable.

4.4.4 Roll Motion

To test the rolling motion response, the ailerons were activated alternately as shown in Figure 4.12. This method was used because once the vessel began to roll in one direction it would continue to roll and not stabilise to a settling point that could be easily assessed. While the vessel was rolling left and right the depth remained quite stable.

At the point of aileron activation, the vessel began to roll at a constant angular acceleration. It is notable that the motion starts as a second-order response, but quickly stabilises to a linear response. This is consistent with drag force theory, due to the interaction between the roll force and the damping force. It is also notable that when alternately activating the ailerons the roll angle stayed quite stable, which is an encouraging result in terms of the ability to control the roll angle.

When a roll motion takes place the depth is also affected. As shown in Figure 4.13 the depth increases as the vessel is rolling. This seems counter-intuitive as aerofoil lift theory would suggest that the vessel should rise, but this is a reflection of the significant impact of the pitch angle on the depth. It was found that the pitch angle decreased slightly during roll motion, leading to a lower settling depth. It is also notable that there is no "bouncing" evident in the depth measurement, even though the vessel is rolling from side to side. This is investigated further in the simulation.

4.4.5 Yawing Motion

The motion in the yaw axis is extremely stable and the vessel returns aggressively to the neutral position when disturbed. This behaviour is shown in

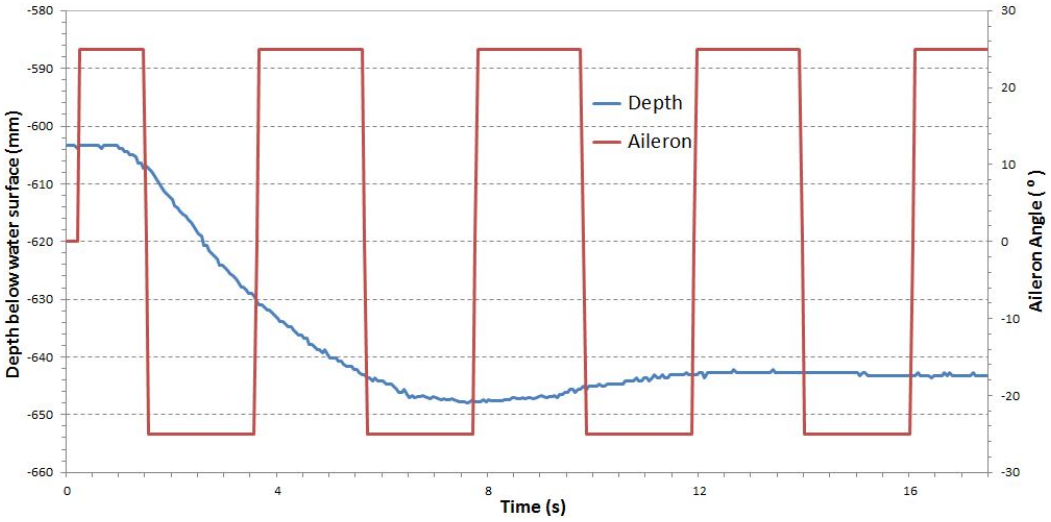

Figure 4.13: Vertical motion with alternating ailerons

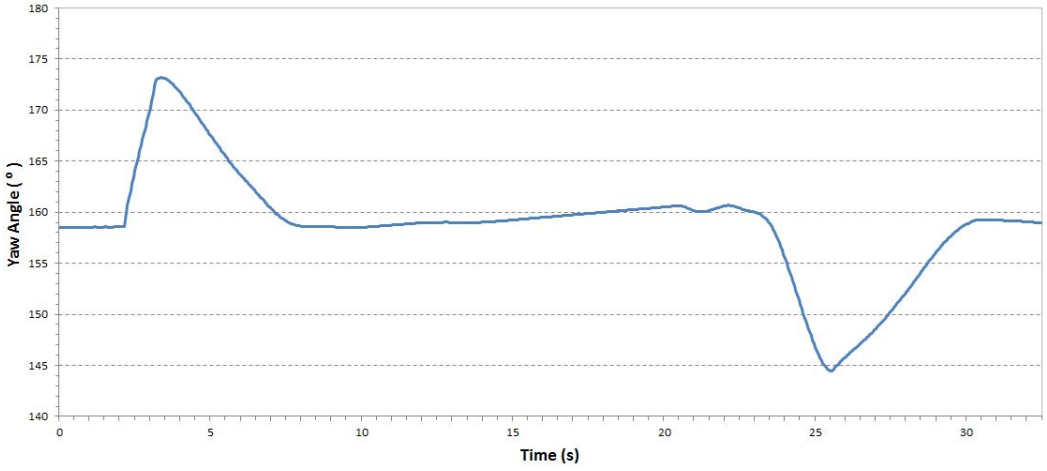

Figure 4.14: Yawing motion due to disturbance

Figure 4.14 where the vessel was disturbed from neutral in the yaw angle and the response was measured. As demonstrated the vessel returns to neutral with minimal overshoot within 7 s.

4.4.6 Canard Response

When the canards are activated the pitch angle of the vessel is affected. A typical response is shown in Figure 4.15.

With canards activated, the vessel will settle to a new angular settling point. The depth will also vary with the pitch angle as shown in Figure 4.16. As expected, when the pitch angle is increased in a positive direction the depth is reduced, and in the negative direction the depth is increased. It is worth noting that there is a maximum limit of an angle that the pitch can

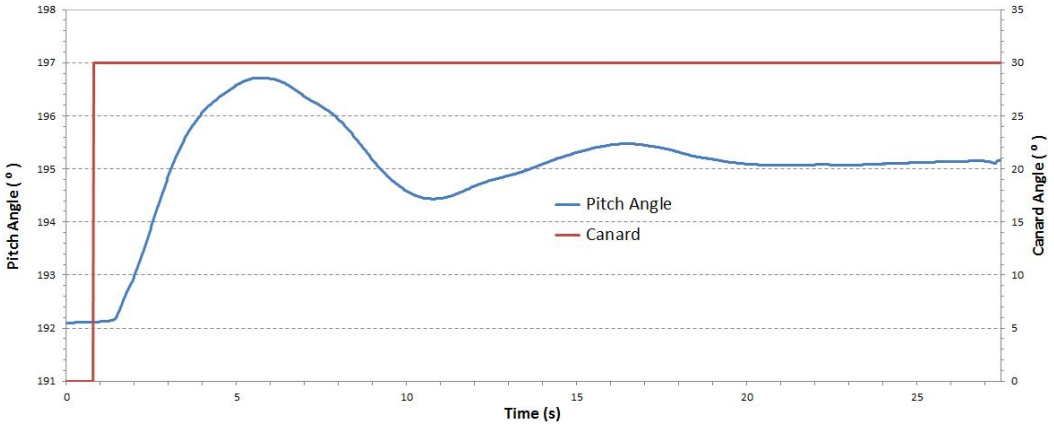

Figure 4.15: Pitch angle motion due to canard action +30°

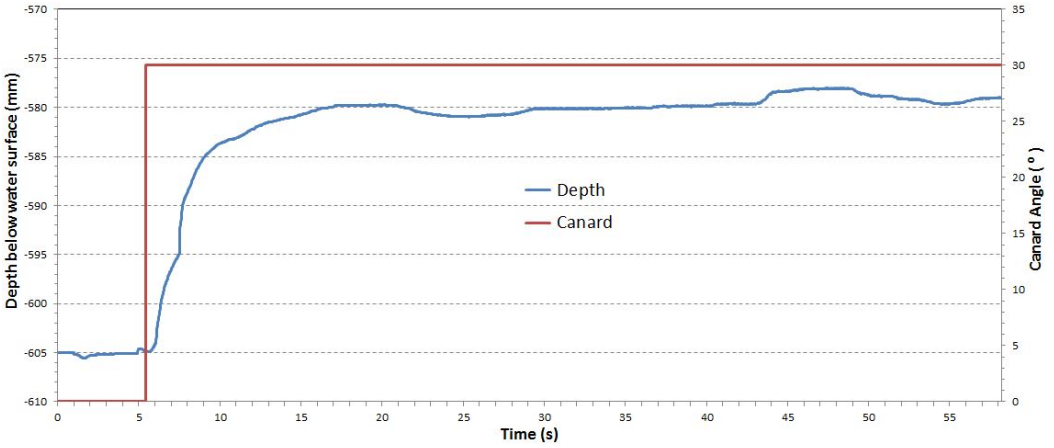

Figure 4.16: Vertical motion due to canard action +30°

be set to, and given the limited range of the pitch angle, the variability of the depth is also limited. The same tests were conducted with the canards activated to -30° with the responses shown in Figures 4.17 and 4.18. The angular response is quite consistent with the response found in Section 4.4.3, with similar overshoot, frequency, and settling characteristics. The depth responses are even more damped than those from Section 4.4.1. This may be due to the small changes in depth experienced.

4.4.7 Testing Challenges

The testing phase of this project proved very time consuming, with a number of difficulties encountered with the prototype, which resulted in delays and numerous repeats of test runs. Though some challenges were to be expected given that this test platform was entirely original and untested, the impact proved greater than anticipated. The key area of challenge was water ingress. Despite many attempts at different methods of waterproofing, water ingress

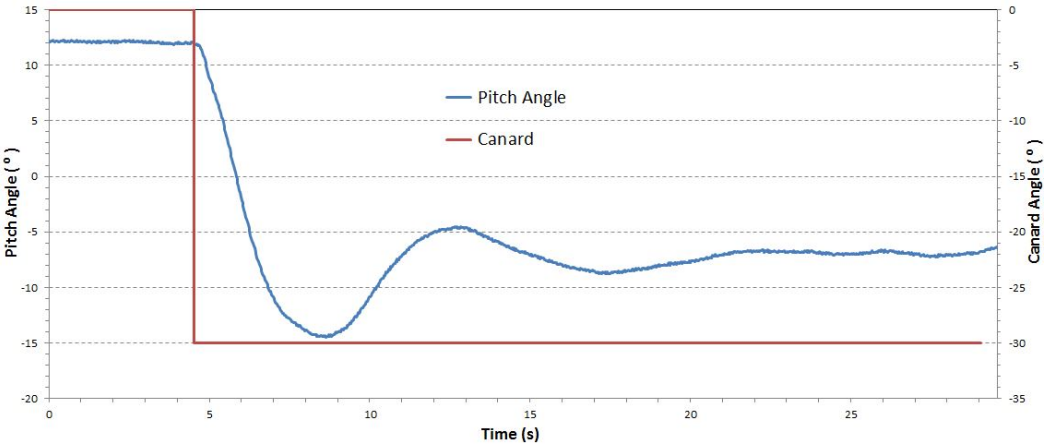

Figure 4.17: Pitch angle motion due to canard action -30°

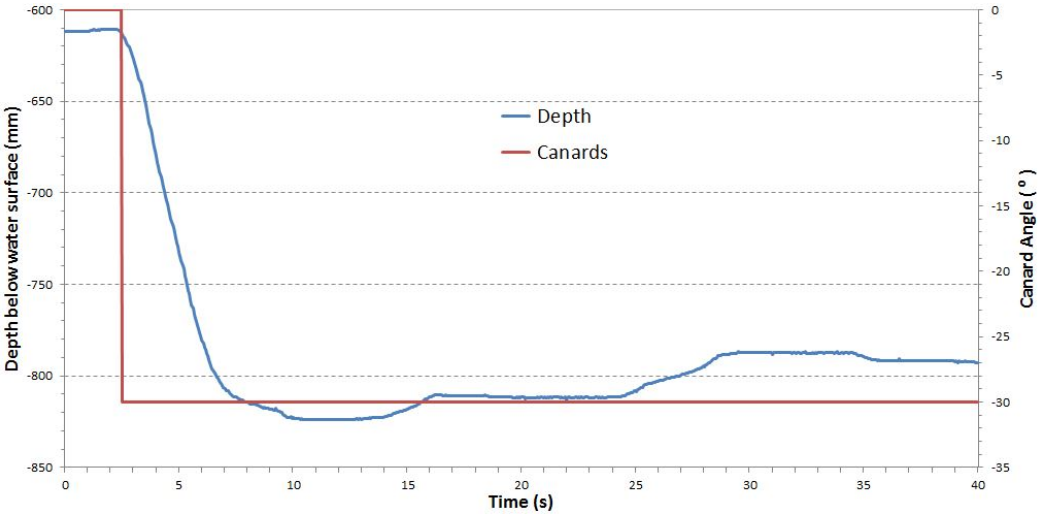

Figure 4.18: Vertical motion due to canard action -30°

remained a problem throughout testing. This had two major impacts on the testing process. Firstly, water would affect the electronics on the prototype, resulting in erratic behaviour of the servomotors controlling the control surfaces, or shutting down the onboard gyro sensor. Secondly, the balance of the vessel was affected, as water leaked in unevenly at different points, resulting in either an aft to fore imbalance, starboard to port imbalance, or both. Continually having to account for these problems resulted in many test runs being invalidated and having to be repeated, and significantly lengthened the time taken for testing. The second major challenge area was the effect of the launching and damage prevention cables. Cables were attached to the vessel (as shown in Figure 4.6) to allow for level launching and preventing damage, however, it was found that these cables had an influence on the movement of the vessel. This lead to anomalies in the test data, which were later found to be due to the cables, and the tests had to be re-run. Finally, there were some

challenges due to the limitations of the facility. Maintenance problems were encountered during testing, which lead to delays. The variability of the run speed (as shown in Figure 4.7) also lead to uncertainty about the validity of certain test data.

4.5 Simulation versus Actual

A program was written using the theory from Chapter 3 in Matlab Simulink including the Aerospace Toolbox to create a simulation that would predict the behaviour of the vessel in experimental cases. The results are shown in the sections that follow with the simulation results plotted against the actual results from Section 4.4.

4.5.1 Vertical Motion

First, the vertical motion was simulated, as shown in Figure 4.19. As can be

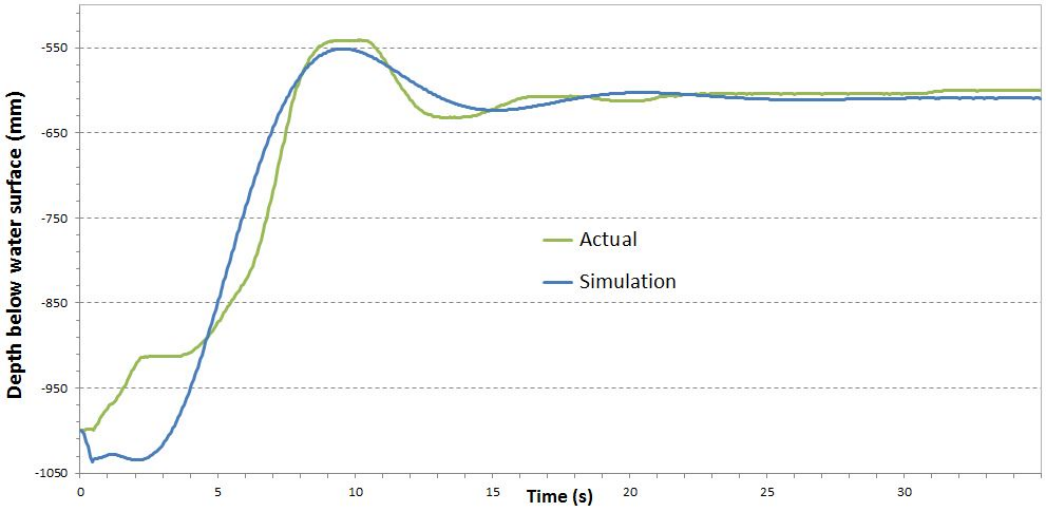

Figure 4.19: Vertical motion - simulation vs. actual

seen the dynamics are quite similar, with overshoot, peak time and settling time well predicted. A note is that the simulation does not experience the "pause" noted at 3 seconds on the actual. It is theorised that this is due to the support cables that prevented downward motion at the start of each run. In the simulation, the vessel first went down before beginning to rise. It is likely that the more "extreme" motions shown in the actual measurements are due to the sensor being slightly offset from the exact centre of the vessel, and so experiencing "rocking" as the angle changes. Simulations were also done at different flow velocities, as per Section 4.4.1. A summary of the results is shown in Table 4.3.

Table 4.3: Depth - simulation vs. actual

Flow Velocity (ms^{-1})	Depth Simulation (mm)	Depth Actual (mm)	Error (%)
0.47	-873	-863	-2.7%
0.53	-732	-699	-9.0%
0.62	-610	-605	-1.4%
0.70	-549	-516	-9.0%
0.80	-505	-507	0.5%

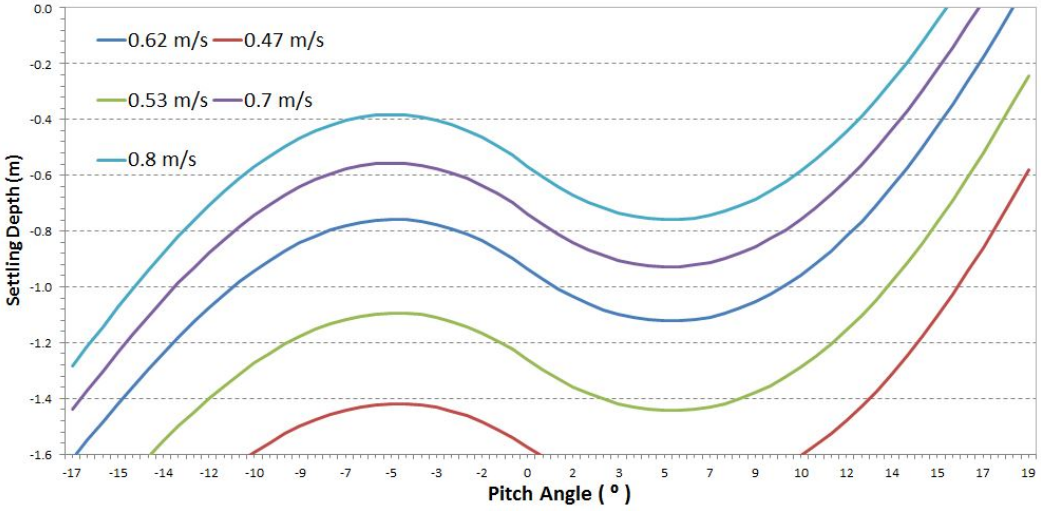

Figure 4.20: Comparison of settling depth vs. pitch angle for various flow velocities

As shown there is a good correlation between simulation and actual, with the error never more than 10% in this flow velocity range. Considering the results from Section 4.4, an analysis was done of the settling depth versus pitch angle. The correlation is shown in Figure 4.20. There are some very interesting features of this relationship. Firstly, it can be seen that in the area of the setpoint angle (7 to 20°) there is a large effect of a change in the pitch angle on the settling depth. Even a change of 1° can result in 100 mm depth change. This would suggest that the pitch angle is the overriding factor when it comes to determining the settling depth of the vessel. There is also a very interesting result that around the 0° point the relationship is counterintuitive; as the pitch angle increases, the settling depth actually decreases. Once the pitch angle gets beyond 6° though the relationship becomes closer to what one would expect. The reason for this is due to the interplay between the drag force and the lift force. As the pitch angle increases the lift force increases, but the drag force also decreases due to the smaller surface area being presented to the current, and since for small angles the drag force is much larger than the lift force, the decrease overrides the increase in lift. This graph also shows the

Table 4.4: Force in tether - simulation vs. actual

Flow Velocity (ms^{-1})	Average Force Simulation (N)	Average Force Actual (N)	Error (%)
0.35	68.0	67.6	0.6%
0.47	108.0	111.3	-3.0%
0.53	133.0	137.7	-3.4%
0.62	175.0	174.4	0.3%
0.70	221.0	219.3	0.8%
0.80	288.0	280.0	2.9%

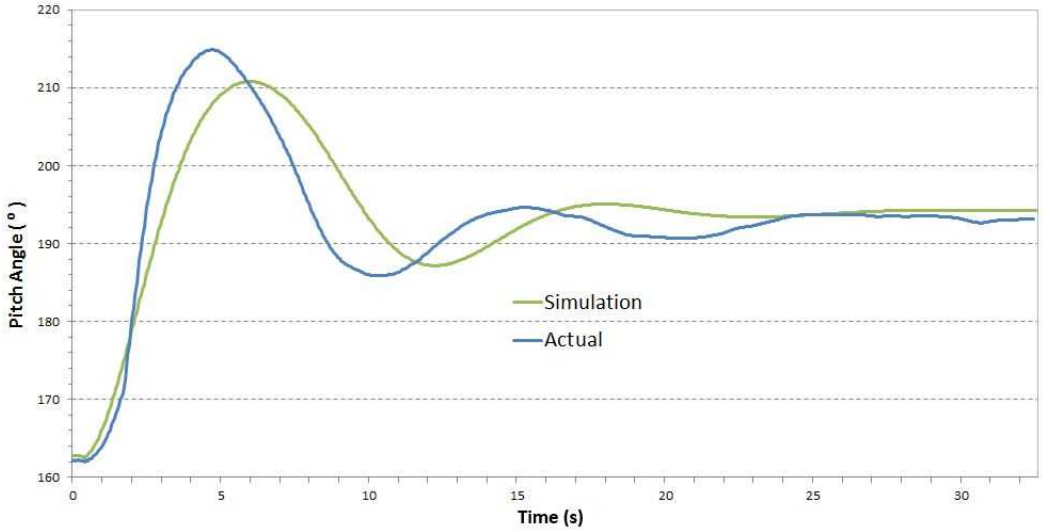

Figure 4.21: Pitching angle motion - simulation vs. actual

change when the flow velocity is altered. As can be seen for lower velocities the settling depth is deeper and for higher velocities the depth is shallower, though the characteristic relationship described above still remains.

A comparison was also done of the tether force for various flow velocities in the simulation, and the results from the simulation were found to correlate well with the actual results. The comparison is shown in Table 4.4.

4.5.2 Pitching Motion

Next the pitch motion was simulated, with results shown in Figure 4.21. Once again, there is good correlation between the responses. The peak, settling time, and frequency are within 10% of the actual data. The discrepancy could be due to inconsistencies in the flow velocity experienced during testing. The frequency of the pitching motion was found to be dependent on flow velocity.

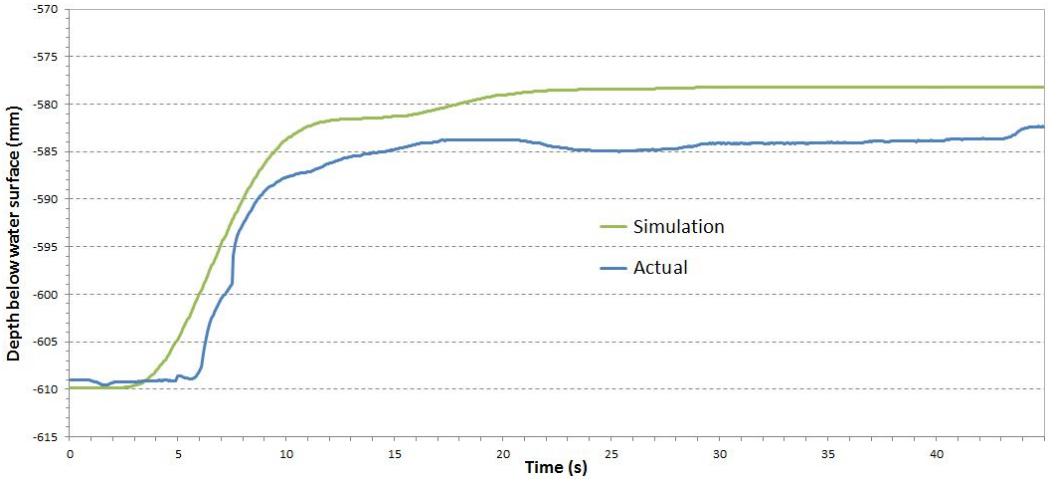

Figure 4.22: Vertical motion due to canard action +30° - simulation vs. actual

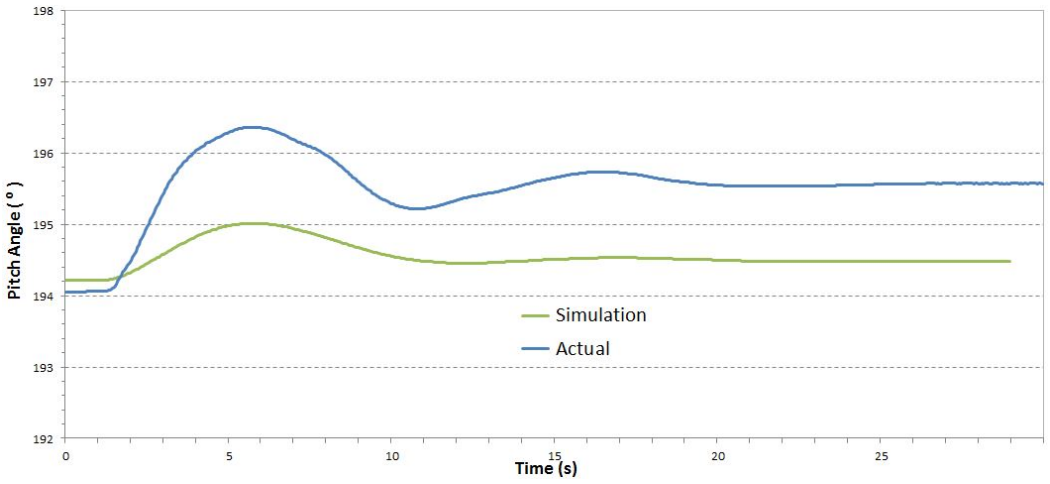

Figure 4.23: Pitch angle motion due to canard action +30° - simulation vs. actual

4.5.3 Canard Response

Next the response to canard action was simulated. The results are shown in Figures 4.22, 4.23, 4.24, and 4.25.

The depth response shows a very good correlation. The settling depth, settling time and overshoot compare very well. With the canards actuated to +30° the depth decreases by 30 mm (25 mm actual). For the pitch angle, from Figure 4.23 it appears that there is a discrepancy. While the settling time is comparable, the final settling angle appears to differ. However, upon closer examination this is purely because of the scale of the graph. The angle change is actually quite small (0.3° simulation, 1.7° actual), so the scale of the graph is misleading, and the results are actually quite close. It is interesting to note that even with a large change in the canard angle, the pitch angle change is quite small. This could be due to the fact that since the Trim pitch

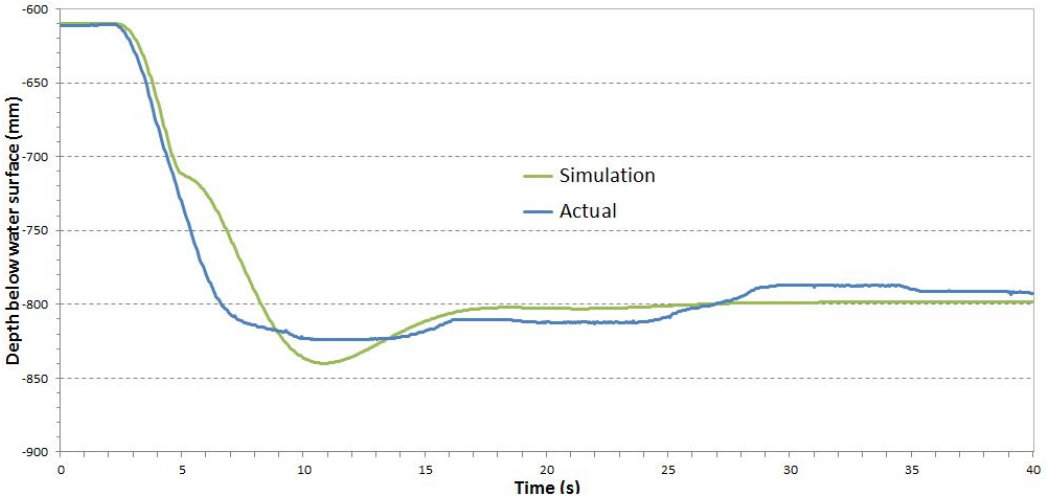

Figure 4.24: Vertical motion due to canard action -30° - simulation vs. actual

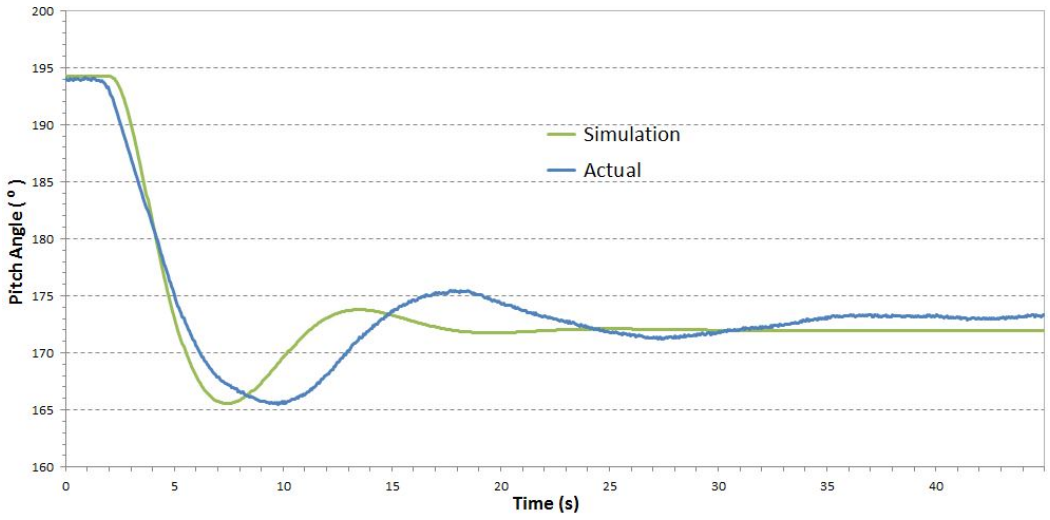

Figure 4.25: Pitch angle motion due to canard action -30° - simulation vs. actual

angle is already positive (12°), the moment will resist further positive change.

For a negative canard action the correlation is also very good since in the depth response the settling depth, settling time, and overshoot are comparable. The main discrepancy is that the simulation shows slightly more overshoot. For the pitch angle response the settling time and settling angle are very close, though the frequency is slightly different. As previously stated this could be due to either variations in the flow velocity during the experiment, or to changes in the added mass added effect on the moment of inertia, caused by the changed state of the canard.

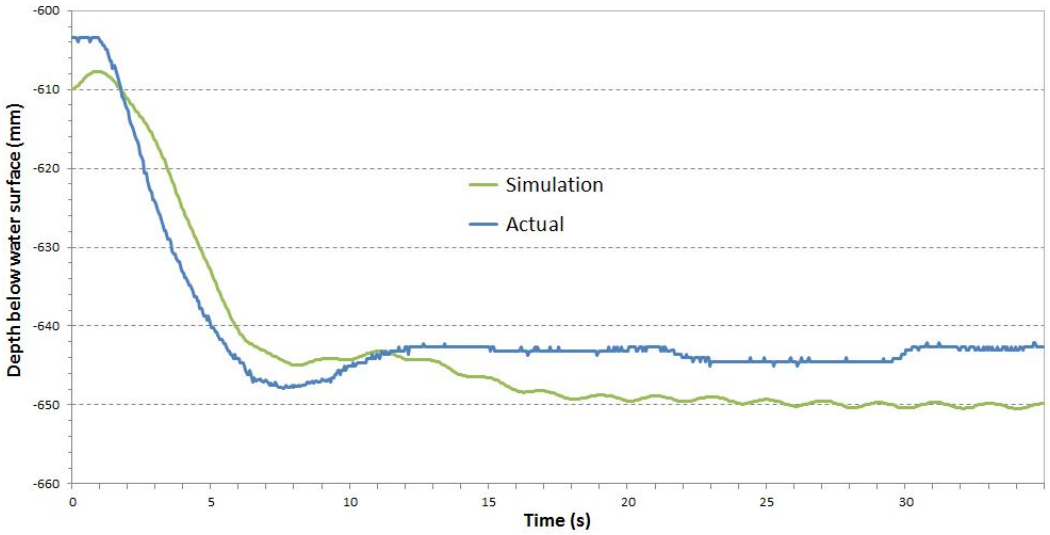

Figure 4.26: Vertical motion due to aileron action - simulation vs. actual

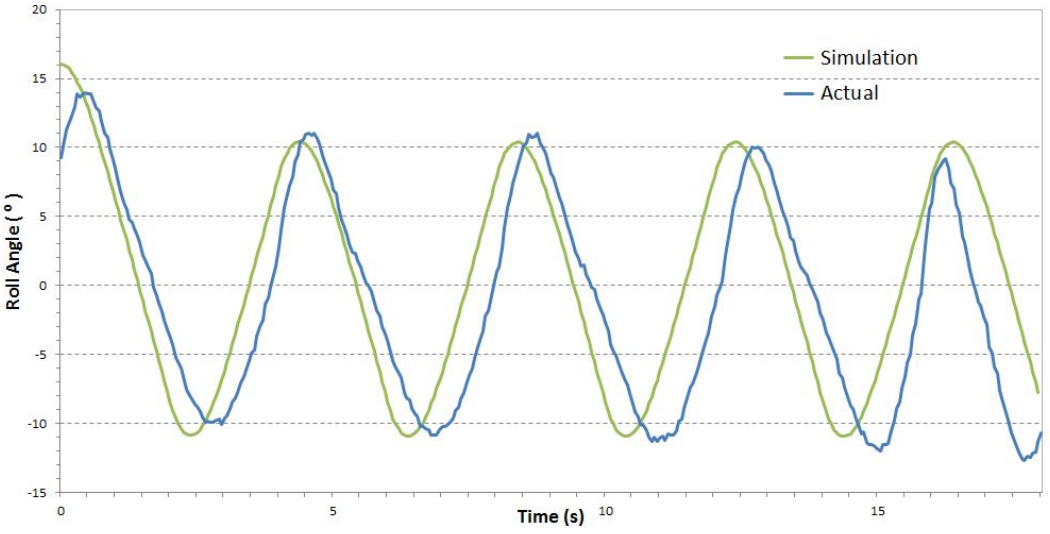

Figure 4.27: Roll angle due to aileron action - simulation vs. actual

4.5.4 Aileron Response

Next the aileron response was simulated, with the ailerons activating alternately, as per Section 4.4.4. Results are shown in Figure 4.26 and Figure 4.27.

For the depth, the correlation is very good. The settling depth, settling time, and overshoot are very comparable. As discussed in Section 4.4.4 above, an interesting point to note was the lack of depth variation due to the rolling motion. As can be seen in the simulation result, a slight oscillation is predicted due to this motion, but in the actual results this is not evident. This could be due to inconsistencies in the flow velocity, or due to insufficient sensitivity of the sensors.

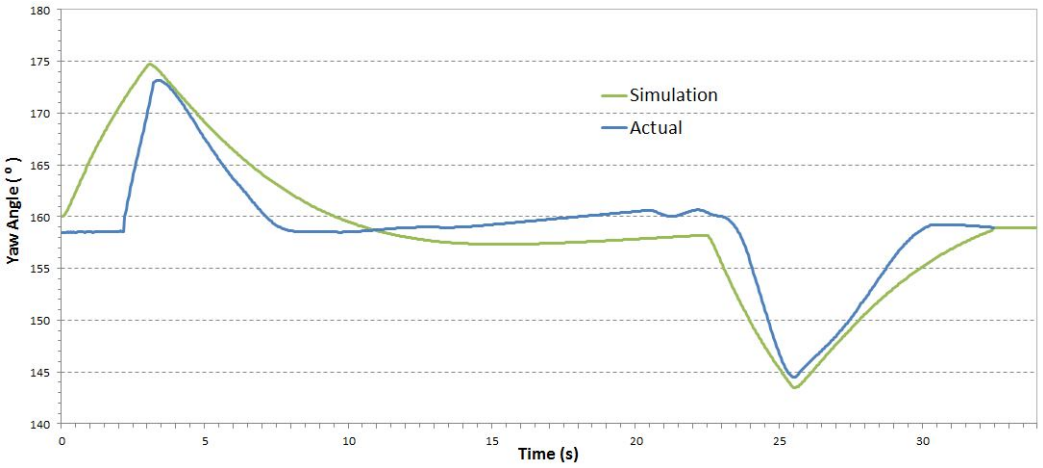

Figure 4.28: Yaw angle motion due to disturbance - simulation vs. actual

For the roll angle, the results are once again quite encouraging. For the first five oscillations the results are very much in line. From then the motion shifts a bit out of phase, and this is probably due, once again, to variations in the flow velocity. The amplitude of the oscillations is also very comparable.

4.5.5 Yaw Angle Response

Finally, the yaw angle disturbance response was simulated, with the results shown in Figure 4.28.

The simulated response is consistent with the actual test data. The simulated response is a bit more idealised than the actual, but that is to be expected.

4.6 Model Tuning

When comparing the purely theoretical model with the test data some discrepancies were found, and the model was adjusted to fit the actual data. The major discrepancies are discussed in this section with analysis of possible reasons for the discrepancy.

4.6.1 Wing Force

The theoretical model predicts a larger force on the vessel due to the wings, than was seen in the actual data. The difference between the calculated behaviour and the actual behaviour is show in Figure 4.29. According to the theory, the peak overshoot brings the vessel much shallower, and the settling depth is also shallower. By reducing the impact of the wing force by 32% the faithful response in Section 4.4.1 is achieved. There are two possible reasons for this discrepancy. Firstly, the wake from the nacelles could be disrupting

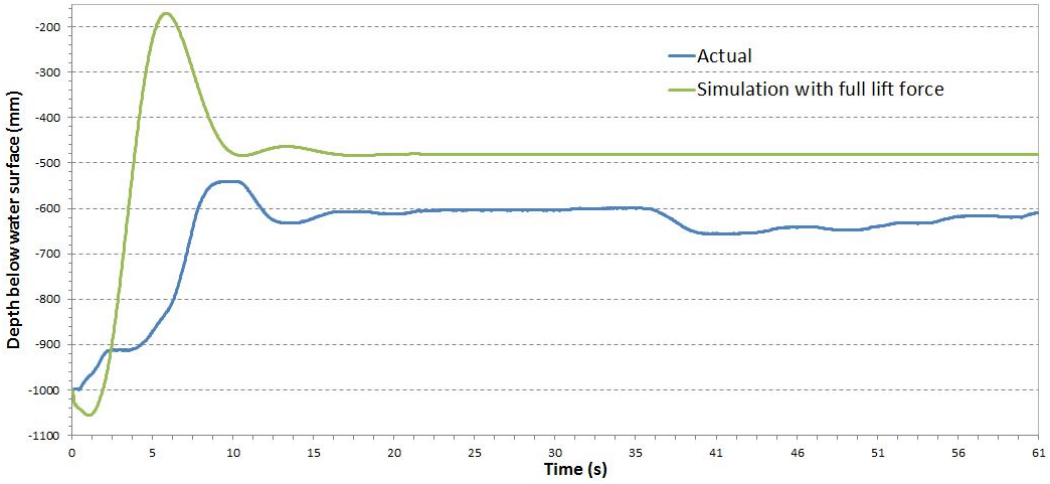

Figure 4.29: Depth simulation vs. actual for theoretical wing force

the flow of water over the wings, resulting in a reduced wing force. Secondly, in the resting pitch orientation, the vessel is at a negative angle of attack. Typically only a positive pitch angle range is asessed for an aerofoil profile, so it may also be that the coefficients at negative angles of attack are not as well studied or understood as the coefficients for positive angles of attack.

4.6.2 Added Mass

Discrepancies were also found in the inertia in the Z_b direction and the moment of inertia about the pitch axis. The difference between the theoretical behaviour and actual behaviour is shown in Figure 4.28. Using the theoretical

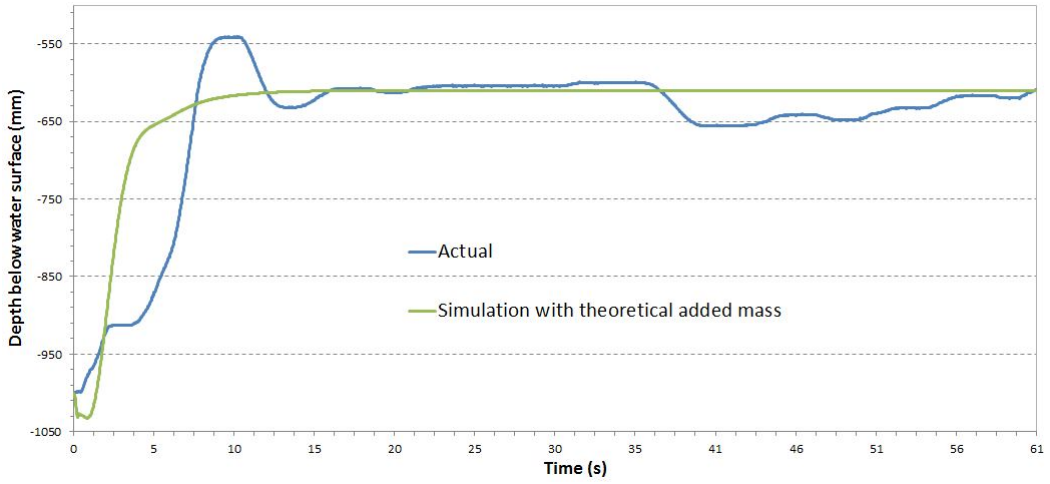

Figure 4.30: Depth simulation vs. actual for theoretical added mass

values the response is far more damped than the actual and reaches the set-

tling point much quicker, though the same setpoint is reached. It was found that by decreasing the Z_b inertia by 42% and increasing the moment of inertia about the pitch axis by 29% the faithful response of Section 4.4.1 is achieved. It is clear that the simplified calculations from Section 3.3 are not accurate for a complex shape such as the OCEC vessel. Calculating accurate values would be very computationally intensive, so obtaining the value by trial and error was more efficient. Actual values for the simulation versus actual results are shown in Appendix B.5.

4.7 Conclusion

A prototype based on the SRET design was constructed, and tests were run to record its dynamic behaviour. Specific tests were done of the depth, pitch angle, roll angle, yaw angle, canard, and aileron responses, with the results being recorded.

Then a mathematical simulation was programmed, based on the theory in Chapter 3, and implemented in Matlab to accurately describe the behaviour of the prototype. Simulations were run and the results were compared against the actual data from the prototype tests. Some discrepancies between theoretical and actual values were found and the model was tuned to more accurately match the actual data.

Once this was completed it was found that there was strong correlation between the simulation results and the actual test results, and therefore the mathematical simulation can be used to accurately predict the behaviour of the vessel in other scenarios, and can be used for the design and testing of control algorithms.

Chapter 5

Control System Design

Now that the behaviour of the vessel has been accurately modelled and verified by experiment, the next stage of the project is to design a control system that will allow for commands to be given to the vessel to accurately and smoothly move into a new position and orientation. There are a number of reasons why this is a requirement:

- Tracking of the optimal current flow. Earlier info has shown that the position of the maximum flow of the Agulhas Current moves, and the vessel should be capable of adjusting its position to follow the current's "sweet spot".
- The vessel should also be capable of basic hazard avoidance, such as if there is an extreme weather event at the surface, it should dive lower to avoid damage.
- It should be capable of rising to the surface and diving back down again for maintenance purposes. The vessel should also be able to avoid damage in the case of the failure of a critical component, such as a turbine blade or a gearbox.
- A safe depth below the surface should also be stictly maintained to avoid interference with shipping lanes.

5.1 Trim Condition

In this study, linear control theory will be used to analyse the stability of the vessel and to design a controller which gives desired behaviour for various motions. The motions that will be targeted for control will be the depth and the roll angle. Drag has been shown to be a significant factor in the dynamics of the vessel. Drag is by its nature non-linear, as it has a squared relationship with flow velocity, so to perform a linear analysis a linear approximation of the vessel's dynamics will have to be done. Standard practice for aircraft control design is to linearise the behaviour of the vessel around its equilibrium

point, often called the "Trim condition". For this study the equilibrium point which was the natural resting point and orientation of the vessel that was obtained from the prototype tests will be used as the Trim point about which to linearise. This point is with the vessel at a depth of 610 mm and an angle of 14.2°.

This position is clearly highly dependent on the specific characteristics of the vessel, and could be adjusted if necessary. However, when analysing the depth versus angle graph from Chapter 4, it can be seen for the test flow velocity of 0.62 ms^{-1} that 14.2° is actually an optimal position to use since the relationship between depth and angle is fairly linear at that point, and the vessel can go through a wide range of depths (0 m to -1 m), without moving into the non-linear space.

Since, due to the angle of the tether, the dynamics would be slightly different at different depths, the characteristics will be investigated at three depth points.

For the purpose of this analysis, the state space notation will be used to allow a multi-variate analysis. The typical state space equation is of the form:

$$\dot{\mathbf{x}} = f(\mathbf{x}, \mathbf{u}) \tag{5.1.1}$$

Where $\mathbf{x}$ is the states of the vessel, and $\mathbf{u}$ is the state of the input variables such that:

$$\mathbf{x} = (\eta, \nu) \tag{5.1.2}$$

$$\mathbf{u} = (\delta_C, \delta_A) \tag{5.1.3}$$

The Trim condition is the point at which the resultant force on the vessel is zero in all directions as well as the moment about all axes and the velocity is zero in all directions. With the vessel in equilibrium at Trim, this would mean that:

$$\dot{\mathbf{x}}_T = f(\mathbf{x}_T, \mathbf{u}_T) = 0 \tag{5.1.4}$$

Where $\mathbf{x}_T$ are the vessel states at Trim and $\mathbf{u}_T$ are the input variables at Trim.

To linearise the non-linear dynamics of the vessel, a linear approximation will be done about the Trim condition by considering that deviations from the Trim state are small, and that the above condition is true. This means Equation 5.1.1 can be re-written to:

$$\dot{\mathbf{x}}_T + \Delta\dot{\mathbf{x}} = f(\mathbf{x}_T + \Delta\mathbf{x}, \mathbf{u}_T + \Delta\mathbf{u}) \tag{5.1.5}$$

Considering Equation 5.1.4 and disregarding higher order terms, this can be simplified to:

$$\Delta\dot{\mathbf{x}} \approx A_T\Delta\mathbf{x} + B_T\Delta\mathbf{u} \tag{5.1.6}$$

Where:

$$A_T = \left.\frac{\partial f}{\partial x}\right|_T$$
$$B_T = \left.\frac{\partial f}{\partial u}\right|_T \tag{5.1.7}$$

It would further simplify the analysis to separate the longitudinal and lateral states such that:

$$\begin{aligned}\Delta\mathbf{x}_{long} &= [\Delta u \quad \Delta w \quad \Delta q \quad \Delta x \quad \Delta z \quad \Delta\theta]^T \\ \Delta\mathbf{x}_{lat} &= [\Delta v \quad \Delta p \quad \Delta r \quad \Delta y \quad \Delta\phi \quad \Delta\psi]^T \\ \Delta\mathbf{u}_{long} &= \Delta\delta_C \\ \Delta\mathbf{u}_{lat} &= \Delta\delta_A\end{aligned} \tag{5.1.8}$$

Then Equation 5.1.6 becomes:

$$\begin{bmatrix} \Delta\dot{\mathbf{x}}_{Long} \\ \Delta\dot{\mathbf{x}}_{Lat} \end{bmatrix} = \begin{bmatrix} A_{T11} & A_{T12} \\ A_{T21} & A_{T22} \end{bmatrix} \begin{bmatrix} \Delta\mathbf{x}_{Long} \\ \Delta\mathbf{x}_{Lat} \end{bmatrix} + \begin{bmatrix} B_{T11} & B_{T12} \\ B_{T21} & B_{T22} \end{bmatrix} \begin{bmatrix} \Delta\mathbf{u}_{Long} \\ \Delta\mathbf{u}_{Lat} \end{bmatrix} \tag{5.1.9}$$

Since the vessel is symmetrical about the X-Z plane:

$$\begin{aligned}A_{T21} &= 0 \\ B_{T21} &= 0\end{aligned} \tag{5.1.10}$$

And since deviations (particularly roll angle) are small:

$$\begin{aligned}A_{T12} &\approx 0 \\ B_{T12} &\approx 0\end{aligned} \tag{5.1.11}$$

And thus the longitudinal and lateral equations can be decoupled and written as:

$$\begin{aligned}\Delta\dot{\mathbf{x}}_{Long} &= A_{T11}\Delta\mathbf{x}_{Long} + B_{T11}\Delta\mathbf{u}_{Long} \\ \Delta\dot{\mathbf{x}}_{Lat} &= A_{T22}\Delta\mathbf{x}_{Lat} + B_{T22}\Delta\mathbf{u}_{Lat}\end{aligned} \tag{5.1.12}$$

This allows for separate analysis of the longitudinal and lateral dynamics, and separate control strategies can be implemented for these two sets of dynamics.

5.2 Analysis of Linearised Dynamics

In this analysis, for both the longitudinal and lateral motions, the state space equations to be used will be of the following form:

$$\begin{aligned}\dot{x} &= Ax + Bu \\ y &= Cx\end{aligned} \tag{5.2.1}$$

By performing a Laplace transform on the above equations it can be shown that the open loop poles of the system satisfy:

$$det(sI - A) = 0 \tag{5.2.2}$$

It can be noted that this is also the equation to calculate the eigenvalues of a matrix, therefore determining the eigenvalues will produce the open loop poles of the system and allow for linear analysis.

5.2.1 Longitudinal Motion

Writing the longitudinal states in the form of Equation 5.2.1 and dropping the Δ notation for simplicity gives:

$$\begin{bmatrix} \dot{u} \\ \dot{w} \\ \dot{q} \\ \dot{x} \\ \dot{z} \\ \dot{\theta} \end{bmatrix} = \begin{bmatrix} \frac{\partial \dot{u}}{\partial u} & \frac{\partial \dot{w}}{\partial u} & 0 & \frac{\partial \dot{u}}{\partial x} & \frac{\partial \dot{u}}{\partial z} & \frac{\partial \dot{u}}{\partial \theta} \\ 0 & \frac{\partial \dot{w}}{\partial w} & 0 & \frac{\partial \dot{w}}{\partial x} & \frac{\partial \dot{w}}{\partial z} & \frac{\partial \dot{w}}{\partial \theta} \\ 0 & 0 & \frac{\partial \dot{q}}{\partial q} & \frac{\partial \dot{q}}{\partial x} & \frac{\partial \dot{q}}{\partial z} & \frac{\partial \dot{q}}{\partial \theta} \\ \cos\Theta_T & -\sin\Theta_T & 0 & 0 & 0 & 0 \\ -\sin\Theta_T & \cos\Theta_T & 0 & 0 & 0 & 0 \\ 0 & 0 & 1 & 0 & 0 & 0 \end{bmatrix} \begin{bmatrix} u \\ w \\ q \\ x \\ z \\ \theta \end{bmatrix} + \begin{bmatrix} 0 \\ 0 \\ \frac{\partial \dot{q}}{\partial \delta_C} \\ 0 \\ 0 \\ 0 \end{bmatrix} \delta_C \tag{5.2.3}$$

For details of the calculation of the values for this matrix see Appendix C.1. Using the eigenvalues of the above matrix to determine the roots produces the root locus diagram in Figure 5.1.

There are three sets of complex pole pairs at -0.15 $\pm$ 0.5j, -0.381 $\pm$ 0.384j, and -99.99 $\pm$ 23.9j. The first pole pair represents the pitch angle motion, which is slow and under-damped, as shown in graphs of Section 4.4.3. The second pole pair represents the motion in the Z_b direction, which is slow and close to critically damped, as was seen in the response graphs of Section 4.4.1. The third pole pair represents motion in the X_b direction, which is very fast and damped. This represents the elastic response of the tether. These roots can be ignored in the control design since this response is stable and orders of magnitude faster than the other dynamics . For the pitch angle dynamics some damping is required to reduce the overshoot. The Z_b dynamics are well damped, so all that is necessary from a control standpoint is to try to optimise the speed of the response and ensure no error when tracking the system setpoint.

5.2.2 Lateral Motion

Since motion in the Y_b direction is relatively slow, the y position has little impact on the dynamics and there are no control surfaces to affect this motion so it will be excluded from the analysis. Thus the linearised lateral dynamics

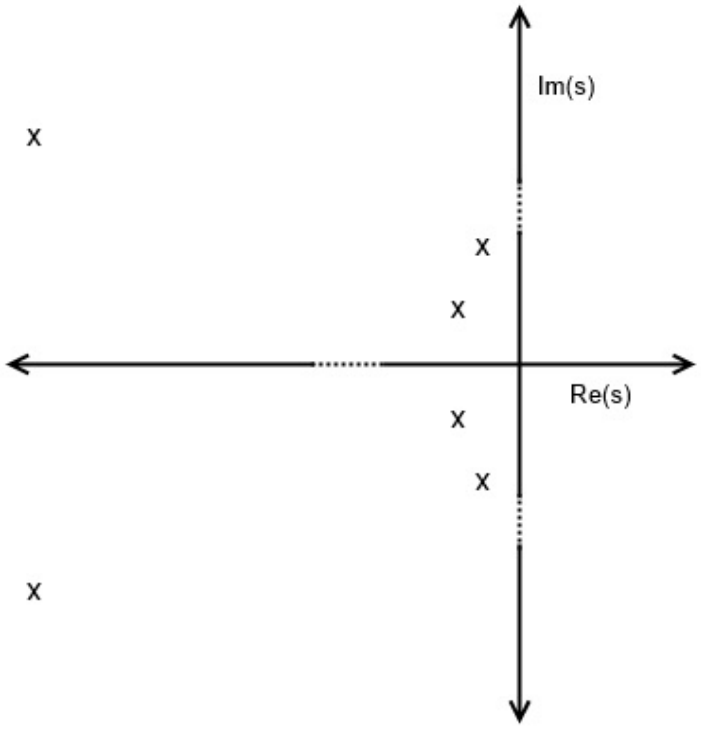

Figure 5.1: Longitudinal Poles - not to scale

can be reduced to:

$$\begin{bmatrix} \dot{p} \\ \dot{r} \\ \dot{\phi} \\ \dot{\psi} \end{bmatrix} = \begin{bmatrix} \frac{\partial \dot{q}}{\partial \psi} & 0 & 0 & \frac{\partial L}{\partial \psi} \\ 0 & \frac{\partial \dot{r}}{\partial r} & \frac{\partial \dot{r}}{\partial \phi} & \frac{\partial \dot{r}}{\partial \psi} \\ 1 & \tan\Theta & 0 & 0 \\ 0 & \sec\Theta & 0 & 0 \end{bmatrix} \begin{bmatrix} p \\ r \\ \phi \\ \psi \end{bmatrix} + \begin{bmatrix} \frac{\partial \dot{p}}{\partial \delta_C} \\ 0 \\ 0 \\ 0 \end{bmatrix} \delta_A \tag{5.2.4}$$

Using the eigenvalues above to determine the open loop roots produces the root locus diagram in Figure 5.2.

There are four poles at 0.0285, -0.798, $-0.389 \pm 0.116j$. The first two poles represent the motion about the roll axis which is slow and unstable. When disturbed in roll the vessel will continue to roll at a constant rate, as seen in the graphs of Section 4.4.4. The complex pole pair represents the yaw motion, which is slow and overdamped, returning to neutral without any overshoot, as shown in Section 4.4.5. This analysis suggests that simply inserting a feedback loop on the roll states into the above system will allow for faithful tracking of the setpoint roll angle. Actual values used in the matrices can be found in Appendices C.2 and C.3.

5.3 Detailed Control System Design

Since motions in both directions are already well damped in open loop, a simple state feedback loop will be used for control in both longitudinal and

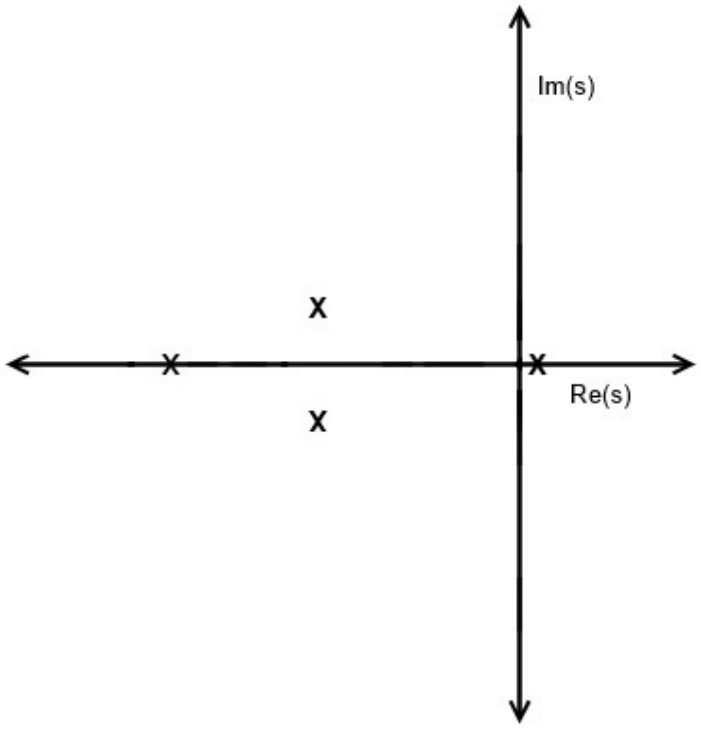

Figure 5.2: Lateral Poles - not to scale

lateral motions. Only the states available from the sensor will be used for feedback, to avoid the errors that could arise from estimating states. For both motions the control design will be of the following form shown in Figure 5.3.

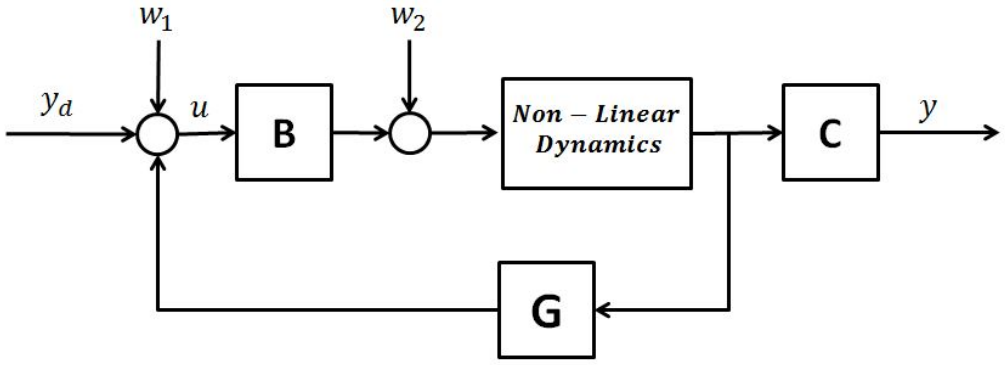

Figure 5.3: Control system form

Where A, B, C are as per Equation 5.2.1, G is the feedback coefficients, y_d are the desired outputs, w_1 and w_2 are disturbances, and y is the actual output. The states available from the gyro sensor are the Euler Angles (ϕ, θ, ψ) and the angular rates (p, q, r). From the linear sensor the depth z is available, thus these are the states that will be used for feedback.

From Section 4.4.6 it was noted that the full range of canard motion only allows a limited range of depth motion, so for this theoretical study the canard will be allowed to deviate further than it's physical operating range to allow a greater depth range.

5.3.1 Depth Control

As can be seen from the linear analysis and the response graphs of Section 4.4.1, the depth response is already well damped, thus minimal intervention is required to achieve the ideal results. Depth change rate damping is required to reduce the overshoot and integral control will also be implemented to ensure precise tracking of the setpoint. As was shown in Section 4.5.1 there is a nearly linear correlation between the depth and the pitch angle, therefore feedback of the pitch angle and pitching rate will be used in the depth control. The objective of this study is to achieve stable depth control with the simplest possible control strategy, thus proving the stability and controllability of the system.

The coefficients for the states θ and q will be selected to provide a more damped angle command response, and then the depth error coefficient will be tuned to produce a damped response. An integrator term will also be added on the depth error to ensure faithful tracking of the depth setpoint. Thus, the control strategy will be of the form shown in Figure 5.4.

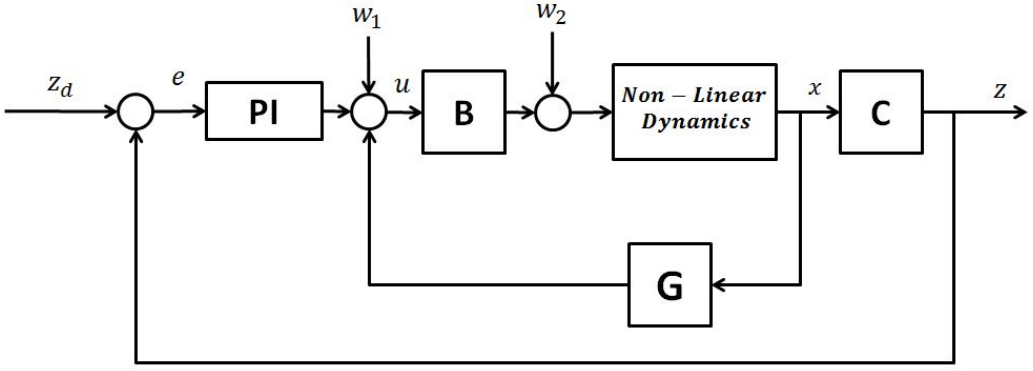

Figure 5.4: Longitudinal motion controller

Tuning those variables to the values $G_1 = 1.6$, $G_2 = 0.1$, $P = 4$, and $I = 2.3$ gives the step response in Figure 5.5. The depth settles to within 10% of the setpoint within 20.5 s and 1% within 27.3 s, with an overshoot of 1.3%. This is a close to ideal response and compares well with the open loop response from Section 4.4.1. The settling time is almost the same, but with far less overshoot and with less than 1% error from setpoint.

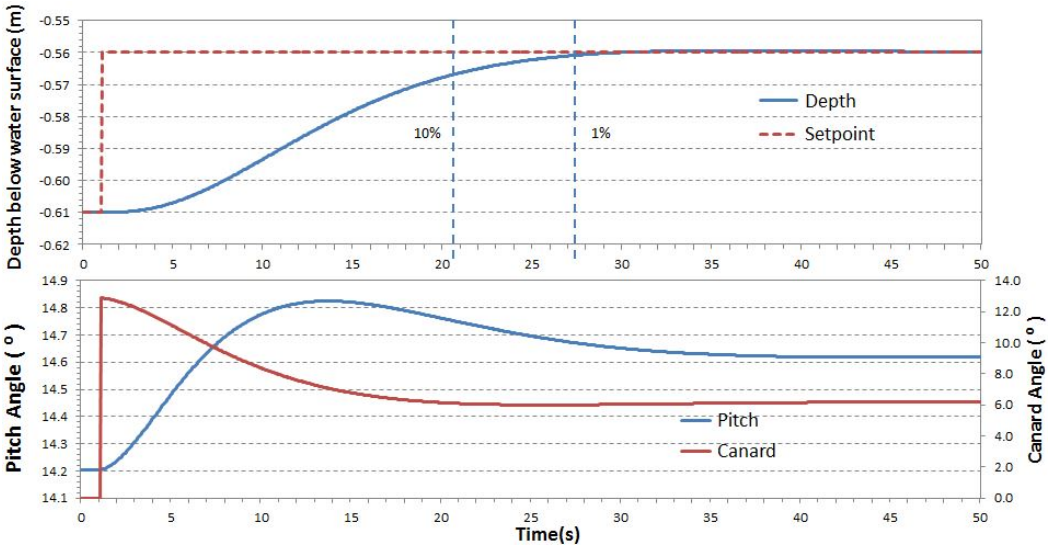

Figure 5.5: Depth control (simulation)

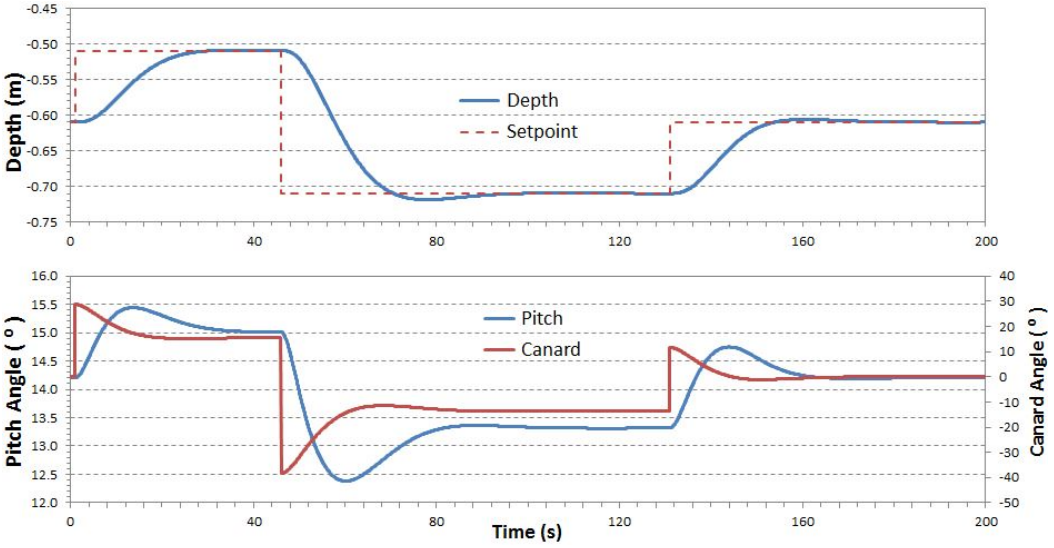

Figure 5.6: Depth control following varying setpoint 1 (simulation)

With a linear model it could be expected to achieve a faster response than the open loop, however, with the response being non-linear it does not follow the same pattern, and any attempt to increase the speed resulted in an overshoot. It can also be noted that the pitch angle has overshoot, which enables a faster depth response, and the canard action is well within normal working range.

Further simulations to different setpoints were done and the results are shown in Figures 5.6 and 5.7.

It can be seen that the response tracks the setpoint well with all setpoints, though the response dynamics do vary, depending on the depth.

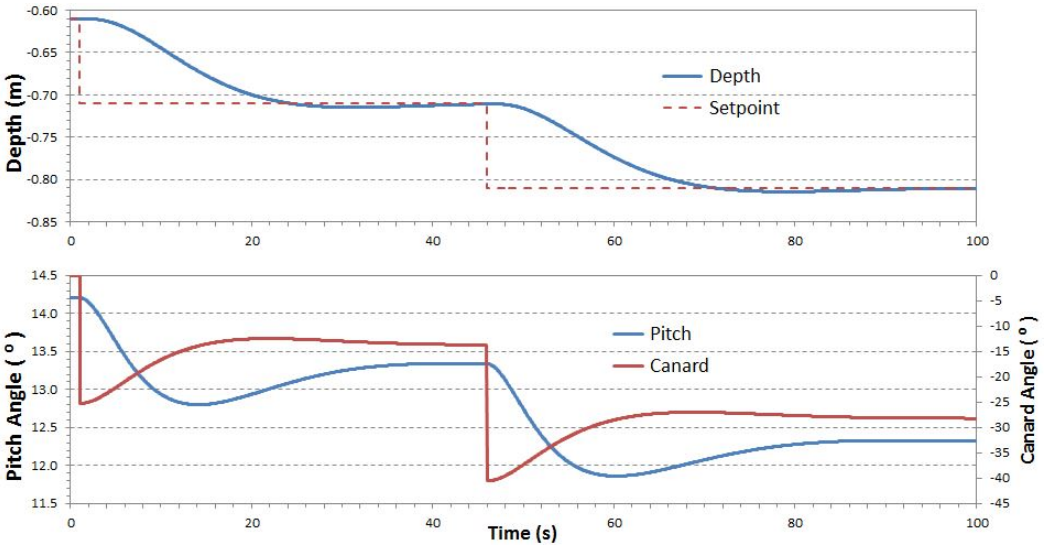

Figure 5.7: Depth control following varying setpoint 2 (simulation)

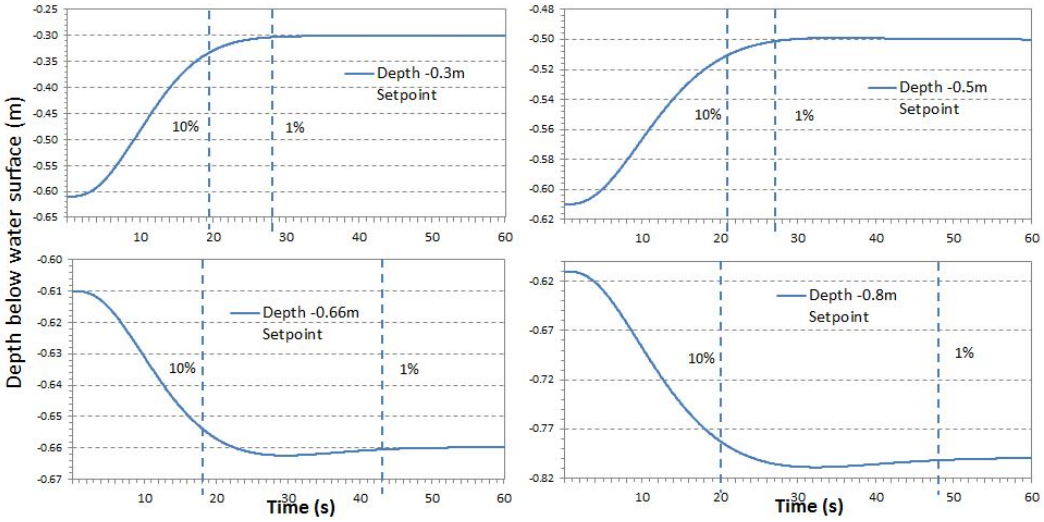

Figure 5.8: Depth control to various setpoints (simulation)

It was noted in Section 5.1 that some variance could be expected in the response at different depths due to changes in the pitch angle and tether angle. The response was tested to various depths with some examples shown in Figure 5.8.

While the dynamic response does vary depending on the depth of the command setpoint, all the responses are favourable and improved from the open loop. Table 5.1 gives the response characteristics for the various depths. Clearly the controller could be adjusted to suit the specific range in which the vessel is expected to operate, but given these values for G, P, and I the vessel is controllable across the full depth range. The key indicators are shown in Table 5.1. The crucial difference is that moving to the deeper

Table 5.1: Dynamic response data for different depths (simulation)

Depth (m)	Overshoot	10% (s)	1% (s)
-0.80	4.4%	19.8	47.7
-0.70	4.8%	21.0	44.0
-0.66	4.8%	18.7	42.9
-0.56	1.3%	20.5	27.3
-0.50	1.0%	20.8	27.1
-0.40	0	20.2	27.1
-0.30	0	19.7	28.2

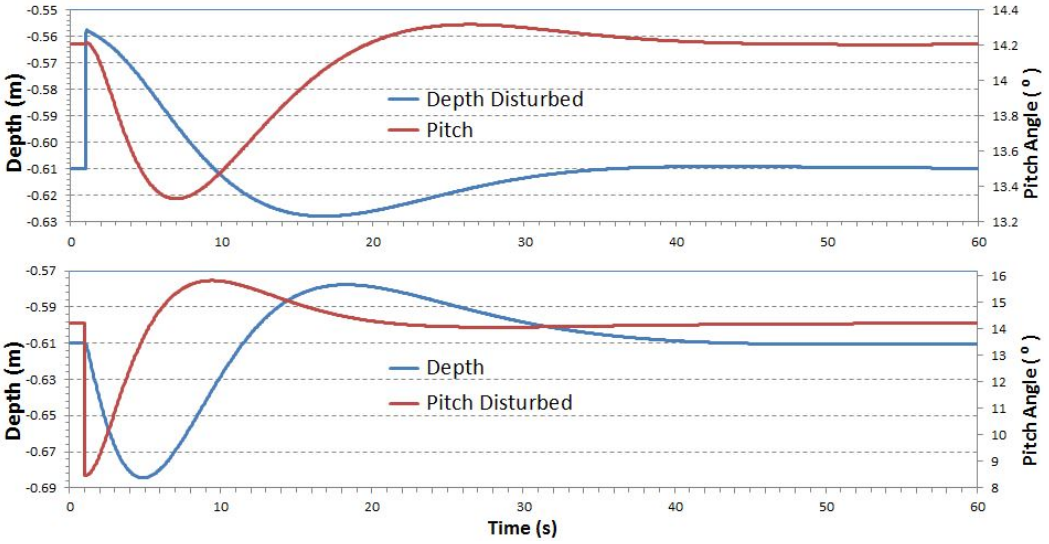

Figure 5.9: Pitch and depth response to pitch and depth disturbance (simulation)

depths (< -0.6 m) the overshoot increases, resulting in a significant increase in settling time to the 1% of setpoint.

To test the robustness of this control strategy, disturbances were introduced into the system, with the responses shown in Figure 5.9. Both pitch angle and depth return to Trim condition within 45 s, therefore it can be determined that the system is robust enough to reject disturbances of the major states.

As was illustrated in Section 3.4 the flow rate of the towing tank was inconsistent, thus the system was tested for the case of a varying flow rate. It is also likely, given the environment, that the sensor feedback would have a significant noise component, so the system is tested for noise on the sensor signals. The responses are shown in Figures 5.10 and 5.11. It can be seen that a variation in the flow rate does have a significant effect on the depth response, and even looks similar to the variation in response obtained in data from Section 3.5.1. However the system is still capable of tracking the setpoint. As can be seen in all the response figures, the control method is

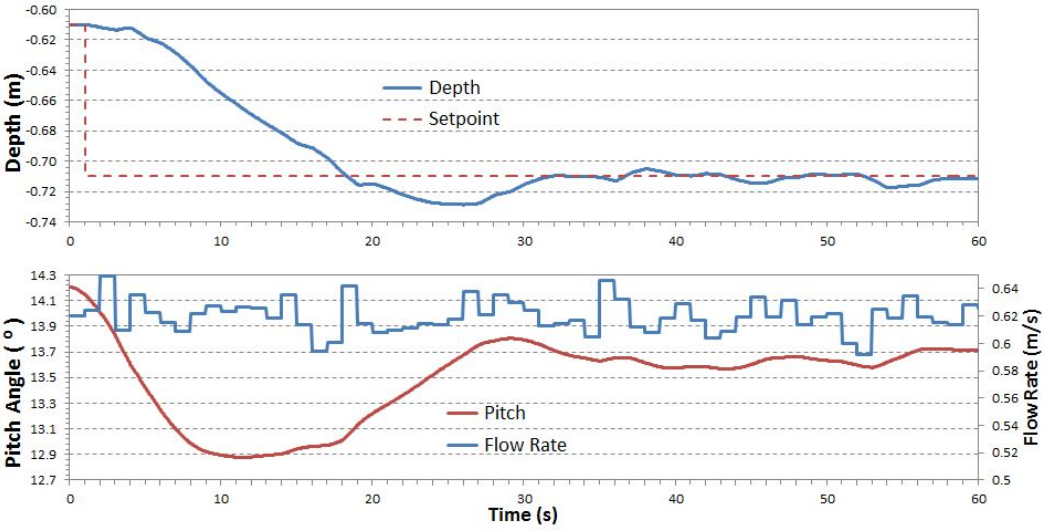

Figure 5.10: Depth control response with flow rate disturbance (simulation)

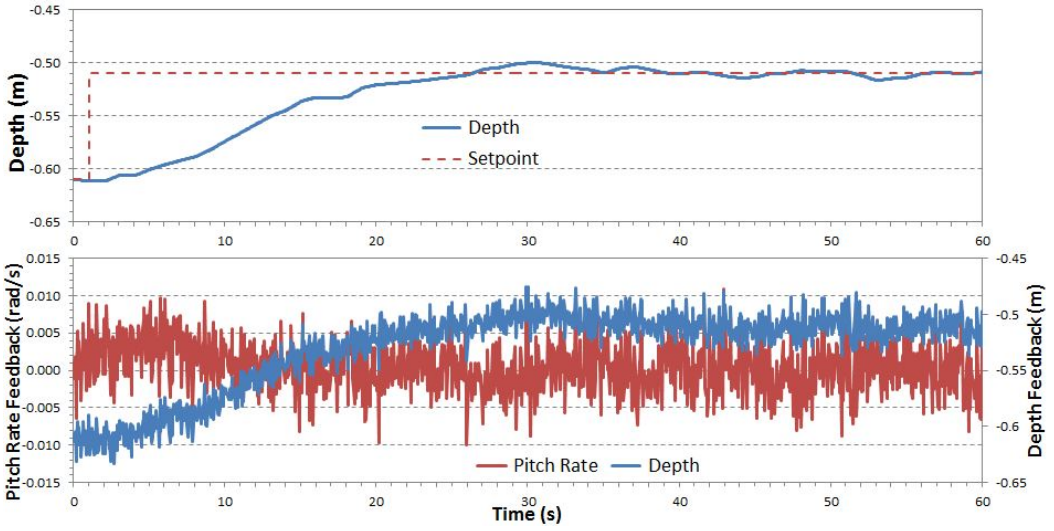

Figure 5.11: Depth control response with flow rate disturbance and feedback noise (simulation)

robust and well able to resist noise and disturbances on all parameters. Having been simulated with disturbances the control strategy was then simulated at different depths to confirm consistent response over the entire depth range.

The data in this section has shown that the response is consistent despite changes in depth. This control stratgey is thus suitable for use on this model in all conditions.

5.3.2 Lateral Motion Control

The coefficients for the states ϕ and p will be selected to provide an ideal angle command response, using the following control form. Both these states are available from the onboard gyro so this is a practical implementation of a control strategy. It shoud be noted that, for this vessel, it is unlikely that it would ever be required to do a controlled roll motion, as this control strategy is designed to resist changes in yaw and roll angle and return the vessel to its Trim state. The control strategy will be of the form of Figure 5.3. After selecting the angle coefficients of $G_1 = 1$ and $G_2 = 3$, the angle step response shown in Figure 5.12 was achieved on the non-linear model. This control

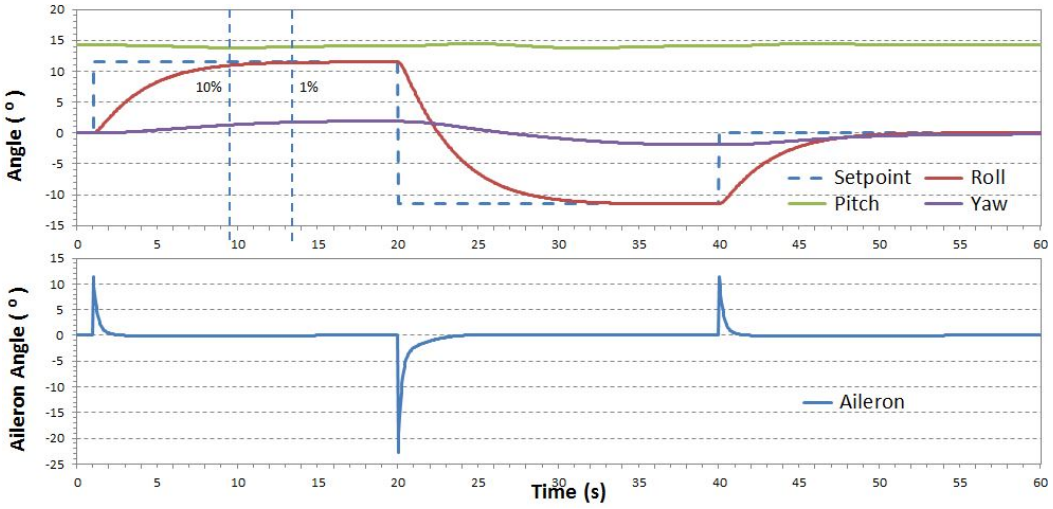

Figure 5.12: Roll angle control (simulation)

algorithm produces a critically damped response, moving to within 10% of the setpoint value in 9.4 s, and 1% of the setpoint value in 13.3 s, and having no overshoot. The aileron action stays within the useable range of motion for the flaps. As predicted, the pitch angle is only slightly affected and the yaw angle is disturbed by 2°, but returned to zero when the roll angle returns to zero. Disturbances were introduced into the system to test the robustness of this control strategy, with the responses shown in Figures 5.13, 5.14, and 5.15.

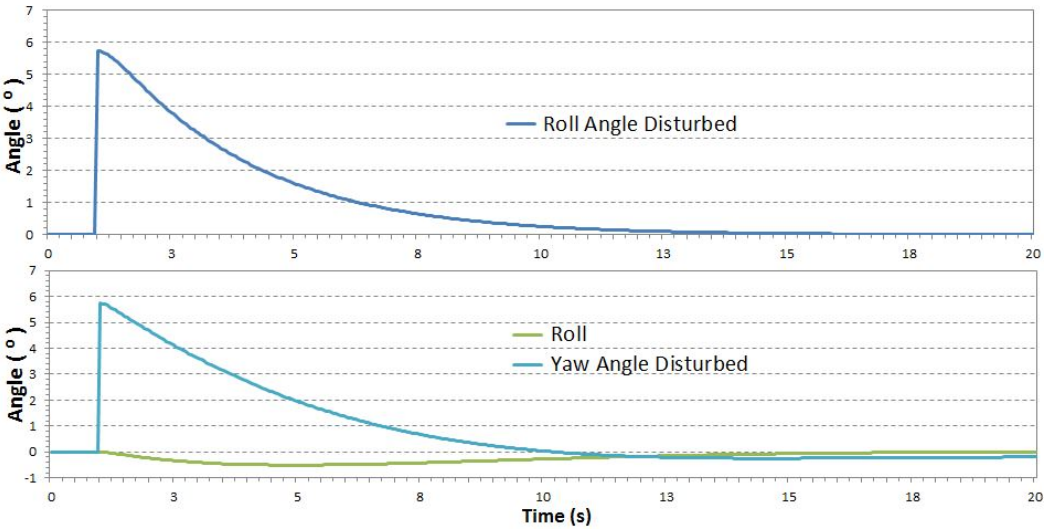

Figure 5.13: Roll angle control response to roll and yaw angle disturbances (simulation)

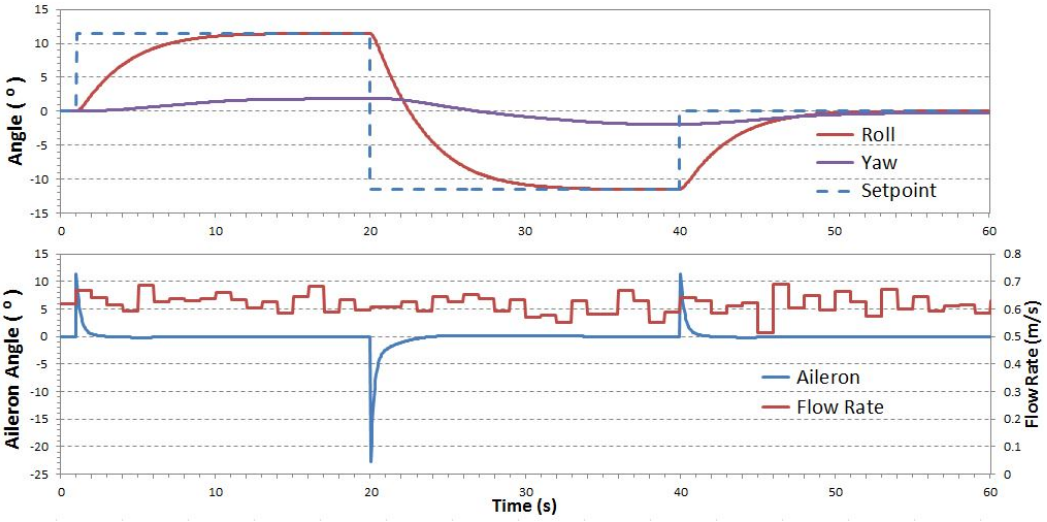

Figure 5.14: Roll angle control response with flow rate disturbance (simulation)

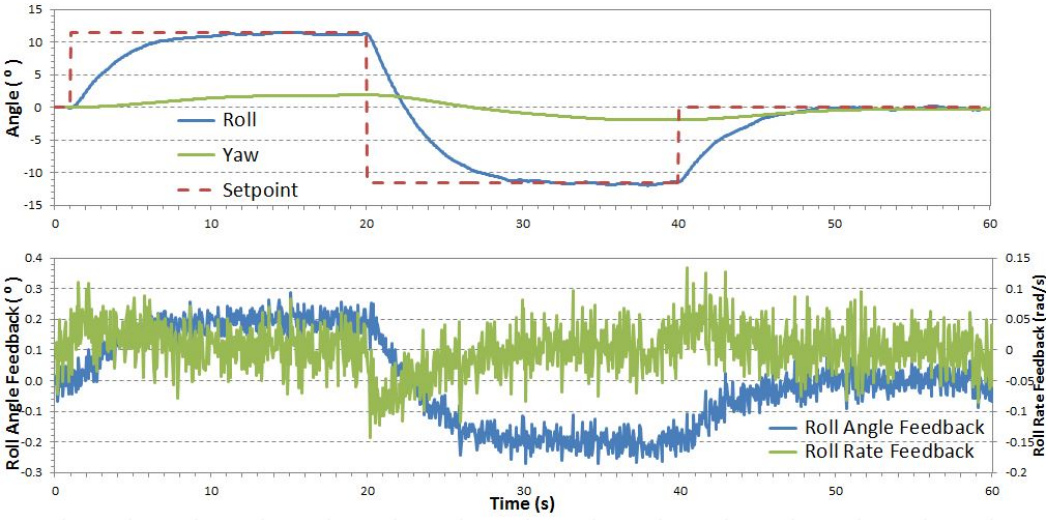

Figure 5.15: Roll angle control response with flow rate disturbance and feedback noise (simulation)

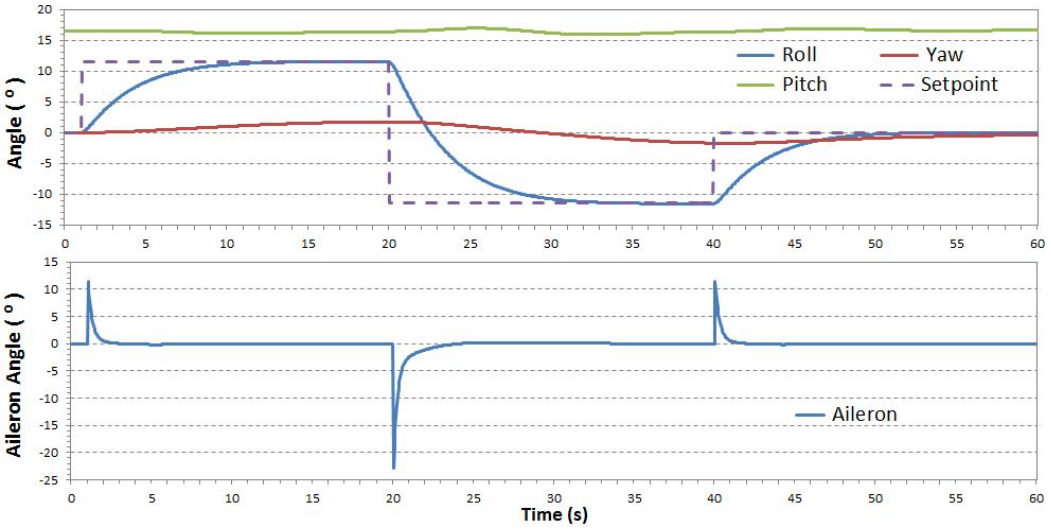

Figure 5.16: Roll angle control response at depth of -300 mm (simulation)

As can be seen in all these figures the control method is well able to resist noise and disturbances on all parameters. The control strategy was then simulated at different depths to confirm consistent responses over the entire depth range. The results are shown in Figures 5.16 and 5.17.

It has been shown in those Figures that the response is consistent despite changes in depth. This control stratgey is thus suitable for use on this model in all conditions.

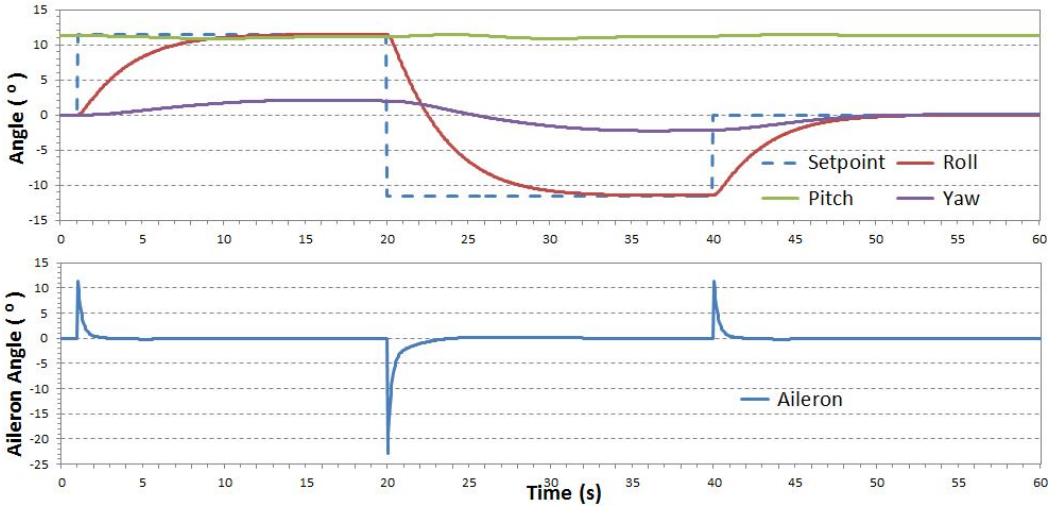

Figure 5.17: Roll angle control response at depth of -900 mm (simulation)

5.3.3 Combined Motion Control

While the linear model works on the assumption of total independence between longitudinal and lateral motions, in reality there must be some correlation in the non-linear model. First, a test was done of the impact on the height when the roll changes. Results are shown in Figure 5.18.

These results show that when the vessel rolls there is a disturbance of about

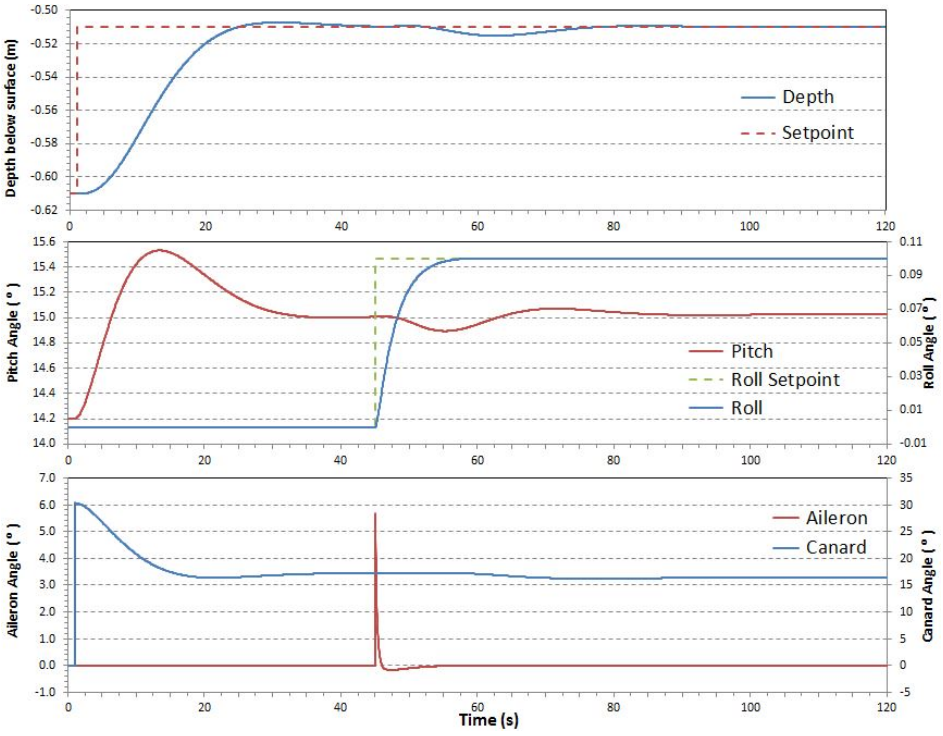

Figure 5.18: Combined response graphs - roll angle change (simulation)

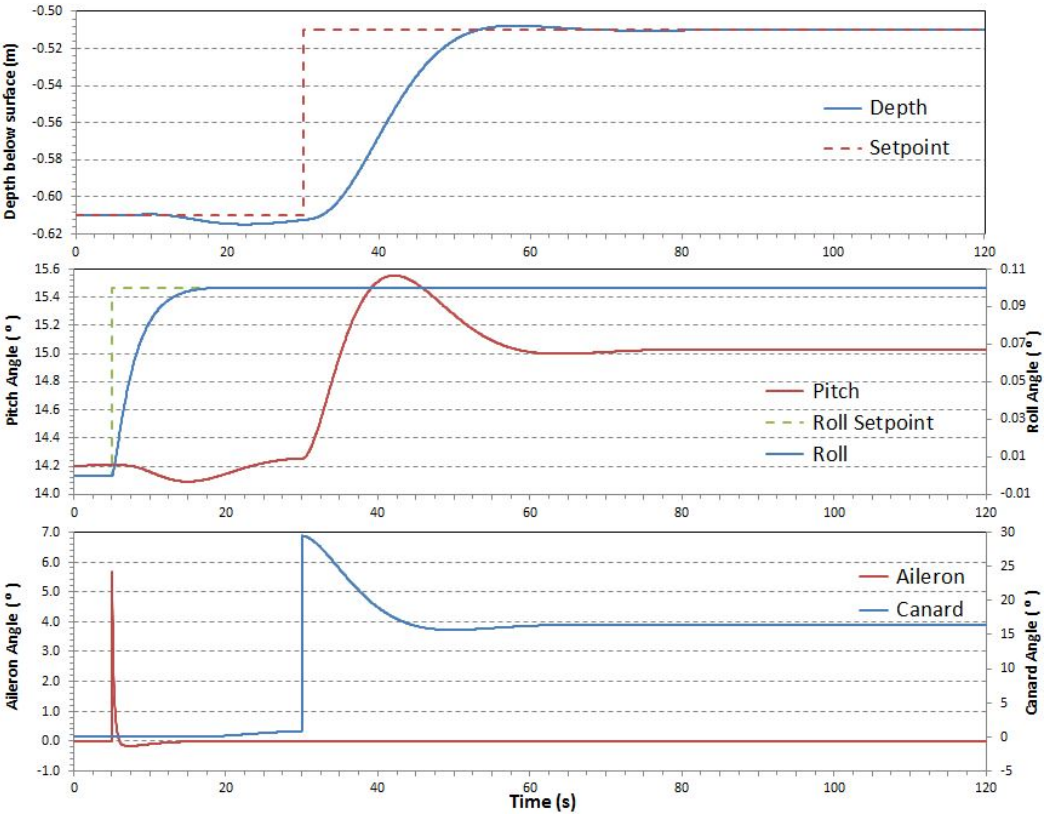

Figure 5.19: Combined response graphs - depth change (simulation)

10 mm of the height and pitch angle, however, the height then returns to setpoint, despite the changed roll angle. Next, the impact on the roll was tested when the height is changed. Results are shown in Figure 5.19. The roll angle is not affected at all by a change in the height. Finally, a complex combination of motions of the height and roll angle were simulated and the results are shown in Figure 5.20. Despite the extreme motions in both longitudinal and lateral motions, both the height and roll angle are able to track their setpoints, with only some disturbance shown in the height.

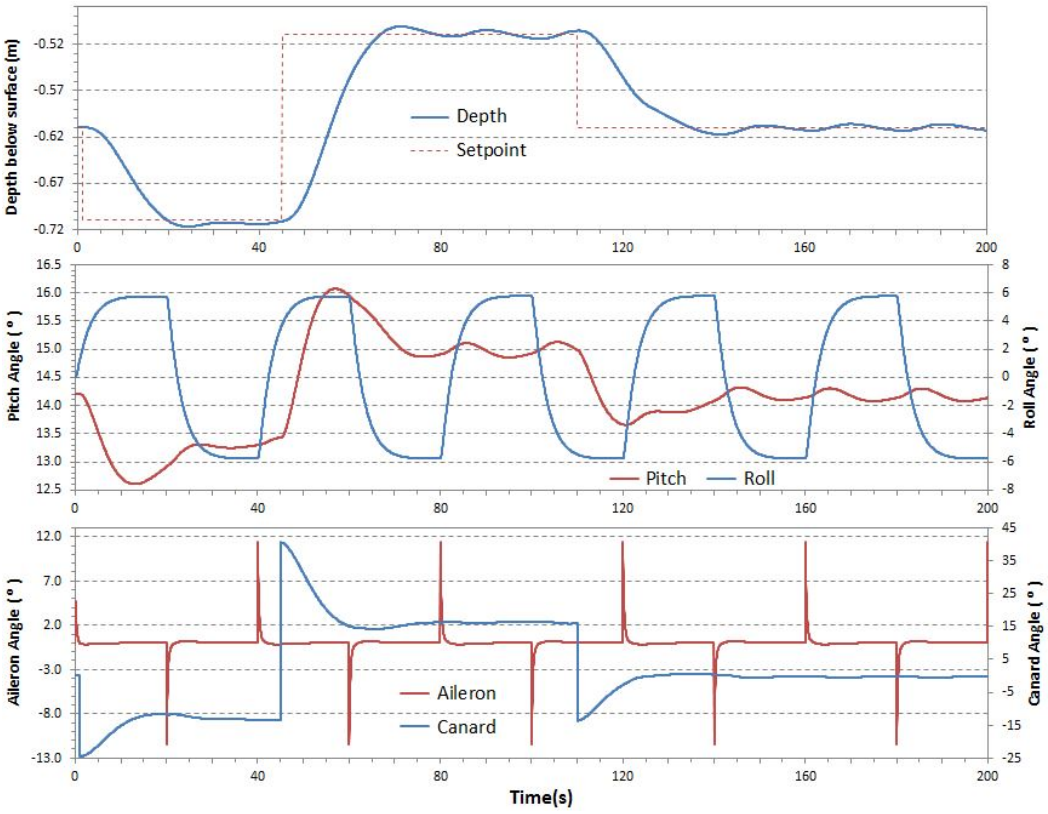

Figure 5.20: Combined response graphs - depth and roll angle change (simulation)

5.4 Conclusions

Throughout this section, the controlabillity of this model was theoretically analysed and tested in simulation. It was shown that by using a simple controller the system can be robustly controlled for depth and roll angle, and even in extreme circumstances, the control method is successful in controlling the vessel.

Chapter 6

Conclusions and Recommendations

6.1 Conclusions

This study set out to test the feasibility of the OCEC design by confirming that the design is both dynamically stable and controllable when acted upon by hydrodynamic forces. A simulation model was written in Matlab to predict the dynamic behaviour of the OCEC. A prototype OCEC was built to verify the simulation model. This prototype was tested under various conditions in the Towing Tank Facility at Stellenbosch University. The data obtained confirmed that the mathematical model was a faithful representation of the dynamic behaviour of the vessel. The simulation model was analysed to determine the dynamic factors related to control design. A simple PID control strategy was then devised based on the analysis and tested in simulation, using the Matlab simulation model. This simluation showed that both in longitudinal and lateral motions the vessel is stable and controllable, even when the control motions are combined and disturbances are introduced into the system.

6.1.1 Simulation Model

The simulation model used proved to give accurate predictions of the dynamic behaviour, however, there were a few points where there were discrepancies between theory and test data:

- Wing Lift Force - the lift force from the wings proved to be much less in practice than the theory had predicted. A possible reason for this could be that the wake created by both the nacelles and fuselage disrupted the flow over the wings, resulting in reduced lift.
- Added Mass - due to the complex shape of the OCEC, determining the added mass effect by separately calculating the effect of individual body

elements and then adding those together resulted in significant error. More accurate values had to be derived by testing.

- Complex Cable Dynamics - the cable force theory used was quite complex, as obtained from literature, but due to the low weight and short length of the cable, those dynamics were hardly noticeable and could essentially be disregarded. However, this theory has been retained because if the cable were to be longer and heavier, as in the case for the full-scale prototype, then cable dynamics would come much more into play.

6.1.2 Prototype

The building of the prototype and testing was the most challenging part of the project due to numerous practical difficulties encountered. As this model was an original and unproven design this was to be expected. This does call into question the reliability of the test data obtained, though tests were repeated numerous times to verify results. Difficulties encountered included the following:

- Water Ingress - keeping the prototype waterproof was a major challenge, which affected a number of the test runs. This had two major impacts. Firstly, water contaminated the onboard sensors affecting the readings. Secondly, the water ingress was not uniform in the various parts of the prototype, which affected the weight distribution of the prototype, resulting in unbalanced moments.

- Balancing - as mentioned above, balancing due to water ingress became a problem, but balancing overall was a challenge as the prototype proved to be very sensitive to small weight imbalances. An inordinate amount of time was spent getting the vessel balanced.

- Launching Level - holding the vessel in the desired position just prior to the start of each test run meant that the dynamics were affected just at the start, which resulted in anomalies like the “nodding” effect.

- Towing Tank Difficulties - variation in the speed of the towing tank resulted in some inconsistency in test results and uncertainty in the exact measurements.

- Canards Maxing out in Limited Range - full extension of the canards resulted in only a 300 mm height range. This was sufficient for proving dynamics, but would need to be adjusted for fuller depth range movement.

6.1.3 Controller

The stability of the prototype during open-loop testing suggested that a simple control strategy would be adequate. In the simulation this proved to be the case. Separate controllers were designed for the longitudinal (depth) and lateral (roll angle) motions. These were tested separately and a damped and accurate response was obtained for both. The motions were then combined and though some additional dynamics were seen due to interdependence between the axes, the motion was damped and stable in both roll and depth response. Further study into more complex controllers may determine a method to achieve a faster response, especially in depth control.

Based on these findings this design is both open loop stable and closed loop controllable and is suitable for further study to build a full-scale prototype.

6.2 Recommendations

Based on the results and conclusions of this study the following recommendations are made.

6.2.1 Improve Reliability of Prototype

The prototype used for this model was a totally original platform and thus experienced certain reliability issues, especially in relation to water ingress, which affected both the sensors and weight balance. These issues invalidated a number of the test runs, and also made more comprehensive testing impractical. The platform should be revisited to improve the reliability, robustness, and ease of use. Further test runs should be conducted to verify the physical properties of the prototype and the dynamic test data obtained in this study. Some limitations discovered were that the canards were not suitable to give a full range of motion for the prototype, so the canards should be modified to give a higher moment.

Some thought could also be given to the reliability of the towing tank, which experienced maintenance issues during this study, and the fine control of the speed, so that a smoother flow rate could be achieved, which would allow for a more accurate study. A flow meter could also be utilised to verify that the speed reading from the control module is accurate.

6.2.2 Include Rotor Blade Rotation into Study and Prototype

In this study the rotor blades were assumed to be a permeable disk to simplify modelling. The next step should be to modify the platform to allow for controllable rotating blades and to include modelling of the blade rotation into the mathematical model. This will allow study of further situations such

as rotor failure or a mismatch in rotor speed. The effect of pitching the blade angle should also be further investigated.

6.2.3 More Comprehensive Study of Added Mass Effect

When searching the literature it becomes clear that the concept of added mass is generally poorly or only briefly explained, even though its effect on hydrodynamics is clearly significant. A detailed study should be conducted on the added mass effect on various simple shapes. Then tests should be performed using the OCEC platform to empirically determine the accurate added mass effect for accelerations in all directions, and compare these results to theoretically calculated values.

6.2.4 Further Study of Wing Lift Force Discrepancy

Focused tests in a wind tunnel should be conducted to determine the source of the discrepancy between the theoretical and measured wing lift force. These tests could include measuring the flow rate over the wing and induced forces first when isolated, and then with structures placed around it disrupting the flow, such as nacelles and turbines.

6.2.5 Testing of the Control Strategy

The control strategy designed and simulated in this study should be implemented on the prototype and tuned to suit the real-world conditions experienced. Only by this testing can the question of the controllability of the model be answered accurately. Ideally, testing should include a physical method to isolate the longitudinal and lateral motions from each other so that their control response can first be tested independently before allowing the device free motion and then testing the combined response.

Appendices

Appendix A

Testing Details

A.1 Building Prototype

The following sections describe the detail of the design and construction of the various elements of the prototype.

A.1.1 Body Externals

The body consists of the two nacelles, the fuselage, the wings and the control surfaces (canards and ailerons) as shown in A.1. The nacelles and fuselage

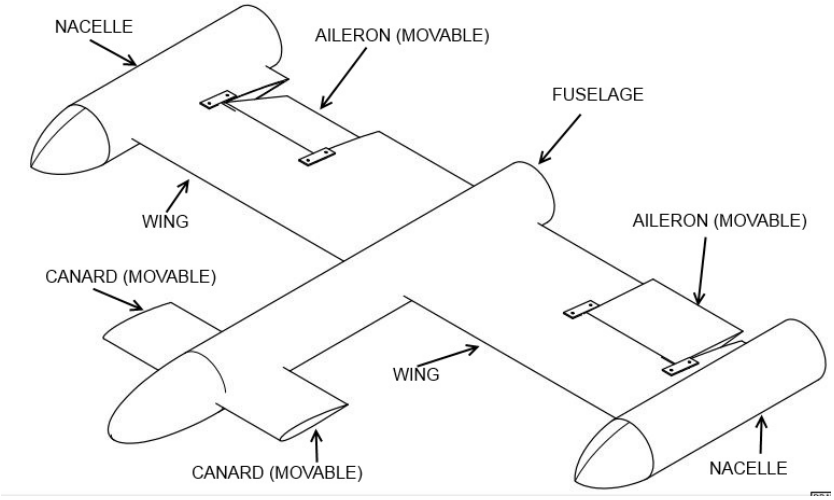

Figure A.1: OCEC body design

were made from fibreglass tubes, constructed by glassing over 101 mm aluminium tubes. The noses were shaped from hard foam, and then also glassed over to create hollow nose cones, joined in a single "one-piece" body (A.2). The profile selected for the wings was NACA5012, as it features good characteristics for a hydrofoil. The wings were constructed by CNC cutting a lattice

Figure A.2: OCEC prototype body

and rib structure from plywood as shown in A.3. The gaps in between the

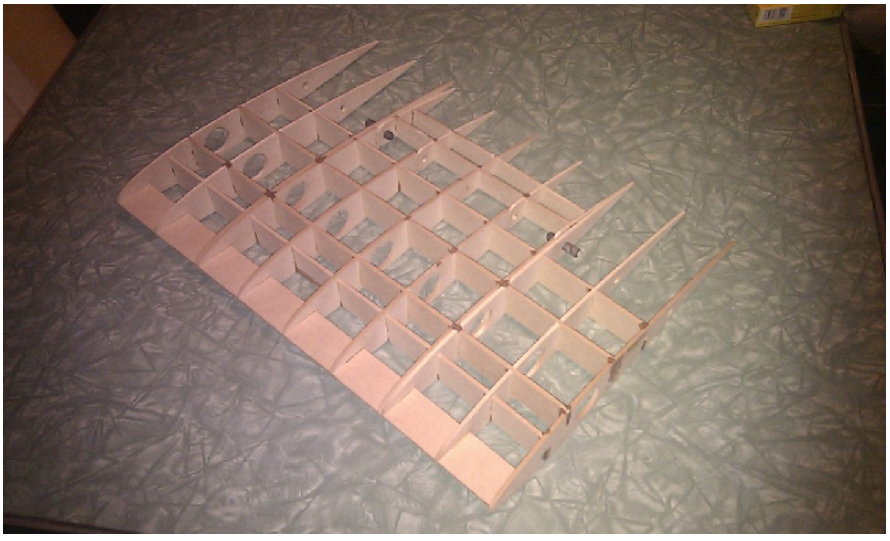

Figure A.3: OCEC wing structure

wood were filled with pieces of hard foam, and then glassed over, painted and sealed for waterproofing. Allowance was made for weight to be added to the nose of the fuselage and hubs to aid in balancing centre of gravity.

A.1.2 Body Internals

Inside the nacelles a shaft system (see Section A.4) was built to allow the turbines to rotate freely in the current. This system consisted of an aluminium outer tube, to which was fixed two aluminium disks, cut to allow bearing

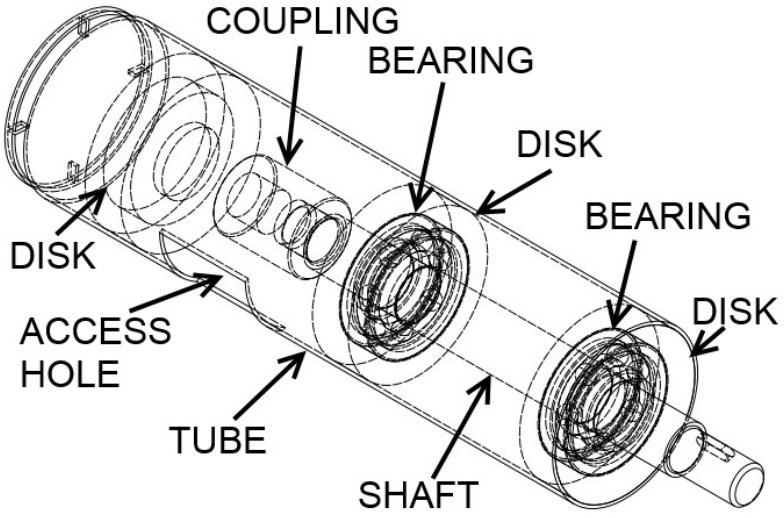

Figure A.4: Nacelle internals design

mounting. 30 mm inner diameter bearings were mounted inside these disks. The shaft was made from 30 mm stainless steel round bar and was mounted into the bearings. There was a coupling at the forward end of the shaft to which a friction brake mechanism was attached, to control the rotational speed, which was mounted into a third aluminium disk.

This assembly was fixed to fibreglass body by being bolted though at the rear end of the nacelles. A fibreglass cover was then fixed over the end plate with the shaft protruding and bolted into the end disk with shaft seals as the shaft exited the cover, to seal off the tube from water ingress. See Appendix A.5.

Figure A.5: Nacelle fabricated

A.1.3 Hub and Blades

The blade and hub assembly is shown in A.6. The blade profile was based

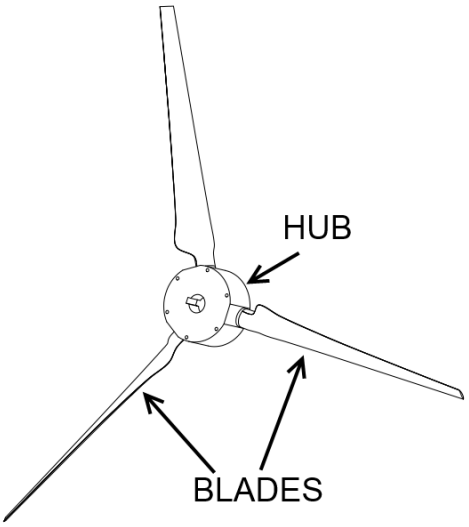

Figure A.6: Hub and blades design

upon the design by Richard Stanford [12] for ease of manufacturing. The blades were machined from 6061 grade aluminium blocks, using the 6 axis CNC milling machine from Stellenbosch University (A.7). The hubs were

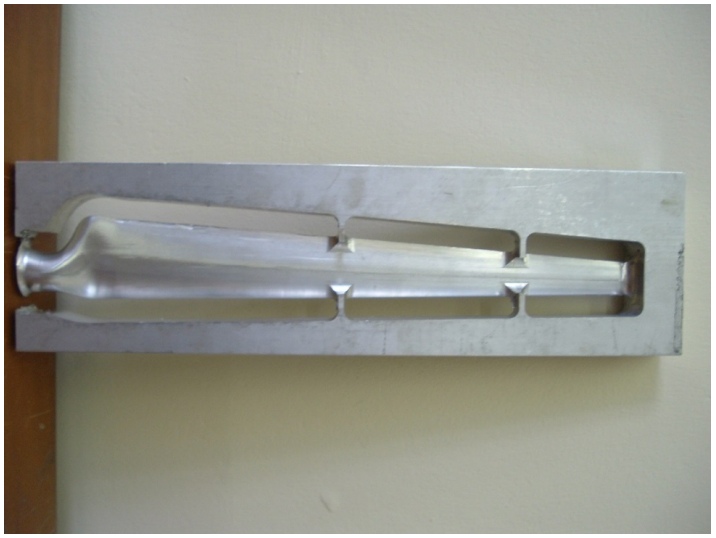

Figure A.7: Machined blade

also machined from 6061 grade aluminium. They were fixed to the shafts with keys and a nut to secure to the threaded end of the shaft.

Figure A.8: Assembling hub and blades

A.1.4 Actuators

There are four moving surfaces on the prototype, the two canards and the two ailerons. The canards were fixed together, and actuated by a single high torque waterproof servo motor (Figure A.9) via an actuator arm mounted inside the nose of the fuselage. The ailerons were separately actuated by indi-

Figure A.9: Servo motor and actuator arms

vidual high torque servo motors. The ailerons had an axle that was embedded into the wing that allowed them to pivot as shown in Figure A.10. They were then attached via an actuator arm on the top of the flap to the servo motor that was embedded into the wing body. The servo motors were controlled by

an Arduino Uno3 microcontroller, given instructions via USB communication to a Windows computer running Matlab. The microcontroller was mounted on a plate outside the water, with a 10 m cable running down to the prototype. To compensate for chatter in the motors an on-board battery pack was installed into the fuselage to provide power.

Figure A.10: Aileron and servo motor assembled

A.1.5 Sensors

The principle sensor is a VectorNav VN-100 Inertial Measurement Unit (IMU) as shown in Figure A.11, mounted inside the fuselage, heavily water-protected and connected to computer feedback via a 10 m USB cable. Use was also made of the trolley's onboard 50 kg load cell (Figure A.12), for measuring the tension in the tether cable, and onboard 750 mm linear sensors (Figure A.13) which were used to give depth readings, and to verify the gyro angle readings. The technical specifications of the IMU are shown in Table A.1.

A.1.6 Attachment to Trolley

The prototype was dragged by an adjustable pulley roller just above the water surface, while all signals and electronics were in cables dragging behind the prototype. Fishing line was used to constrain the model from hitting the bottom of the towing tank, and a winch was used for repairs and adjustments. Note that test runs were performed upside down to prevent drag from a tether pole. The tether used was 3 mm steel rope, which was attached to the prototype with hooks embedded into the front of the wings. Fishing line was used to constrain the prototype from hitting the bottom of the towing tank. A winch was used to lift the prototype out of the water for repairs

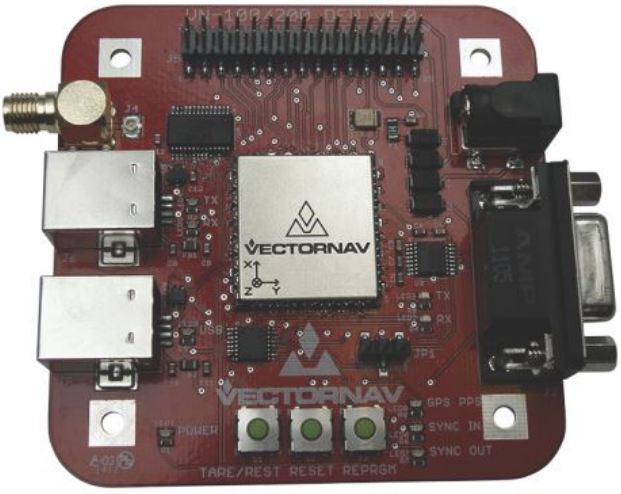

Figure A.11: VectorNav VN-100 IMU

Figure A.12: HBM RSCM-50kg 25152

and adjustments. Once fully assembled the prototype looked as shown in Figure A.15.

A.1.7 Examples of Experimental Data

Some examples of the data extracted from the various sensors during test runs are shown in Tables A.4 and A.5,

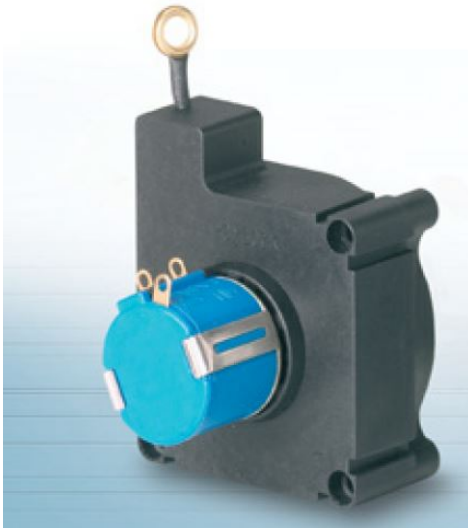

Figure A.13: Micro-Epsilon WPS-750-MK30-P10

Figure A.14: Force meter and pulley wheel

Table A.1: VectorNav specifications

TECHNICAL SPECIFICATIONS	
Attitude & Heading	
Range (Heading/Roll):	±180 °
Range (Pitch):	±90 °
Static Accuracy (Heading):	2.0 °
Static Accuracy (Pitch/Roll):	0.5 °
Angular Resolution:	< 0.05 °
Repeatability:	< 0.2°
Output Rate:	200 Hz*
Gyro Specifications	
Range:	±2000 °/s
In-Run Bias Stability:	< 10 °/hr
Linearity:	< 0.1 % FS
Noise Density:	0.005 °/s /√Hz
Bandwidth:	256 Hz
Alignment Error:	±0.05 °
Accelerometer Specifications	
Range:	±16 g
Linearity:	< 0.5 % FS
Noise Density:	0.4 mg/√Hz
Bandwidth:	260 Hz
Alignment Error:	±0.05 °
Magnetometer Specifications	
Range:	±2.5 Gauss
Linearity:	< 0.1 %
Noise Density:	140 µGauss/√Hz
Bandwidth:	200 Hz
Alignment Error:	±0.05 °
Pressure Sensor Specifications**	
Range:	10 to 1200 mbar
Resolution:	0.042 mbar
Accuracy:	±1.5 mbar
Error Band:	±2.5 mbar
Bandwidth:	200 Hz
Environment	
Operating Temp:	-40°C to +85°C
Storage Temp:	-40°C to +85°C

Table A.2: Load cell specifications

Technical Data

Type		RSCA C1						
Accuracy class according to OIML R 60 Max. numbers of load cell intervals (n_{LC})		C1 1000						
Nominal (rated) capacity (E_{max})		50 kg	100 kg	200 kg	500 kg	1 t	2 t	5 t
Minimum LC verification interval (v_{min})	% of E_{max}	0.0286						
Sensitivity (C_n)	mV/V	2						
Sensitivity tolerance	%	±0.2500						
Temperature effect on sensitivity (TK_C) [1]	% of C_n / 10 K	±0.0230 [1]						
Temperature effect on zero signal (TK_0)		±0.0400						
Hysteresis error (d_{hy}) [1]	% of C_n	±0.0500 [1]						
Non-Linearity (d_{lin}) [1]		±0.1000 [1]						
Creep (d_{cr}) 30 min.		±0.0490						
Input resistance (R_{LC}) (nominal)	Ω	350						
Output resistance (R_0)		350 ±1.5						
Reference excitation voltage(U_{ref})	V	5						
Nominal range of excitation voltage (B_U)		0.5 ... 12						
Insulation resistance (R_{is})	GΩ	> 5						
Nominal range of ambient temperature (B_T)	°C [°F]	–10 ... +40 [+14 ... +104]						
Service temperature range (B_{tu})		–30 ... +70 [–22 ... +158]						
Storage temperature range (B_{tl})		–50 ... +85 [–58 ... +185]						

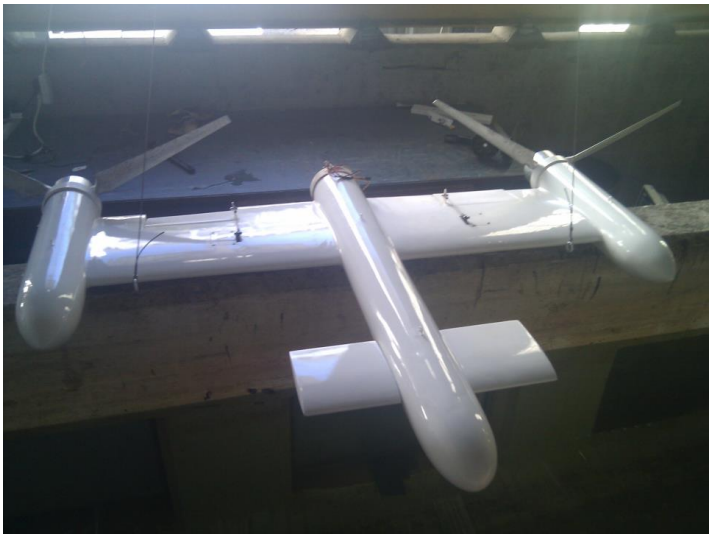

Figure A.15: Fully assembled prototype

Table A.3: Linear sensor specifications

			WPS-50 MK30	WPS-150 MK30	WPS-250 MK30	WPS-500 MK30	WPS-750 MK30
Output			P	P	P	P/E	P/E
Measuring range			50 mm	150 mm	250 mm	500 mm	750 mm
Linearity	wire pot.	±0.5 % FSO	0.25 mm	-	-	-	-
	wire pot.	±0.25 % FSO	-	0.375 mm	0.625 mm	1.25 mm	1.87 mm
	hybrid pot.	±0.1 % FSO	-	-	0.25 mm	0.5 mm	0.75 mm
	encoder	±0.05 % FSO	-	-	-	0.25 mm	0.375 mm
Resolution	encoder		-	-	-	10 pulses/mm	6.7 pulses/mm
			-	-	-	0.1 mm	0.15 mm
	wire pot.		0.1 mm	0.1 mm	0.1 mm	0.15 mm	0.2 mm
	hybrid pot.		quasi infinite				
Sensor element			wire- / hybrid-potentiometer or incremental encoder				
Temperature range			-20 ... +80 °C				
Material	housing		plastic				
	draw wire		coated polyamid stainless steel (ø 0.36 mm)				

Table A.4: VectorNav data example

Time Stamp	Yaw (deg)	Pitch (deg)	Roll (deg)	Mag X	Mag Y	Mag Z	Acceleration X (m/s^2)	Acceleration Y (m/s^2)	Acceleration Z (m/s^2)	Compensated Angular Rate X (deg/sec)	Compensated Angular Rate Y (deg/sec)	Compensated Angular Rate Z (deg/sec)
2013-07-08T14:41:43.54	157.129	7.070	145.723	0.693	-0.209	2.485	1.175	-5.466	8.012	0.217	-0.034	-0.035
2013-07-08T14:41:43.57	157.129	7.072	145.724	0.694	-0.207	2.484	1.250	-5.495	8.039	0.115	0.003	0.054
2013-07-08T14:41:43.59	157.130	7.071	145.729	0.696	-0.210	2.481	1.173	-5.489	8.073	0.125	0.018	-0.065
2013-07-08T14:41:43.62	157.129	7.077	145.728	0.693	-0.210	2.480	1.247	-5.497	8.076	0.100	-0.074	0.037
2013-07-08T14:41:43.64	157.130	7.078	145.730	0.693	-0.206	2.480	1.210	-5.498	7.994	0.161	0.042	0.115
2013-07-08T14:41:43.67	157.130	7.077	145.735	0.694	-0.205	2.479	1.223	-5.462	8.066	0.049	-0.130	0.053
2013-07-08T14:41:43.69	157.130	7.076	145.735	0.692	-0.210	2.476	1.166	-5.499	8.050	0.212	-0.078	0.063
2013-07-08T14:41:43.72	157.131	7.076	145.739	0.693	-0.209	2.481	1.238	-5.496	8.069	0.026	-0.009	0.041
2013-07-08T14:41:43.74	157.131	7.074	145.744	0.692	-0.208	2.484	1.174	-5.457	8.064	0.100	0.017	0.037
2013-07-08T14:41:43.77	157.131	7.073	145.749	0.693	-0.205	2.485	1.231	-5.497	8.095	0.161	-0.034	-0.069
2013-07-08T14:41:43.79	157.132	7.072	145.749	0.694	-0.208	2.484	1.213	-5.511	8.093	0.103	-0.008	-0.006
2013-07-08T14:41:43.82	157.133	7.072	145.750	0.694	-0.208	2.481	1.231	-5.498	8.065	0.077	-0.037	-0.087
2013-07-08T14:41:43.84	157.133	7.069	145.749	0.694	-0.206	2.484	1.165	-5.465	8.088	0.107	-0.022	0.045
2013-07-08T14:41:43.87	157.133	7.070	145.749	0.693	-0.207	2.484	1.229	-5.495	8.041	0.094	-0.077	0.007
2013-07-08T14:41:43.89	157.132	7.067	145.747	0.691	-0.208	2.483	1.198	-5.514	8.117	0.073	0.053	-0.061
2013-07-08T14:41:43.92	157.133	7.064	145.745	0.694	-0.208	2.482	1.235	-5.500	8.081	0.114	-0.034	0.003
2013-07-08T14:41:43.94	157.133	7.061	145.742	0.694	-0.208	2.480	1.189	-5.485	8.052	0.116	-0.036	-0.164
2013-07-08T14:41:43.97	157.134	7.061	145.749	0.692	-0.205	2.480	1.220	-5.491	8.104	0.163	0.046	0.162
2013-07-08T14:41:43.99	157.134	7.056	145.745	0.691	-0.208	2.480	1.168	-5.492	8.035	0.046	0.007	-0.117
2013-07-08T14:41:44.02	157.136	7.059	145.748	0.692	-0.206	2.474	1.225	-5.470	8.096	0.139	0.013	0.025
2013-07-08T14:41:44.04	157.136	7.057	145.748	0.694	-0.205	2.485	1.194	-5.506	8.034	0.031	0.110	-0.082
2013-07-08T14:41:44.07	157.138	7.055	145.749	0.692	-0.206	2.486	1.207	-5.501	8.077	-0.014	0.095	0.007
2013-07-08T14:41:44.09	157.140	7.054	145.750	0.693	-0.208	2.483	1.202	-5.478	8.065	0.120	-0.141	0.011
2013-07-08T14:41:44.12	157.141	7.055	145.748	0.693	-0.207	2.484	1.223	-5.476	8.060	0.134	-0.055	0.058
2013-07-08T14:41:44.14	157.142	7.052	145.747	0.693	-0.206	2.484	1.176	-5.484	8.053	0.151	0.101	-0.022
2013-07-08T14:41:44.17	157.143	7.050	145.749	0.693	-0.204	2.485	1.221	-5.483	8.040	0.035	0.031	0.037
2013-07-08T14:41:44.19	157.144	7.052	145.746	0.692	-0.209	2.481	1.197	-5.493	8.083	0.091	0.063	-0.095
2013-07-08T14:41:44.22	157.145	7.055	145.742	0.695	-0.208	2.481	1.225	-5.504	8.053	0.044	0.104	0.046
2013-07-08T14:41:44.24	157.146	7.050	145.739	0.695	-0.205	2.481	1.194	-5.508	8.033	0.085	0.083	0.072
2013-07-08T14:41:44.27	157.147	7.047	145.742	0.696	-0.205	2.481	1.209	-5.490	8.056	0.037	0.027	0.007
2013-07-08T14:41:44.29	157.149	7.045	145.743	0.692	-0.206	2.477	1.189	-5.478	8.044	0.076	0.092	0.033
2013-07-08T14:41:44.32	157.148	7.042	145.745	0.692	-0.210	2.481	1.226	-5.504	8.072	0.081	0.121	0.034
2013-07-08T14:41:44.34	157.150	7.038	145.747	0.694	-0.206	2.484	1.196	-5.507	8.080	-0.016	0.095	0.020
2013-07-08T14:41:44.37	157.151	7.040	145.749	0.693	-0.206	2.485	1.245	-5.499	8.061	-0.024	0.086	0.054
2013-07-08T14:41:44.39	157.153	7.038	145.746	0.695	-0.208	2.484	1.199	-5.522	8.042	0.038	0.083	0.007
2013-07-08T14:41:44.42	157.156	7.037	145.746	0.693	-0.206	2.483	1.218	-5.482	8.087	-0.005	0.053	-0.040
2013-07-08T14:41:44.44	157.159	7.037	145.744	0.694	-0.206	2.485	1.190	-5.501	8.036	0.156	0.029	-0.129
2013-07-08T14:41:44.47	157.162	7.042	145.749	0.695	-0.205	2.485	1.208	-5.481	8.106	0.119	0.079	-0.082
2013-07-08T14:41:44.49	157.164	7.045	145.746	0.693	-0.208	2.482	1.196	-5.500	8.007	0.007	-0.055	0.070

Table A.5: Linear and force meter data examples

Time	Speed (m/s)	Force (N)	Linear 1 (mm)	Linear 2 (mm)
103.34	0.357	102.23	35.81	34.34
103.36	0.362	101.75	34.83	32.87
103.39	0.362	100.90	33.85	31.39
103.41	0.357	100.53	32.87	29.43
103.44	0.362	100.17	32.38	28.45
103.46	0.362	99.68	31.39	27.47
103.49	0.362	99.19	30.41	25.51
103.51	0.362	98.59	29.43	24.04
103.54	0.362	98.22	28.45	23.06
103.56	0.362	97.74	27.47	21.58
103.59	0.367	97.25	26.49	20.60
103.61	0.362	96.52	25.51	19.13
103.64	0.362	95.79	24.53	17.66
103.66	0.362	94.94	23.55	16.68
103.69	0.362	94.21	22.07	15.70
103.71	0.362	93.36	21.09	14.23
103.74	0.362	92.39	19.62	13.24
103.76	0.362	91.66	18.64	12.26
103.79	0.362	90.68	17.66	11.28
103.81	0.362	89.71	15.70	9.81
103.84	0.362	88.86	13.73	8.34
103.86	0.362	87.89	12.75	6.87
103.89	0.362	87.16	11.77	5.89
103.91	0.362	86.43	9.81	4.41
103.94	0.362	86.07	7.85	2.94
103.98	0.362	85.58	6.87	1.47
104.01	0.362	85.21	6.38	0.49
104.05	0.362	84.97	5.89	-0.49
104.07	0.362	84.61	4.91	-1.96
104.1	0.362	84.49	4.91	-3.43
104.12	0.362	84.49	4.41	-4.41

Appendix B

Simulation Details

B.1 Coefficient Values

Table B.1: Values used in simulation model

Coefficient	Value	Coefficient	Value	Coefficient	Value
$A^t_{Fuselage}$	0.038	A^n_{Wing}	0.3	d_{Cable}	0.005
$A^n_{Fuselage}$	0.102	$A^n_{Turbine}$	1.01	P_{Cable}	150
$A^t_{Nacelle}$	0.076	A^n_{Canard}	0.03	ρ_{Cable}	2000
$A^n_{Nacelle}$	0.121	$A^n_{Aileron}$	0.06	E_{Cable}	11200000000
C^n_{PF}	1.2	C^n_{PT}	0.9	m	26.0
C^t_{PF}	0.73	C^t_{PT}	0.4	vol	0.0192
C^n_{PN}	1.2	C^n_{PC}	0.9	m_x	52.0
C^t_{PN}	0.73	C^t_{PC}	0.9	m_y	31.0
C^n_{PH}	see B.2	I_{xa}	25.0	m_z	45.0
C^t_{PH}	see B.3	I_{ya}	19.0	I_{za}	50.0

B.2 NACA5012 Coordinates

Table B.2: Naca5012 profile coordinates

X	Y	X	Y	X	Y
0.99591	0.00228	0.19674	0.10519	0.36841	-0.01581
0.98332	0.0053	0.14722	0.10201	0.43228	-0.01596
0.96256	0.01018	0.10381	0.09684	0.49736	-0.01537
0.93397	0.01672	0.06726	0.08992	0.56253	-0.01428
0.89801	0.02463	0.03818	0.08151	0.6267	-0.01287
0.85526	0.03361	0.01707	0.07189	0.68876	-0.01128
0.80644	0.04331	0	0.05	0.74764	-0.00964
0.75236	0.05339	0.017	0.02808	0.80232	-0.00801
0.69393	0.06349	0.03794	0.01835	0.85184	-0.00646
0.63212	0.07325	0.06672	0.00963	0.89535	-0.00503
0.56799	0.08233	0.10283	0.00209	0.93206	-0.00377
0.50264	0.09037	0.14567	-0.00415	0.96132	-0.00271
0.43719	0.09706	0.1945	-0.00902	0.98261	-0.00192
0.37278	0.10208	0.24852	-0.01252	0.99554	-0.00142
0.31051	0.10521	0.30681	-0.01473	0.99987	-0.00125
0.25148	0.10627				

B.3 NACA5012 Coefficients

Table B.3: Naca5012 coefficients

alpha (°)	Cl	Cm	Cd	alpha (°)	Cl	Cm	Cd	alpha (°)	Cl	Cm	Cd
-60	-0.99	-0.37125	1.485	-20	-0.63788	-0.0579	0.231616	21	1.075063	-0.06357	0.254287
-59	-1.0015667	-0.3636942	1.45477685	-19	-0.6107	-0.05247	0.209869	22	1.100809	-0.06946	0.277854
-58	-1.0119242	-0.3559969	1.42398744	-18	-1.267	-0.071	0.03382	23	1.125802	-0.07557	0.302288
-57	-1.021091	-0.3481673	1.39266928	-17	-1.2475	-0.0679	0.02685	24	1.15002	-0.08189	0.327561
-56	-1.0290849	-0.3402151	1.36086053	-16	-1.2157	-0.0589	0.02214	25	1.173445	-0.08841	0.35364
-55	-1.035923	-0.33215	1.32859994	-15	-1.1474	-0.0522	0.01945	26	1.196058	-0.09512	0.380495
-54	-1.0416216	-0.3239817	1.29592682	-14	-1.0796	-0.0443	0.01715	27	1.217843	-0.10202	0.408093
-53	-1.0461963	-0.3157202	1.26288098	-13	-1.0091	-0.0362	0.01532	28	1.238784	-0.1091	0.436399
-52	-1.049662	-0.3073757	1.22950268	-12	-0.9087	-0.0338	0.01353	29	1.258867	-0.11634	0.46538
-51	-1.0520328	-0.2989581	1.19583257	-11	-0.7759	-0.0378	0.012	30	1.278077	-0.12375	0.495
-50	-1.0533218	-0.2904779	1.1619117	-10	-0.646	-0.0409	0.01064	31	1.296403	-0.13131	0.525223
-49	-1.0535416	-0.2819453	1.12778137	-9	-0.5127	-0.0448	0.00943	32	1.313834	-0.139	0.556013
-48	-1.052704	-0.2733708	1.09348318	-8	-0.3952	-0.0451	0.00838	33	1.330357	-0.14683	0.587331
-47	-1.05082	-0.2647647	1.05905891	-7	-0.2871	-0.0432	0.00746	34	1.345963	-0.15478	0.619139
-46	-1.0479001	-0.2561376	1.0245505	-6	-0.1793	-0.0414	0.0067	35	1.360643	-0.16285	0.6514
-45	-1.0439541	-0.2475	0.99	-5	-0.0701	-0.0401	0.00612	36	1.374387	-0.17102	0.684073
-44	-1.0389914	-0.2388624	0.9554495	-4	0.0397	-0.0389	0.00575	37	1.387188	-0.17928	0.717119
-43	-1.0330207	-0.2302353	0.92094109	-3	0.149	-0.0378	0.00553	38	1.399036	-0.18762	0.750497
-42	-1.0260506	-0.2216292	0.88651682	-2	0.2565	-0.0363	0.00543	39	1.409924	-0.19604	0.784167
-41	-1.0180892	-0.2130547	0.85221863	-1	0.3601	-0.0339	0.00556	40	1.419844	-0.20452	0.818088
-40	-1.0091444	-0.2045221	0.8180883	0	0.471	-0.0332	0.00615	41	1.428789	-0.21305	0.852219
-39	-0.999224	-0.1960419	0.78416743	1	0.6084	-0.0394	0.00715	42	1.436751	-0.22163	0.886517
-38	-0.9883358	-0.1876243	0.75049732	2	0.7272	-0.0422	0.00833	43	1.443721	-0.23024	0.920941
-37	-0.9764875	-0.1792798	0.71711902	3	0.8161	-0.0385	0.00959	44	1.449691	-0.23886	0.955449
-36	-0.9636871	-0.1710183	0.68407318	4	0.9089	-0.0358	0.01089	45	1.454654	-0.2475	0.99
-35	-0.9499428	-0.16285	0.65140006	5	1.005	-0.034	0.01223	46	1.4586	-0.25614	1.024551
-34	-0.935263	-0.1547849	0.61913947	6	1.1	-0.0323	0.01371	47	1.46152	-0.26476	1.059059
-33	-0.9196568	-0.1468327	0.58733072	7	1.1919	-0.0304	0.01536	48	1.463404	-0.27337	1.093483
-32	-0.9031336	-0.1390031	0.55601256	8	1.2769	-0.0278	0.01732	49	1.464242	-0.28195	1.127781
-31	-0.8857035	-0.1313058	0.52522315	9	1.3482	-0.0234	0.01983	50	1.464022	-0.29048	1.161912
-30	-0.8673773	-0.12375	0.495	10	1.4072	-0.0176	0.02237	51	1.462733	-0.29896	1.195833
-29	-0.8481667	-0.116345	0.46537993	11	1.4396	-0.0107	0.02703	52	1.460362	-0.30738	1.229503
-28	-0.8280842	-0.1090998	0.43639903	12	1.4755	-0.0071	0.03231	53	1.456896	-0.31572	1.262881
-27	-0.8071432	-0.1020232	0.4080926	13	1.4904	-0.0059	0.04074	54	1.452322	-0.32398	1.295927
-26	-0.7853583	-0.0951238	0.38049514	14	0.875749	-0.02897	0.115882	55	1.446623	-0.33215	1.3286
-25	-0.762745	-0.0884101	0.35364027	15	0.906081	-0.03316	0.132635	56	1.439785	-0.34022	1.360861
-24	-0.7393202	-0.0818902	0.3275607	16	0.935841	-0.03761	0.150432	57	1.431791	-0.34817	1.392669
-23	-0.7151019	-0.0755721	0.30228821	17	0.965	-0.04231	0.169253	58	1.422624	-0.356	1.423987
-22	-0.6901093	-0.0694634	0.2778536	18	0.993528	-0.04727	0.189073	59	1.412267	-0.36369	1.454777
-21	-0.664363	-0.0635717	0.25428662	19	1.021398	-0.05247	0.209869	60	1.4007	-0.37125	1.485
				20	1.048585	-0.0579	0.231616				

B.4 Simulink Block Diagrams

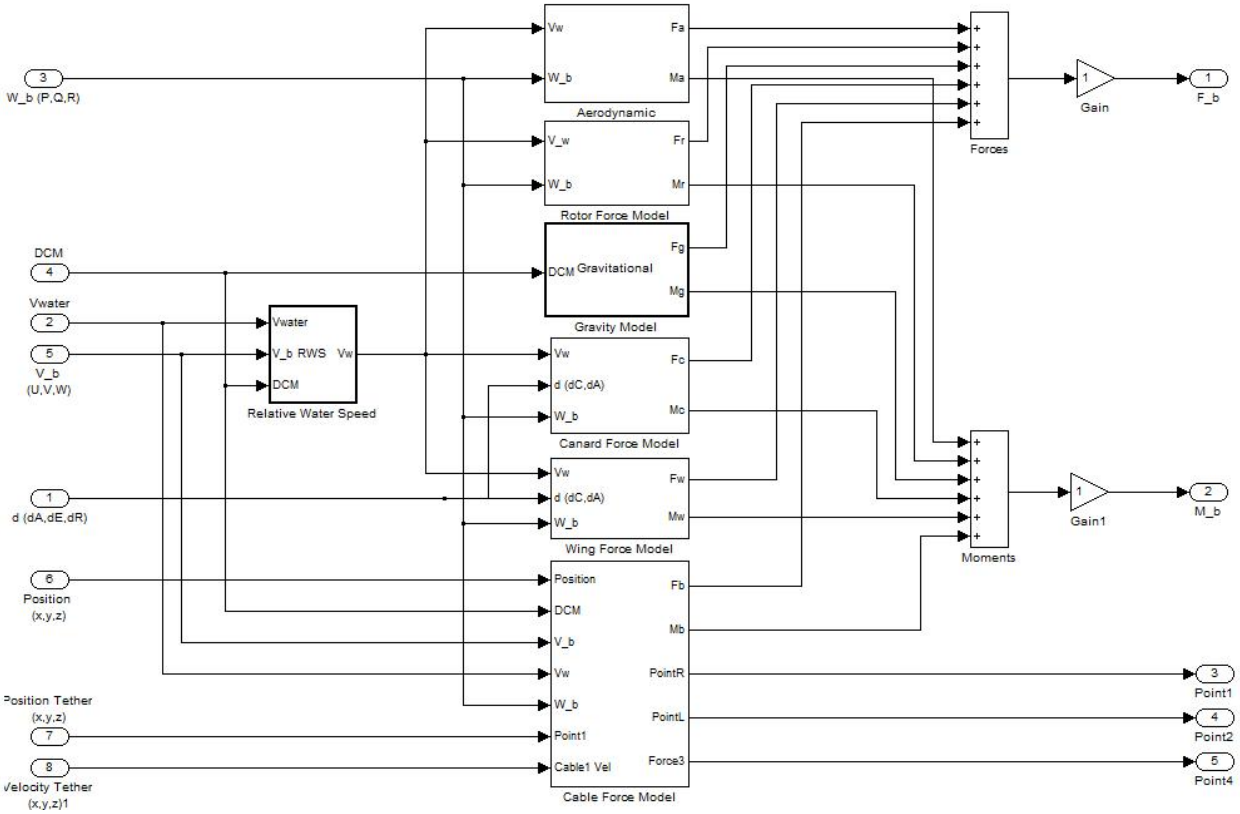

Figure B.1: Simulink force model block diagram

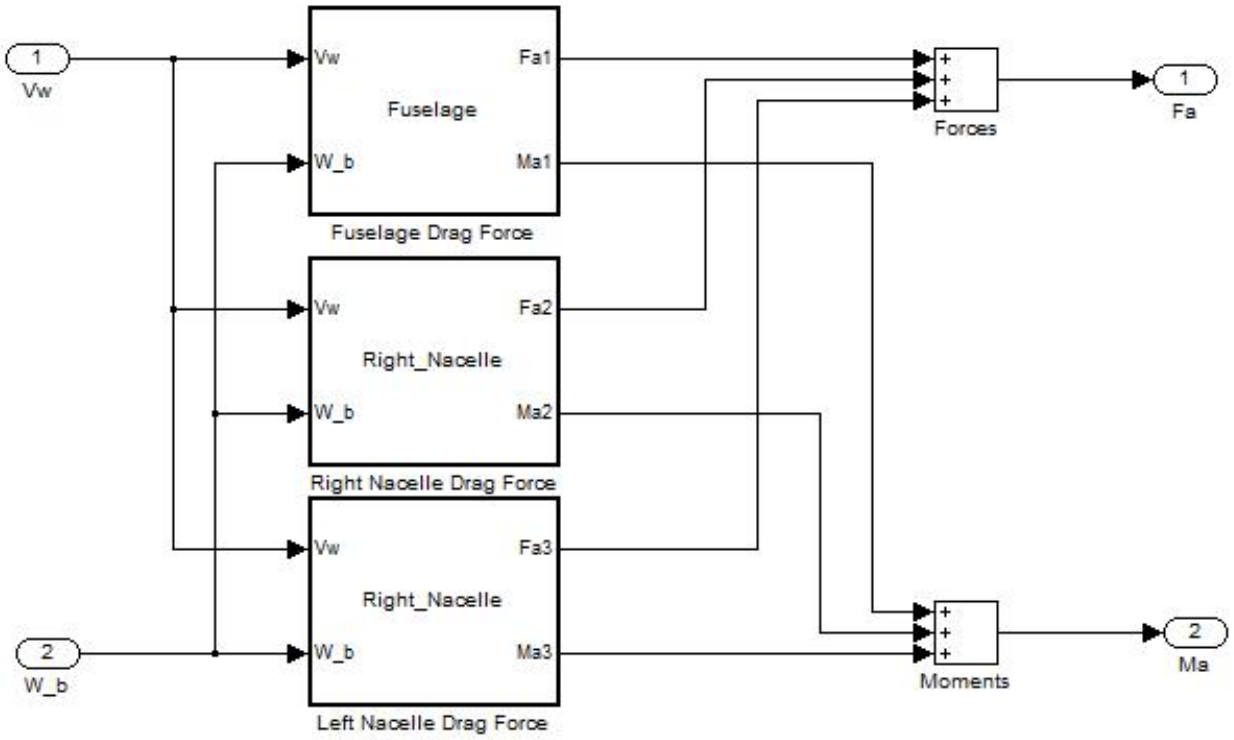

Figure B.2: Simulink aerodynamic force block diagram

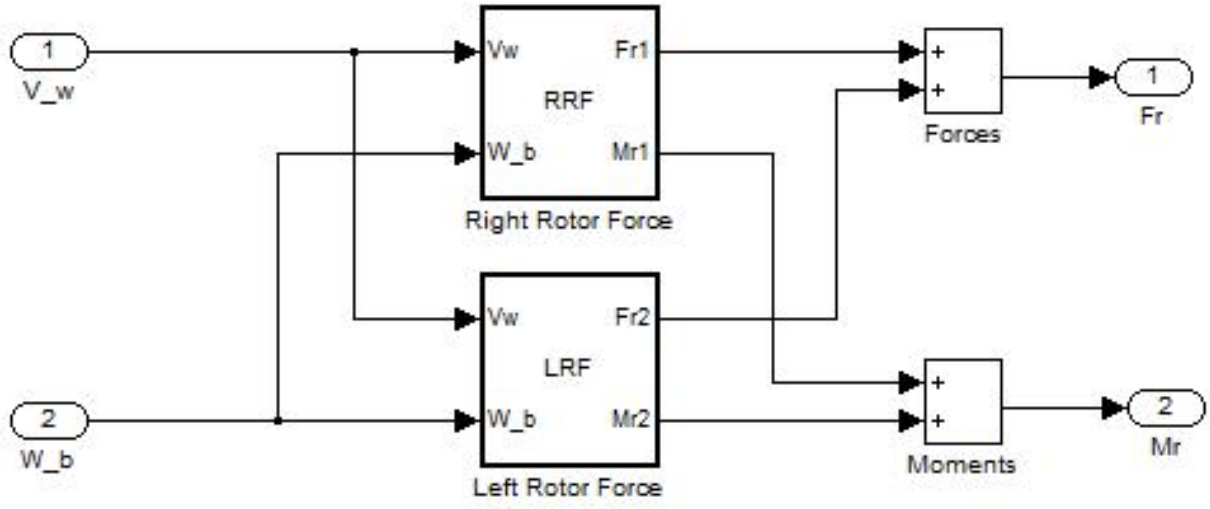

Figure B.3: Simulink rotor force block diagram

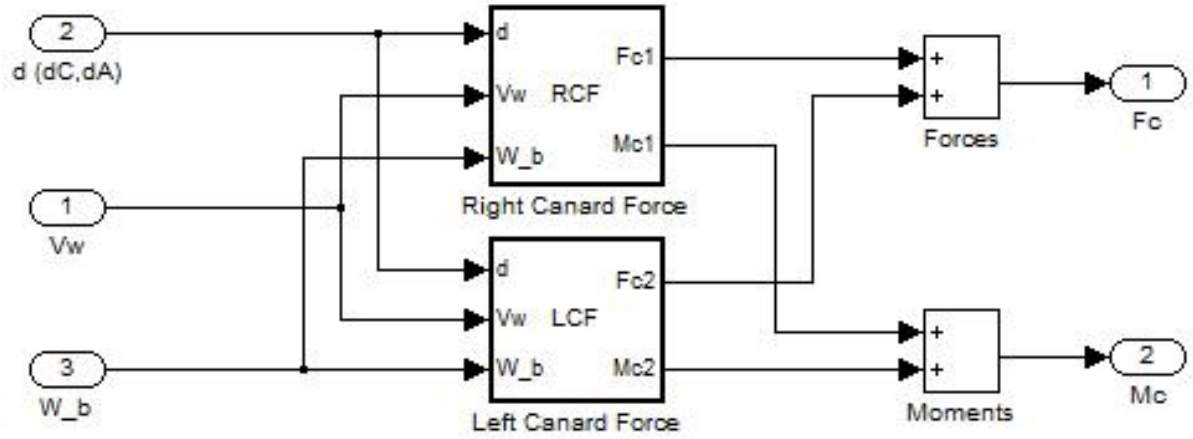

Figure B.4: Simulink canard force block diagram

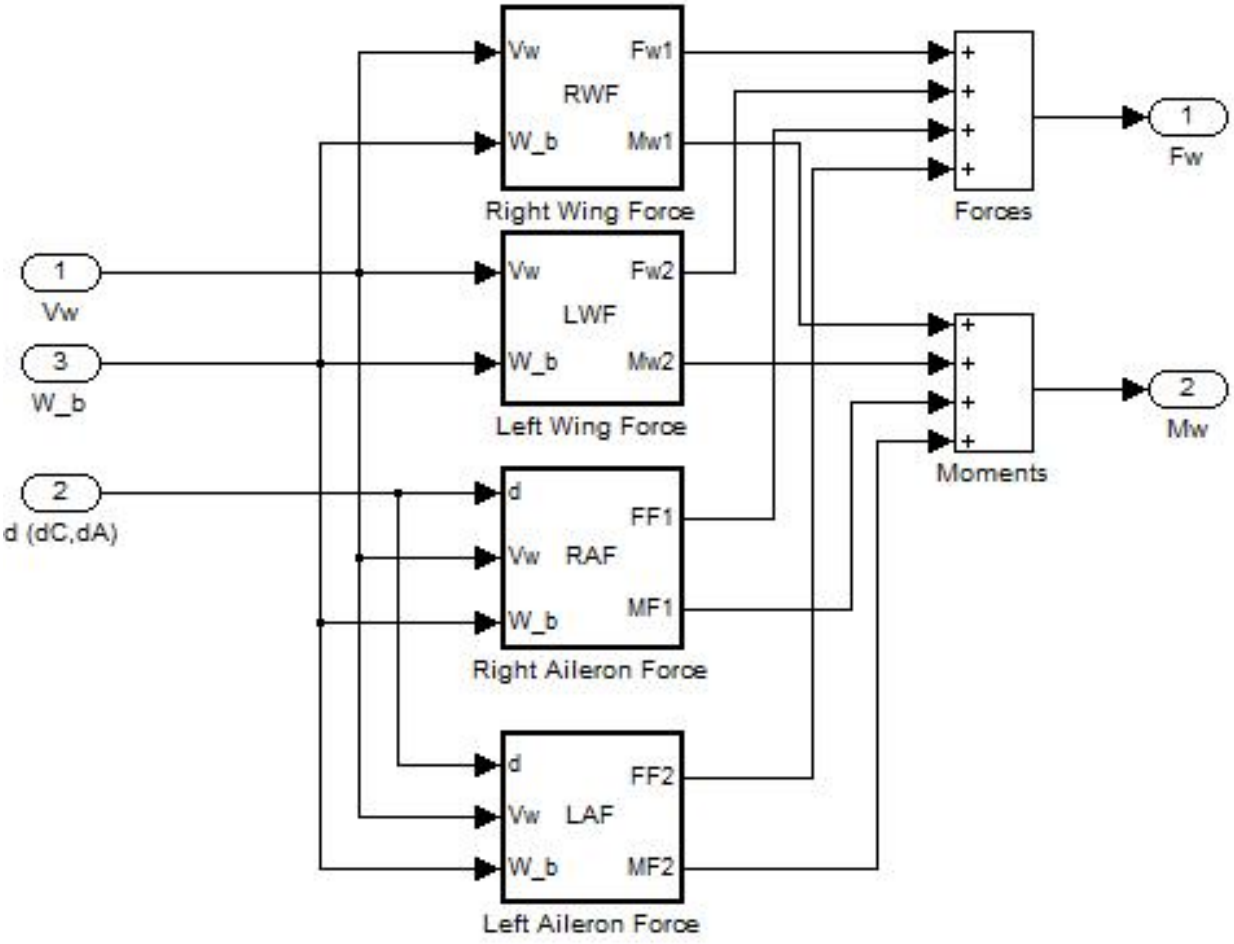

Figure B.5: Simulink wing force block diagram

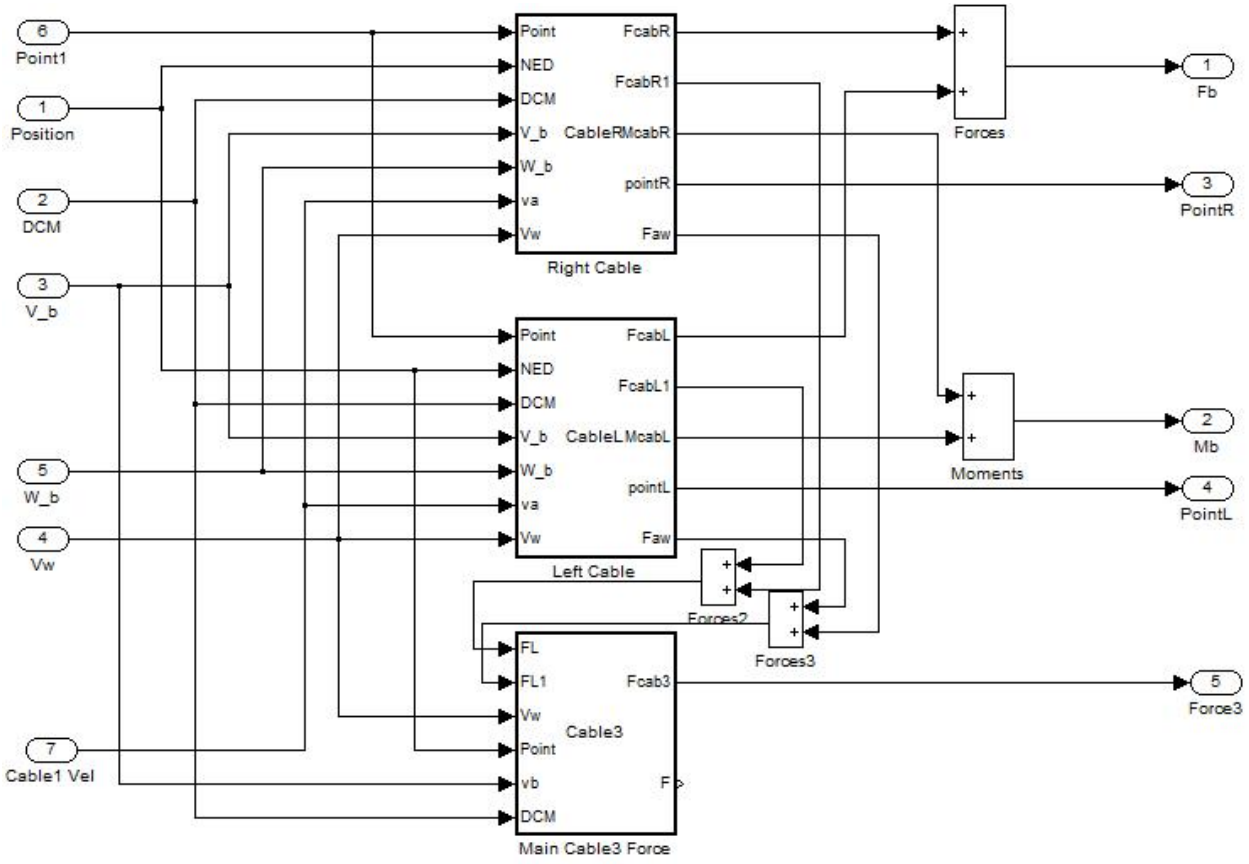

Figure B.6: Simulink cable force block diagram

B.5 Detailed Simulation Results

Detailed figures for the results of the simulation versus actual results are shown in Table B.4.

Table B.4: Simulation results

		Actual	Simulation	Error (%)
Depth	Time	25	22	12.0
	Value	-605	-610	1.4
	Time	26	27	3.8
Pitch	Value	193	194	7.1
	Frequency	0.11	0.093	15.5
Depth	Time	22	24	9.1
Canard +30°	Value	-583	-578	14.8
Pitch	Time	24	18	25.0
Canard	Value	1.6	0.5	68.8
+30°	Frequency	0.1	0.07	30.0
Depth	Time	18	19	5.6
Canard -30°	Value	-790	-800	5.6
Pitch	Time	32	26	18.8
Canard	Value	173	172	8.3
-30°	Frequency	0.056	0.08	42.9
	Time	19	22	15.8
Roll	Value	11	10.5	4.5
	Frequency	0.19	0.2	5.3
Yaw	Time	6	11	83.3

Appendix C

Details of Linearisation Calculations

C.1 Linearising about Trim

To perform this analysis, the vessel will be taken as in equilibrium at Trim condition, and that all deviations from the Trim condition are small.

C.1.1 General Equations of Motion and States

Considering the Trim conditions it's noted that:

$$\tau_T = \nu_T = \begin{bmatrix} 0 & 0 & 0 \\ 0 & 0 & 0 \end{bmatrix} \tag{C.1.1}$$

And:

$$\eta_T = \begin{bmatrix} x_T & 0 & z_T \\ 0 & \Theta_T & 0 \end{bmatrix} \tag{C.1.2}$$

Where:

τ_T , ν_T, η_T are the states at Trim.

Given the above, and the fact that all deviations about the Trim condition are small, the general equations of motion of 3.2.1 and 3.2.2 can be simplified and re-written to obtain expressions for the states to fit the form of 5.1.1. For the accelerations it can be determined that:

$$\begin{aligned} \Delta\dot{u} &= \frac{X}{m_x} + vr - wq \approx \frac{X}{m_x} \\ \Delta\dot{v} &= \frac{Y}{m_y} - ur + wp \approx \frac{Y}{m_y} \\ \Delta\dot{w} &= \frac{Z}{m_z} + uq - vp \approx \frac{Z}{m_z} \end{aligned} \tag{C.1.3}$$

Where:

m_x , m_y, m_z are the mass of the vessel plus the inertia due to the added mass effect in each direction.

and:

$$\begin{aligned}\Delta\dot{p} &= \frac{L}{I_{xa}} - qr\frac{I_{za} - I_{ya}}{I_{xa}} \approx \frac{L}{I_{xa}} \\ \Delta\dot{q} &= \frac{M}{I_{ya}} - pr\frac{I_{xa} - I_{za}}{I_{ya}} \approx \frac{M}{I_{ya}} \\ \Delta\dot{r} &= \frac{N}{I_{za}} - pq\frac{I_{ya} - I_{xa}}{I_{za}} \approx \frac{N}{I_{za}}\end{aligned} \tag{C.1.4}$$

Where:

I_{xa} , I_{ya}, I_{za} are the moments of inertia of the vessel plus the inertia due to the added mass effect about each axis.

Using the conditions at Trim, the velocity deviations about Trim can be simplified to:

$$\begin{aligned}\Delta\dot{x} &\approx -\sin\Theta_T\Delta w + \cos\Theta_T\Delta u \\ \Delta\dot{y} &\approx \Delta v \\ \Delta\dot{z} &\approx -\sin\Theta_T\Delta u + \cos\Theta_T\Delta w\end{aligned} \tag{C.1.5}$$

$$\begin{aligned}\Delta\dot{\theta} &\approx \Delta q \\ \Delta\dot{\phi} &\approx \Delta p + \Delta r\tan\Theta_T \\ \Delta\dot{\psi} &\approx \Delta r\sec\Theta_T\end{aligned} \tag{C.1.6}$$

For linearisation it's also useful to note that:

$$\begin{aligned}\sin(\Theta_T + \Delta\theta) &\approx \sin\Theta_T + \cos\Theta_T\Delta\theta \\ \cos(\Theta_T + \Delta\theta) &\approx \cos\Theta_T - \sin\Theta_T\Delta\theta\end{aligned} \tag{C.1.7}$$

Using all the above, the DCM at Trim simplifies to:

$$J_1(\eta_2)^T = \begin{bmatrix} \cos\Theta - \sin\Theta_T\Delta\theta & \Delta\psi & -\sin\Theta_T - \Delta\theta \\ -\Delta\psi + \sin\Theta_T\Delta\phi & 1 & \Delta\phi \\ \sin\Theta_T + \Delta\theta & -\Delta\phi + \sin\Theta_T\Delta\psi & \cos\Theta_T - \sin\Theta_T\Delta\theta \end{bmatrix} \tag{C.1.8}$$

To determine C.1.3 and C.1.4 the expressions for τ are required. From Chapter 3 they are the sum of the restoring, hydrodynamic, wing, turbine, and tether forces and moments. These need to be expressed in terms of the state deviations.

$$\begin{aligned}\tau(\mathbf{x_T} + \Delta\mathbf{x}) =& \tau_G(\mathbf{x_T} + \Delta\mathbf{x}) + \tau_B(\mathbf{x_T} + \Delta\mathbf{x}) + \tau_P(\mathbf{x_T} + \Delta\mathbf{x}) \\ &+ \tau_R(\mathbf{x_T} + \Delta\mathbf{x}) + \tau_H(\mathbf{x_T} + \Delta\mathbf{x}) + \tau_C(\mathbf{x_T} + \Delta\mathbf{x})\end{aligned} \tag{C.1.9}$$

Given C.1.1 and noting that all expressions will be linearised:

$$\tau(\Delta\mathbf{x}) = \tau_G(\Delta\mathbf{x}) + \tau_B(\Delta\mathbf{x}) + \tau_P(\Delta\mathbf{x}) + \tau_R(\Delta\mathbf{x}) + \tau_H(\Delta\mathbf{x}) + \tau_C(\Delta\mathbf{x}) \quad \text{(C.1.10)}$$

Thus expressions must now be obtained for all the forces and moments about Trim.

C.1.2 Restoring Force

From Section 3.4.1 and given Trim conditions:

$$\tau_{1G}(\Delta\mathbf{x}) + \tau_{1B}(\Delta\mathbf{x}) = g(m - V\rho) \begin{bmatrix} -\Delta\theta \\ \Delta\phi \\ -\sin\Theta_T \Delta\theta \end{bmatrix} \quad \text{(C.1.11)}$$

In the case of the OCEC, the distance between the centre of gravity and centre of bouyancy is only along the x axis thus:

$$\tau_{2B}(\Delta\mathbf{x}) = gV\rho x_B \begin{bmatrix} 0 \\ -\sin\Theta_T \Delta\theta \\ \Delta\phi \end{bmatrix} \quad \text{(C.1.12)}$$

Where:

x_B is the distance along the x-axis to the centre of bouyancy.

C.1.3 Damping Force

From Section 3.4.2 and given Trim conditions:

$$\tau_{1P} = -V_w\rho \begin{bmatrix} C_x^d(V_w \sin\Theta_T \Delta\theta + \Delta u) \\ C_y^d \Delta y \\ C_z^d(-V_w \Delta\theta + \Delta w) \end{bmatrix} \quad \text{(C.1.13)}$$

Where:

C_x^d , C_y^d, C_z^d are the consolidated linear damping coefficients in the x, y, and z directions for the entire vessel.

Similarly:

$$\tau_{2P} = -V_w\rho \begin{bmatrix} C_l^d(\Delta p - \Delta r) \\ C_m^d \Delta q \\ C_n^d(\Delta r - \Delta p) \end{bmatrix} \quad \text{(C.1.14)}$$

Where:

C_l^d , C_m^d, C_n^d are the consolidated angular damping coefficients about the xx, yy, and zz axes for the entire vessel.

C.1.4 Wing Force

The lift force due to hydrofoil was found to be an order of magnitude less than the restoring, damping, and tether forces. The Trim condition is also at the cross-over point between stalled and unstalled behaviour for the wings, so the behaviour is clearly non-linear. For simplicity of this analysis, the drag component of the wing force has been incorporated into the restoring force and the lift component is disregarded.

C.1.5 Cable Force

All other forces exerted by the tether are insignificant next to elastic force, so only the elastic force will be considered for this analysis. From Section 4.7 and given Trim conditions:

$$\tau_{1C} = C_e \begin{bmatrix} x_T \cos\Theta_T \Delta x - z_T \sin\Theta_T \Delta z - z_T x_c \sin\Theta \Delta\theta \\ \Delta y \\ z_T \cos\Theta_T \Delta z - z_T x_c \cos\Theta_T \Delta\theta - x_T \sin\Theta_T \Delta x \end{bmatrix} \tag{C.1.15}$$

Where:

C_e is the elastic resistance coefficient.

Similarly

$$\tau_{2C} = -C_e \begin{bmatrix} 2 z_T \Delta\phi {y_c}^2 \\ x_c(x_T \Delta x \sin\Theta_T + z_T(\Delta z + x_c \Delta\theta)\cos\Theta_T) \\ 2 x_T(-\Delta\psi + \sin\Theta_T \Delta\phi) {y_c}^2 \end{bmatrix} \tag{C.1.16}$$

Where:

x_c and y_c are the offsets of the wing tether points from the centre of gravity in the x and y directions.

C.1.6 Canard Force

The change in drag due to the canard position is negligible so this will be discarded.

$$\tau_{2cn} = C_{cn} x_{cn} \begin{bmatrix} 0 \\ \delta_C + \Delta\theta - \Delta q \\ 0 \end{bmatrix} \tag{C.1.17}$$

Where:

C_{cn} is the coefficient of canard moment.

x_{cn} is the distance along the x axis of the pivot point of the canard from the centre of gravity.

C.1.7 Aileron Force

The change in drag due to the aileron position is negligible so this will be discarded.

$$\tau_{2al} = C_{al} y_{al} \begin{bmatrix} \delta_A + \Delta r \\ 0 \\ 0 \end{bmatrix} \tag{C.1.18}$$

Where:

C_{al} is the coefficient of aileron moment.

y_{al} is the distance along the y axis of the middle of the aileron from the centre of gravity.

C.1.8 Summary

Consolidating the above equations into the correct form for the state space equation gives:

$$\begin{aligned}\dot{u} = \frac{1}{m_x}(&-\Delta\theta(g(m - V\rho) - V_w^2 \rho {C_x}^d \sin\Theta_T - C_e z_T x_c \sin\Theta_T) - V_w \rho {C_x}^d \Delta u \\ &+ C_e x_T \Delta x \cos\Theta_T - C_e z_T \Delta z \sin\Theta_T)\end{aligned} \tag{C.1.19}$$

$$\dot{v} = \frac{1}{m_y}(g(m - V\rho)\Delta\phi - C_e \Delta y) \tag{C.1.20}$$

$$\begin{aligned}\dot{w} = \frac{1}{m_z}((&-g(m - V\rho)\sin\Theta_T + {V_w}^2 \rho {C_z}^d \sin\Theta_T - C_e z_T x_c \cos\Theta_T)\Delta\theta \\ &- V_w \rho C_z \sin\Theta_T \Delta w - C_e x_T \Delta x \sin\Theta - C_e z_T \Delta z \cos\Theta_T)\end{aligned} \tag{C.1.21}$$

$$\dot{p} = \frac{1}{I_{xa}}(-V_w \rho {C_l}^d \Delta p + V_w \rho {C_l}^d \Delta r + C_e z_T {y_c}^2 \Delta\phi + C_A y_{al}(\delta_A + \Delta r) \tag{C.1.22}$$

$$\begin{aligned}\dot{q} = \frac{1}{I_{ya}}((&-g(m - V\rho)\sin\Theta_T + C_e z_T {x_c}^2 \cos\Theta_T)\Delta\theta - V_w \rho {C_m}^d \Delta q \\ &- C_e x_c x_T \sin\Theta_T \Delta x - C_e z_T \cos\Theta_T \Delta z + C_{cn} x_{cn}(\delta_C + \Delta\theta - \Delta q))\end{aligned} \tag{C.1.23}$$

$$\dot{r} = \frac{1}{I_{za}}(-C_e \Delta y - V_w \rho {C_n}^d (\Delta r - \Delta p) + 2 C_e x_T (-\Delta\psi + \sin\Theta_T \Delta\phi) {y_c}^2) \tag{C.1.24}$$

C.2 Longitudinal Matrix Actual Values

$$\begin{bmatrix} \dot{u} \\ \dot{w} \\ \dot{q} \\ \dot{x} \\ \dot{z} \\ \dot{\theta} \end{bmatrix} = \begin{bmatrix} -200 & 0 & 11 & -11500 & -2422 & 10 \\ 0 & -0.6 & 0 & 0 & -0.11 & -0.015 \\ 0 & 0 & -0.45 & -12 & 0 & -0.4 \\ 0.97 & -0.24 & 0 & 0 & 0 & 0 \\ -0.24 & 0.97 & 0 & 0 & 0 & 0 \\ 0 & 0 & 1 & 0 & 0 & 0 \end{bmatrix} \begin{bmatrix} u \\ w \\ q \\ x \\ z \\ \theta \end{bmatrix} + \begin{bmatrix} 0 \\ 0 \\ 1.2 \\ 0 \\ 0 \\ 0.7 \end{bmatrix} \delta_C \tag{C.2.1}$$

C.3 Lateral Matrix Actual Values

$$\begin{bmatrix} \dot{p} \\ \dot{r} \\ \dot{\phi} \\ \dot{\psi} \end{bmatrix} = \begin{bmatrix} -0.32 & 0 & 0 & 0.01 \\ 0 & -1.2273 & 0.4 & -0.45 \\ 1 & 0.25 & 0 & 0 \\ 0.25 & 1 & 0 & 0 \end{bmatrix} \begin{bmatrix} u \\ w \\ q \\ x \end{bmatrix} + \begin{bmatrix} 0 \\ 0 \\ 3.2 \\ 0 \end{bmatrix} \delta_A \tag{C.3.1}$$

List of References

[1] Garrison, T.: *Oceanography: An Invitation to Marine Science 4th Edition.* Brooks/Cole Publishing, 2002.

[2] Rouault, M.: *Agulhas Current variability determined from space: a multi-sensor approach.* Ph.D. thesis, University of Cape Town, 2011.

[3] Lutjeharms, J.: Three decades of research on the greater Agulhas Current. *Ocean Science*, vol. 3, no. 1, pp. 129–147, 2007.

[4] Biastoch, A., Beal, L., Lutjeharms, J. and Casal, T.: Variability and Coherence of the Agulhas Undercurrent in a High-resolution Ocean General Circulation model. *Journal of Physical Oceanography*, vol. 39, no. 1, pp. 2417–2436, 2009.

[5] Meyer, I., Reinecke, J., Roberts, M. and Van Niekerk, J.: Assessment of ocean energy resources off the South African coast. Tech. Rep., University of Stellenbosch, 2013.

[6] Elghali, S., Benbouzid, M. and Charpentier, J.: Marine tidal current electric power generation technology: State of the art and current status. *2007 IEEE International Electric Machines Drives Conference*, vol. 2, pp. 1407–1412, 2007.

[7] Marine Current Turbines: Accessed 6/01/11.
Available at: `www.marineturbines.com`

[8] Khan, M., Iqbal, M. and Quaicoe, J.: River current energy conversion systems: Progress, prospects and challenges. *Renewable and Sustainable Energy Reviews*, vol. 12, no. 8, pp. 2177–2193, 2008.

[9] Souczek, E.: Stream turbine. US Patent 2501696, 1946.

[10] Bowley, W.: Underwater power generator. US Patent 4383182, 1979.

[11] Fossen, T.: *Guidance and Control of Ocean Vehicles.* John Wiley and Sons, 1994.

[12] Hansen, M.: *Aerodynamics of Wind Turbines 2nd Edition.* Earthscan, 2008.

[13] Bahaj, A., Molland, A. and Chaplin, J.: Power and thrust measurements of marine current turbines under various hydrodynamic flow conditions in a cavitation tunnel and a towing tank. *Renewable Energy*, vol. 32, pp. 407–426, 2007.

[14] Hoerner, S. and Borst, H.: *Fluid-Dynamic Lift.* Liselotte A Hoerner, 1975.

[15] Buckham, B., Nahon, M., Zhao, X. and Lambert, C.: Dynamics and control of a towed underwater vehicle system, part i: model development. *Ocean Engineering*, vol. 30, pp. 453–470, 2003.
Available at: `http://www.elsevier.com/locate/oceaneng`

[16] Oldfield, S.: Method of counteracting the tendency of a tethered electricity water current-driven turbine to dive when power is produced. RSA Patent pending, 2010.

[17] Bryden, H., Beal, L. and Duncan, L.: Structure and Transport of the Agulhas Current and its Temporal Variability. *Journal of Oceanography*, vol. 61, no. 1980, pp. 479–492, 2005.

[18] Tsugawa, M. and Hasumi, H.: Generation and growth mechanism of the Natal Pulse. *Journal of Physical Oceanography*, vol. 40, pp. 1597–1612, 2010.

[19] Dept of Minerals and Energy: Digest of South African energy statistics. 2009.

[20] Cross, C.: Electricity generation options consideredby ESKOM, ESKOM. 2012.

[21] Dept of Minerals and Energy: White paper on renewable energy. 2003.

[22] Dept of Energy: Bid window 3 preferred bidders' announcement. 2013.

[23] Wilson, A.: Machines, power and the ancient economy. *The Journal of Roman Studies*, vol. 92, pp. 1–32, 2002.
Available at: `http://www.jstor.org.ez.sun.ac.za/stable/3184857?seq=18`

[24] Charlier, R. and Menanteau, L.: The saga of tide mills. *Renewable and Sustainable Energy Reviews*, vol. 1, no. 3, pp. 171–207, 1997.

[25] Free Flow Energy: History of wave and current devices. 2009.
Available at: `www.freeflowenergy.com`

[26] New Energy Corporation Ltd: Accessed 6/01/11.
Available at: `www.newenergycorp.ca`

[27] The Engineering Business Ltd: Accessed 6/01/11.
Available at: `www.engb.com`

[28] Dehlsen, J. and Dehlsen, G.: Method of controlling operating depth of an electricity generating device having a tethered water driven turbine. US Patent 6091161, 1998.

[29] Ecomerit Technologies LLC: Accessed 7/01/11.
Available at: `ecomerittech.com/aquantis.php`

[30] Robson, J.: Submersible electrical power generating plant. US Patent 6531788, 2001.

[31] Robson, J.: Submersible electrical power generating plant. US Patent 7291936, 2006.

[32] Gulf Stream Turbines LLC: Accessed 7/01/11.
Available at: `www.currentpower.se`

[33] Manchester, R.: Submerged power generating apparatus. US Patent 7441988, 2004.

[34] SMD Hydrovision: Accessed 7/01/11.
Available at: `www.smd.co.uk`

[35] Imlay, FH: The complete expressions for "added mass" of a rigid body in an ideal fluid. 1961.

[36] Vanzwieten, J., Driscoll, F., Leonessa, A. and Deane, G.: Design of a prototype ocean current turbine - part i: mathematical modeling and dynamics simulation. *Ocean Engineering*, vol. 33, no. 11-12, pp. 1485–1521, 2006.

[37] Palmer, D., Van Niekerk, J., Van Backström, T., Crosby, C. and Thiart, G.: Sea Renewable Energy: Submerged turbine feasibility study. Tech. Rep., University of Stellenbosch, 2010.

[38] Google Maps: Accessed 25/121/13.
Available at: `maps.google.co.za`

[39] Stellenbosch Weather: Accessed 25/121/13.
Available at: `weather.sun.ac.za`